Doctoral Dissertation

Magnetic characteristics of Wiegand wire elucidated by its induced pulse voltage and magnetization measurements

誘導パルス電圧と磁化過程の測定による Wiegand ワイヤの磁気特性の解明

Department of Mathematics, Physics, Electrical Engineering and Computer Science,
Graduate School of Engineering Science,
Yokohama National University

Chao Yang　　楊 超

Dissertation advisor: Professor Yasushi Takemura

January, 2022

Abstract

Internet of Things (IoT) is an important part of the new-generation information technology. It provides technical guarantees for improvements in the quality of human life and development of society. However, the power supply required for the monitoring, connecting, and interactive devices in the IoT, for providing real-time collection and control, has become a factor restricting its development.

In this study, a Wiegand sensor (often used for energy harvesting) is proposed as a battery-less sensor or self-powered device, with an objective to mitigate the power supply problem in the monitoring, connecting, and interactive devices. When the Wiegand sensor is used as a power source, it can not only effectively charge devices equipped with batteries, thereby prolonging their battery life, but also provide power to devices without internal batteries, thereby solving problems concerning difficult power supplies and wiring. Thus, the devices used for monitoring, connection, and interaction in the IoT can achieve maintenance-free and long-term operation. Accordingly, Wiegand sensors are expected to be widely used for IoT technologies.

As the magnetic structure of a Wiegand wire cannot be elucidated using a traditional hysteresis curve, in this study, a first-order reversal curve (FORC) was used to analyze the magnetic characteristics of the Wiegand wire. The magnetization reversal of the soft and hard regions in the wire was identified in the FORC diagrams. The two-layer magnetic structure (without marked boundaries) was clarified. In addition, the magnetization reversal of the intermediate layer was discussed. The relationship between the magnetization process of the Wiegand wires and their magnetic structure was obtained. The electrical power of the pulse signal from the Wiegand sensor was maximized as the power supply for the electronic modules so that the energy of the Wiegand sensor pulse signal could meet power consumption requirements. This research, through magnetic-flux guidance experiments on the Wiegand wire, determined that the magnetic flux density through the center of the Wiegand wire, position of the pickup coil, and angle between the Wiegand sensor and magnetic induction line were the main factors affecting the energy of a Wiegand pulse. The relationships between these factors and the energy of the Wiegand pulse were also obtained. Moreover, in this process, an appropriate configuration of the Wiegand wire was identified for when the Wiegand sensor was used as a power source, i.e., in addition to the necessary pickup coil, ferrite beads should be set at both ends of the Wiegand wire. In addition to the external conditions, the energy of the Wiegand pulse was found to be closely related to its own magnetization characteristics.

To further analyze the magnetic characteristics of the Wiegand wire under different excitation magnetic fields, this study considered three typical magnetic fields, i.e., those produced by a rotating magnet with radial magnetization, by a pair of rotating bar magnets with axial magnetization, and by a solenoid coil with AC current. The amplitude, area, and timing of the induced pulse voltage from a pickup coil placed along the Wiegand wire were analyzed. It was found that the energy of the Wiegand pulse depends on the degree of magnetization reversal of the soft layer in the Wiegand wire. Both the initialization and maximum degree of magnetization reversal in the soft layer are detected at the position with the strongest magnetic field. The direction of magnetization reversal propagation is along the direction in which the intensity of the externally applied magnetic field decreases. The velocity of the domain wall movement is faster when the ferrite beads are added to both ends of the Wiegand wire.

Therefore, the magnetic characteristics of a Wiegand wire can be elucidated according to its induced pulse voltage and magnetization measurements, and Wiegand sensors can be designed according to different applications. In particular, when the Wiegand sensors are used as a battery-less sensor or self-powered device, the maximum energy of a single Wiegand pulse can be obtained according to these magnetic characteristics, so as to meet the power consumption requirements of the IoT devices. This is a major research achievement in the field of electronics.

Table of Contents

Chapter 1: Introduction

1.1 Background

The Internet of Things (IoT) refers to the real-time collection and control of any object or process that needs to be monitored, connected and interacted with through various devices and technologies, including information sensors, radio frequency identification (RFID) technology, global positioning system (GPS), infrared sensors, and laser scanners. [1] Subsequently, the collected information, such as information regarding sound, light, heat, electricity, mechanics, chemistry, biology, and location, is connected to various possible networks to realize the ubiquitous connections between things, and between things and people. The purpose is to provide intelligent perception, identification, and management of objects and processes. The IoT is an information carrier based on the Internet and traditional telecommunications networks. It allows all ordinary physical objects to be independently addressed, thereby forming an interconnected network.

The IoT has been hailed as the next step of the information technology revolution. The development of the IoT technology has set off a wave of digitization and intelligent transformations in various industries worldwide. [2] Digitization is the foundation, and intelligence is the goal. The application field of the IoT involves various aspects. The application of the IoT in the field of infrastructure, such as for industry, agriculture, environment, transportation, logistics, and security, has effectively promoted intelligent development in these areas, e.g., making a more reasonable use and allocation of limited resources, thereby improving the efficiency and benefit of the industry. [3] Applications in the household, medical and health, education, finance, and service industries, along with tourism and other fields closely related to life, have greatly improved in terms of the service scope, service methods, and service quality, greatly improving people's quality of life. A typical application case of the IoT is shown in Figure 1.1.

The application of IoT technology to road traffic is relatively mature. With the increasing popularity of social vehicles, traffic congestion (or even paralysis) has become a major problem in cities. Providing real-time monitoring of road traffic conditions and timely transmission of information to drivers, so that drivers can make timely travel adjustments, can effectively relieve the traffic pressure. An automatic road charging system (electronic toll collection) can be set up at highway intersections, saving the time required for getting and returning a card at the entrance and exit, and improving the traffic efficiency of the vehicles. A positioning system installed on the bus can timely understand

the bus route and arrival time, and passengers can decide to travel according to the route, so as to avoid unnecessary wastes of time. With the increase in social vehicles, in addition to bringing increased traffic pressure, parking is also becoming a more prominent problem. Many cities have launched smart roadside parking management systems. Typically, a smart roadside parking management system is based on a cloud computing platform and combines IoT technology and mobile payment technology, so as to share parking resources and improve the parking utilization rate and user convenience. The system is compatible with mobile phone and radio frequency identification modes. Through mobile APP software, the user can timely understand parking information and locations, make reservations in advance and pay fees, etc.; this largely solves the problem of "difficult parking."

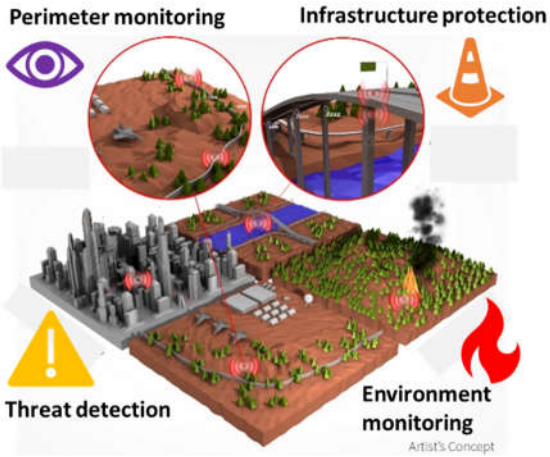

Figure 1.1 Typical application case of the Internet of Things. [4]

A "smart home" represents a basic application of the IoT in the home. [5] With the popularity of broadband services, smart home products are involved in all aspects of the home. Even with no one at home, users can use mobile phones and other products for remote client operation, e.g., intelligent air conditioning for adjusting the room temperature. Such systems can even can learn the user's habits so as to achieve automatic temperature control operation (for example, users can go home in the hot summer to enjoy the comfort of a cool home). Through the client, users can activate intelligent bulbs, control the brightness and color of bulbs, etc. Socket built-in Wi-Fi systems allow for remote control socket timing by turning the current on or off. They can monitor the power consumption of equipment, generate an electricity chart to clarify power consumption, and arrange the use of resources and budgets. A smart scale can be employed for monitoring exercise results. For example, built-in advanced sensors can monitor

conditions such as blood pressure and fat content, and a built-in program can make health recommendations according to the state of the body. A smart toothbrush can be connected to the client to provide reminders regarding the brushing time and brushing position. Moreover, it can produce charts and oral health status notifications according to the data from the brushing. In addition, smart cameras, window sensors, smart doorbells, smoke detectors, smart alarms and other security monitoring equipment are indispensable for families. Even if away from home, users can check the real-time situation of any corner of the home at any time and place, and identify any security risks. Thus, seemingly complicated household life can become more relaxed and beautiful because of the IoT.

In recent years, global climate anomalies have occurred frequently, and the suddenness and harm of the corresponding disasters have further increased. The Internet can monitor environmental insecurities in real time, so as give early warnings in real time and allow for timely measures to reduce the threat of disasters to human life and property and/or prevent them in advance. IoT technology can intelligently perceive index data regarding the atmosphere, along with soil, forest, and water resources and other aspects, and can therefore play a massive role in improving the human living environment.

The development of the IoT in recent years has gradually increased in scale, as all countries have invested massive amounts of manpower, material resources, and financial resources for research and development. However, owing to the wide and irregular distribution of monitoring nodes in the IoT, the cost for deploying monitoring nodes can greatly increase, and even remote monitoring nodes cannot be wired. Therefore, researchers have widely used wireless monitoring nodes to replace wired detection nodes. [6,7] A wireless monitoring node is suitable for applications and for the transmission of video data comprising large-scale, long-distance fixed points and mobile points, and can better overcome the problems in wired transmission, reduce the initial investment cost, and reduce the workload for subsequent maintenance. Although wireless monitoring nodes are designed with low power consumption, owing to their limited battery life, the battery still needs to be replaced regularly. Self-powered sensors can effectively solve this problem. [8-11]

This so-called self-generation is also called "energy harvesting." [12, 13] Sensors collect the tiny energy around the body and use it as electricity, which has become an indispensable part of the Internet. [14] At present, the most commonly used self-powered sensors include Hall sensors, magnetoresistive sensors, electromagnetic sensors, and Wiegand sensors using the Barkhausen effect. [15-17] The output characteristics of the various sensors are shown in Figure 1.2. Among them, the Wiegand sensor consists of two parts: one is the Wiegand wire, which is the sensitive element in the sensor, and the

other is the pickup coil, wound around on the Wiegand wire. When a magnetic field with a certain intensity or higher is applied to the Wiegand wire in the Wiegand sensor, a rapid magnetization reversal called the "large Barkhausen jump" occurs. This magnetization reversal induces a pulse voltage in the pickup coil wound around the Wiegand wire.

Sensors	Detection principle	Power	Output waveform High frequency Low frequency
Hall sensor	Hall effect	With Power supply	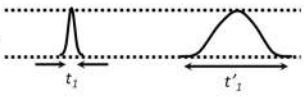
MR sensor	Magnetoresistance effect	With Power supply	
Electromagnetic sensor	Electromagnetic induction	Without Power supply	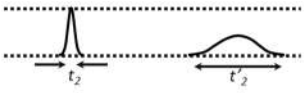
Wiegand sensor	Large Barkhausen jump	Without Power supply	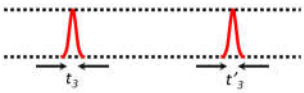

Figure 1.2 Output characteristics of different self-generated sensors. [18]

When an alternating magnetic field is applied to Wiegand wires, positive and negative pulse voltages are repeatedly generated. Thus, Wiegand sensors, consisting of a Wiegand wire and pick-up coil, can be used as self-powered sensors and as power sources for external devices and sensors [18]. Additionally, the Wiegand sensor has a wide operating temperature range, does not require an external power supply, and, owing to the fast magnetization of the soft layer, the amplitude of its induced pulse voltage does not depend on the frequency of the applied alternating magnetic field[19,20]. These properties make the Wiegand sensors advantageous over other conventional sensors and power generators. Owing to these specific features, the applications of the Wiegand sensor are no longer limited to generating output signals as a magnetic sensor; instead, it is possible to use a Wiegand sensor as an electrical power source for various equipment [21]. When used as power sources, Wiegand sensors can efficiently charge battery-equipped devices, thereby improving the battery life. Moreover, Wiegand sensors can provide power to devices without internal batteries; this solves certain difficulties in the power supply and wiring. Therefore, as a battery-less sensor or self-powered device, the Wiegand sensor is expected to be widely used in the field of IoT.

1.2 Research Objective and Main Contribution

The objective of this work is to maximize the electrical power of the pulse signal from the Wiegand sensor, so that the energy of the pulse signal from the Wiegand sensor can meet the power supply requirements of wireless nodes. This will eliminate the need for battery operation and maximize the application potential of the Wiegand sensor, especially its potential as a power supply to electronics modules. To achieve this objective, it is essential to clarify the magnetic structure of the Wiegand wire, understand the magnetization process of the Wiegand wire under different excitation magnetic fields, and increase the pulse voltage generated by the Wiegand wire without changing the external magnetic field conditions. The advantage of using the Wiegand pulse for energy harvesting is that the electrical power can be generated by the movement or vibration of a magnet with an extremely slow speed, i.e., almost zero [18]; this may not be possible with other vibration-type energy harvesters.

In the past, for convenience, the magnetic structure of the Wiegand wire has been described as a two-layer structure, with the vicinity of the surface (with low coercivity) as a soft layer, and the interior (with high coercivity) as a hard core. However, this limits the understanding of the magnetization phenomenon occurring inside the Wiegand wire, and the details of the magnetization processes of the two layers in the wire have not been fully clarified. Therefore, it is necessary to clarify the two-layer structure of the Wiegand wire, and the relationship between the magnetization processes of Wiegand wires and their magnetic structures. For this reason, the magnetization process was analyzed by using the first-order reversal curve (FORC) method, and a two-layer magnetic structure without evident boundaries was verified. In addition, the magnetization reversal of the intermediate layer of the Wiegand wire was also examined.

This study attempted to set ferrite beads at both ends of the Wiegand wire, changed the position of the pickup coil around the Wiegand wire, and adjusted the direction of the Wiegand sensor in the magnetic field. The magnetic flux through the center of the Wiegand wire increased after the ferrite beads were set at both ends of the Wiegand wire. The simulation results predicted an increase in the magnetic flux density, and it was estimated that the energy of the Wiegand pulse would increase in a corresponding manner. When the pickup coil was closer to the center of the Wiegand wire, the angle between the Wiegand sensor and magnetic induction line was smaller, and the energy of the Wiegand pulse was larger. Thus, the factors with great influences on the energy of the Wiegand

pulse were successfully determined. An appropriate configuration was chosen, so as to maximize the energy of the Wiegand pulse without changing the external field conditions.

When applying this configuration of Wiegand sensors to battery-less sensors or power-generating sensors, an appropriate excitation method must also be applied. To identify the optimal excitation methods for different applications, it is essential to examine the magnetization characteristics of the Wiegand wire in different excitation magnetic fields. Accordingly, for each of multiple cases, the magnetic field distribution in the wire was simulated for predicting the trend of magnetization. Specifically, the initial position, propagation direction and velocity, and degree of magnetization reversal in the Wiegand wire were described. These characteristics were analyzed according to the amplitude, area, and timing of the pulses as generated in the pickup coils under different applied magnetic fields. Meanwhile, placing ferrite beads at both ends of the wire was found to increase not only the degree but also the propagation velocity of the magnetization reversal in the soft layer of the Wiegand wire.

In sum, in this research, the magnetic characteristics of the Wiegand wire were elucidated based on induced pulse voltage and magnetization measurements, so that an optimal self-powered sensor for different applications of the IoT could be designed based on the magnetic characteristics.

1.3 Organization of the Dissertation

In this research, aiming to expand the application potential of Wiegand sensors (especially as power supplies for electronic modules), the magnetic characteristics of the Wiegand wire, i.e., the sensitive element of the Wiegand sensors, were elucidated according to induced pulse voltage and magnetization measurements.

In Chapter 1, the background, purposes, and main contributions of this research are introduced. The research background of Section 1.1 describes the convenience brought by the development and application of IoT technologies to human life, and the contributions the IoT has made to social development. At the same time, it also indicates a factor limiting the further development and application of the IoT technology, i.e., the power supply problem, as the power supplies for monitoring, connection, and interactive devices needs to be collected and controlled in real time in the IoT. Then, several commonly used self-powered sensors are listed, and their output characteristics are compared. Finally, based on the comparison results, it is concluded that the Wiegand sensor, used in this research as a battery-less sensor or self-powered device, can solve the power supply problem for the monitoring, connection, and interactive devices in the IoT, and is expected to be widely used in the field of the IoT. In the purpose and main contribution portions of Section 1.2, the purpose of this research is given, i.e., to maximize the electrical power of the pulse signal from the Wiegand sensor, so that the energy of the pulse signal from the Wiegand sensor can meet the power supply requirements for the devices that need to be monitored, connected, and interact in the IoT. Then, the contributions of this research aiming to achieve this purpose are described.

In Chapter 2, the reasons why materials have magnetism are discussed, along with the magnetization, anisotropy, and magnetostriction of magnetic materials, causes of magnetic domains inside magnetic materials, and propagation of magnetic domain walls. For the magnetic material (the Wiegand wire) used in this research, its simple magnetic structure, the relationship between the Barkhausen jump and its internal magnetization reversal, and the essential reason for the pulse generated in the pickup coil are introduced. Then, the three methods used in this research to elucidate the magnetic characteristics of magnetic materials are examined: a traditional hysteresis loop method, the FORC method, and a method for examining the amplitude, area, and timing of the pulse voltage generated in the pickup coil.

In Chapter 3, as the magnetic structure of the Wiegand wire cannot be elucidated using a traditional hysteresis curve, the FORC is used to analyze the magnetic characteristics

of the Wiegand wire. The magnetization reversal of the soft and hard regions in the wire is identified in the FORC diagrams. The magnetization reversal in the dominantly irreversible process of the soft layer and the magnetic intermediate region between the soft and hard regions is clarified. The relationship between the magnetization process of the Wiegand wires and their magnetic structure is obtained. The two-layer magnetic structure, without marked boundaries, is determined. In addition, the magnetization reversal of the intermediate layer is discussed.

As discussed in Chapter 4, the distributions of the magnetic field generated from an applied magnet in air and in the Wiegand wire are simulated before conducting experiments. The simulations predict an increase in the magnetic flux density through the center of the Wiegand wire. This work finds that the magnetic flux density through the center of the Wiegand wire, position of the pickup coil, and angle between the Wiegand sensor and magnetic induction line are the main factors affecting the energy of a Wiegand pulse. The relationship between these factors and the energy of the Wiegand pulse is identified. Moreover, it is concluded that setting the ferrite bead at both ends of the Wiegand wire is advantageous for practical applications of the Wiegand sensor regarding power supply.

In Chapter 5, aiming to understand magnetization characteristics of the Wiegand wire under different applied magnetic fields for excitation, this work considers three typical magnetic fields: one produced by a rotating magnet with radial magnetization, another produced by a pair of rotating bar magnets with axial magnetization, and a third produced by a solenoid coil with an AC current. Then, the amplitude, area, and timing of the induced pulse voltage from the pickup coil placed along the Wiegand wire are analyzed. The magnetization reversal in the wire is initiated at the location with the maximum applied field intensity. The direction of the magnetization reversal propagation is along the direction in which the intensity of the externally applied magnetic field decreases. The velocity of domain wall movement is faster when ferrite beads are added to both ends of the magnetic wire.

Finally, Chapter 6 summarizes this research. The organization of this dissertation is shown in Figure 1.3.

Figure 1.3 Organization of the present dissertation.

Chapter 2: Theories

2.1 Magnetic Materials

2.1.1 Magnetism and Magnetization

All substances are magnetic, and the magnetism of a substance originates from the movement of electrons in atoms. In atoms, electrons have orbital magnetic moments owing to their motion around the nucleus, and spin magnetic moments owing to their spin. The magnetic moments of atoms are mainly derived from the orbital magnetic moments and spin magnetic moments of the electrons. Therefore, magnetic moments are often used to describe magnetism. The magnetization, M, is defined as the effective contribution of all atomic magnetic moments or dipoles as averaged over a given volume, or as the net magnetic moment per unit volume. The magnetism of a substance is a collective reflection of the magnetism of all of the elementary particles comprising the substance. Different substances exhibit different magnetism behaviors in an external applied magnetic field. According to the magnetism of the substance in an external applied magnetic field, the magnetism can be classified as diamagnetism, paramagnetism, ferromagnetism, antiferromagnetism, and ferrimagnetism. [22, 23] That is, any substance can be magnetized in an external applied magnetic field, but the degree of magnetization may be different.

The diamagnetism of a substance means that the magnetic moments of the electrons in the atoms of the substance cancel each other out, and the resultant magnetic moment is zero. Thus, there is no effective magnetic moment. However, when the substance is excited by an external applied magnetic field, the orbital motions of the electrons will change, and a small total magnetic moment will be generated in the opposite direction of the external applied magnetic field. In this way, the magnetic susceptibility of the material becomes a very small negative number (quantity). Therefore, the substance behaves as diamagnetic. In addition, all organic compounds are diamagnetic substances.

The classical theory for explaining the paramagnetism of a substance is Langevin's theory. The theory states that there is no interaction between the atomic magnetic moments (m). Moreover, they are free magnetic moments and point in any direction randomly owing to thermal fluctuations, as shown in Figure 2.1. Therefore, when no external magnetic field is applied, the magnetization, $M = \Sigma m = 0$. However, when an external magnetic field is applied, the angles of some atomic magnetic moments change. These will rotate and align in the direction of the applied field, resulting in low magnetization and positive susceptibility. As the intensity of the external applied field

increases, a greater number of atomic moments align along the external field, increasing linearly. However, when the external applied magnetic field is removed, the atomic magnetic moment returns to a random state.

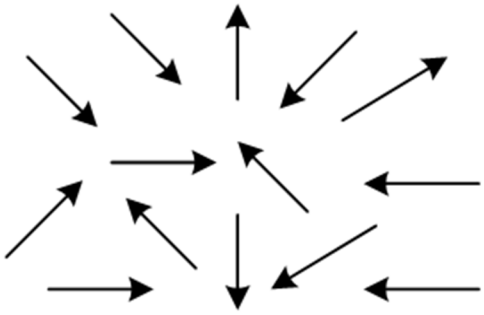

Figure 2.1 Illustration of magnetic moment in paramagnetic substance.

The exchange interaction model believes that there are exchange interactions between the atoms in magnetic materials, and that this exchange interaction only occurs between neighboring atoms. It is this internal exchange interaction that allows the atomic magnetic moment to overcome the disordered effect of the thermal motion, leading to the same-direction alignment of neighboring magnetic moments, as shown in Figure 2.2. Thus, the substance shows ferromagnetism. The origin of this ferromagnetism is the parallel arrangement of the magnetic moments of the atoms in the substance, which leads to spontaneous magnetization.

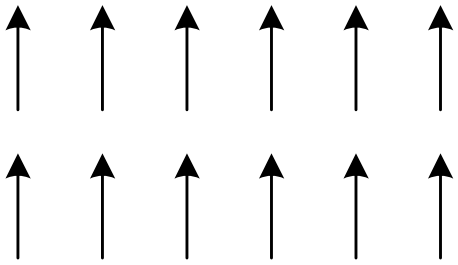

Figure 2.2 Illustration of magnetic moment in ferromagnetic substance.

Specifically, the exchange energy between two adjacent atoms, i and j, is defined as follows:

$$E_{ex} = -2\,J_{ex}\,S_i \cdot S_j \tag{2.1}$$

In Equation (2.1), J_{ex} is the exchange integral, and S_i and S_j are the spins of the exchange-interacting atoms, respectively. The conditions of the ferromagnetism can be obtained

from the exchange interaction model. First, the substance must have an atomic magnetic moment; second, the exchange integral must be greater than 0, that is, $J_{ex} > 0$.

For antiferromagnetic substances, there is a strong negative interaction between the atoms making up these substances. Therefore, adjacent magnetic moments tend to align in antiparallel. In addition, the moments can be distributed with the same values in two interpenetrating but antiparallel lattices of the crystal, as shown in Figure 2.3. Thus, when they are perfectly aligned, they can cancel each other out, and there is no magnetization.

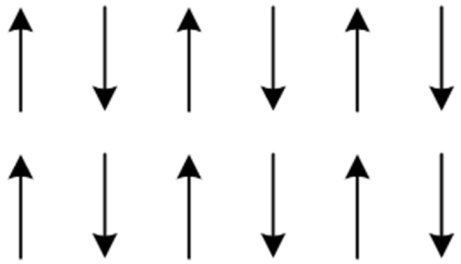

Figure 2.3 Illustration of magnetic moment in antiferromagnetic substance.

Many antiferromagnetic substances exhibit paramagnetism by disordering their spins above a critical temperature T_N (Néel temperature), but exhibit antiferromagnetism when the temperature is lower. As Néel temperatures are usually much lower than room temperature, to determine whether a material that is paramagnetic at room temperature is antiferromagnetic at low temperature, it is necessary to measure its susceptibility at a very low temperature.

The behavior of ferrimagnetic substances is similar to that of ferromagnetic materials. The adjacent magnetic moments tend to be arranged in antiparallel, but they are distributed in the different values in the two interpenetrating but antiparallel lattices of the crystal, as shown in Figure 2.4. As such, they cannot cancel each other out, and the ferrimagnetic substances exhibit a spontaneous magnetization. However, when the temperature rises above the Curie temperature, the spontaneous magnetization of the substance disappears and turns into paramagnetism. This ferrimagnetic behavior is usually observed in oxides. There are two or more magnetic substances on different sublattices, with different magnetic moments.

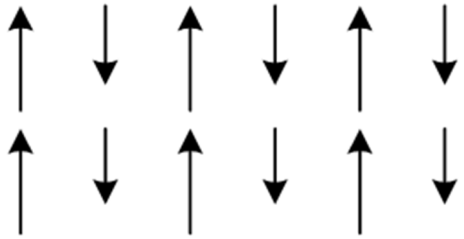

Figure 2.4 Illustration of magnetic moment in antiferromagnetic substance.

Although all substances are magnetic, not all substances can be used as magnetic materials. A magnetic material is a substance that responds significantly to an externally applied magnetic field. Generally speaking, in this study, "magnetic materials" denotes strongly magnetic substances.

Magnetic materials can be classified into soft magnetic materials and hard magnetic materials, according to the degree of difficulty of their magnetization. Soft magnetic materials are magnetic materials with low coercivity and high magnetic permeability, that is, the maximum magnetization can be achieved with the smallest intensity of the external applied magnetic field. Hard magnetic materials refer to magnetic materials with high coercivity. Such materials can retain high remanence for a long time after being magnetized by an external applied magnetic field, and even after the external magnetic field is removed. Therefore, they are also called permanent magnetic materials.

2.1.2 Magnetic Anisotropy and Magnetostriction

When a magnetic material is magnetized in different directions in the applied magnetic field, it exhibits different characteristics along different directions (axes). This phenomenon, i.e., that the magnetic characteristics vary of the magnetic material depending on the direction of the magnetization, is called "magnetic anisotropy." [23] In addition, in many cases, it is easy to magnetize in some directions, but not easy to magnetize in other directions. The easy magnetization direction is called the easy direction of magnetization, or the easy axis of magnetization. The direction that is not easy to magnetize is called the hard direction of magnetization, or the hard axis of magnetization.

The magnitudes of the magnetization energy required for magnetization along the hard and easy magnetization axes of a magnetic material are different. The magnetization energy required for the easy axis of magnetization is the smallest. On the contrary, the magnetization energy required for the hard axis of magnetization is the largest. This energy, related to the axis of magnetization, is called the magnetic anisotropy energy. Furthermore, according to the physical mechanism of the origin of the magnetic anisotropy, it can be divided into magneto-crystalline anisotropy, shape magnetic anisotropy, stress magnetic anisotropy, induced magnetic anisotropy, and exchange magnetic anisotropy.

When a magnetic material is magnetized by an external applied magnetic field, its length and volume change. This phenomenon is called magnetostriction. The change in size along the direction of the external applied magnetic field is called longitudinal magnetostriction, and the change in size perpendicular to the direction of the applied external magnetic field is called transverse magnetostriction. This change in length is also called linear magnetostriction. Correspondingly, the change in the volume of a magnetic material is called volume magnetostriction. The magnetostriction of the volume is very small, and can usually be ignored. Therefore, the magnetostriction coefficient (λ) used to express the magnitude of the magnetostriction effect can be defined as follows:

$$\lambda = \frac{\Delta l}{l} \tag{2.2}$$

In Equation (2.2), l is the original length of the magnetic material in the direction of the magnetization, and Δl is the variable length of the magnetic material in the direction of the magnetization under the action of an externally applied magnetic field.

The magnitude of the magnetostriction is related to the intensity of the externally applied magnetic field, and generally increases with the increase of the externally applied

magnetic field strength before finally reaching saturation. At this time, the magnetostriction coefficient is at a certain value, called the saturation coefficient (λ_S) of the magnetic material.

The saturation magnetostriction coefficient λ_S of different materials are different. Some materials have λ_S values greater than 0, whereas others have λ_S value less than 0. A material with $\lambda_S > 0$ has a positive magnetostriction, that is, the length change is elongated along the direction of the external applied magnetic field, whereas the length change is shortened in the direction perpendicular to the external applied magnetic field. Conversely, for a material with $\lambda_S < 0$, it is a negative magnetostriction, that is, the length change is shortened along the direction of the external applied magnetic field, and elongated in the direction perpendicular to the external applied magnetic field. In addition, if a rotating external field is applied to ferromagnetic and ferrimagnetic rod-shaped or filamentary materials, the sample will be distorted.

For the magnetic material of the Wiegand wire used in this study, the shape anisotropy dominates, owing to its shape as a longitudinal wire. It has uniaxial anisotropy. The axial direction is the easy direction (axis) of magnetization, and the radial direction is the hard direction (axis) of magnetization, as described in detail in Section 3.2.1. In addition, the Wiegand wire has a positive magnetostriction value. Therefore, in the process of the Wiegand wire, the applied stress causes an axial uniaxial anisotropy and plastic deformation of the sample. This results in a "soft layer" with a soft magnetic appearance and a low coercivity of approximately $\mu_0 H = 2$ mT. This also results in a hard center, known as the "hard core," with a larger coercive force of approximately $\mu_0 H = 2$ to 8 mT [18-20]. The details of Wiegand wire are described in Section 2.2. In this research, μ_0 denotes the magnetic permeability in a vacuum.

2.1.3 Magnetic Domain and Movement of Magnetic Domain Wall

According to the theory in Section 2.1.1, when no external applied magnetic field is applied, there is an exchange interaction between the electronic spins of the different atoms in a ferromagnetic substance. When the temperature is lower than the Curie temperature, the magnetic moments of neighboring atoms align in the same direction, resulting in spontaneous magnetization. In addition, some ferromagnetic substances can spontaneously magnetize to a saturated state, but do not exhibit magnetism as a whole. This is because the interior of a ferromagnetic substance is divided into many small areas. The atomic magnetic moments are arranged in parallel to each other in these small areas, resulting in spontaneous magnetization. However, the magnetization directions between different regions are different, so that the magnetizations between such regions cancel each other out. Therefore, the ferromagnetic substance does not exhibit magnetism as a whole without the action of an external applied magnetic field. These small areas of spontaneous magnetization inside ferromagnetic substances are called magnetic domains. The sizes, shapes, and distributions of the magnetic domains are determined by the minimum total free energy of the system. That is, the generation of magnetic domains within ferromagnetic substances is the result of an equilibrium distribution of spontaneous magnetization, and satisfies the principle of minimum energy.

Without the action of an external magnetic field and external stress, the state of the magnetic domain is determined by the minimum value of the total free energy, which comprises the magnetostatic energy, exchange interaction energy, and magnetocrystalline anisotropy energy. A magnetic exchange interaction can cause the spin magnetic moments of neighboring atoms to align in the same direction, resulting in spontaneous magnetization. A magnetocrystalline anisotropy causes the crystal to be magnetized in the direction of the easy axis of magnetization, so that the sum of these two energies can be minimized. That is, the exchange interaction energy and magnetocrystalline anisotropy in a ferromagnetic substance will not cause the generation of magnetic domains.

The magnetic charge generated during the magnetization process increases the magnetostatic energy in a ferromagnetic substance. To reduce the magnetostatic energy generated during the magnetization process and achieve the minimum total free energy in the ferromagnetic substance, only the distribution state of the spontaneous magnetization can be changed. As a result, multiple spontaneous magnetization regions appear in the ferromagnetic substance, thereby forming magnetic domains, as illustrated in Figure 2.5. In the final analysis, the magnetic domains reduce the magnetostatic energy generated by the spontaneous magnetization.

Magnetic charges, unlike in electrostatics, always appear in pairs and balanced by opposite charges, rather than as isolated single charges. Therefore, a free magnetic pole appears; then, a demagnetizing field is generated. The size of the demagnetization field depends on the demagnetization factor and the intensity of the external applied magnetic field. When an external magnetic field is applied to a ferromagnetic substance, in addition to the exchange interaction energy, magnetocrystalline anisotropy energy, and magnetostatic energy, there should also be external magnetic field energy and magnetoelastic energy in the ferromagnetic substance.

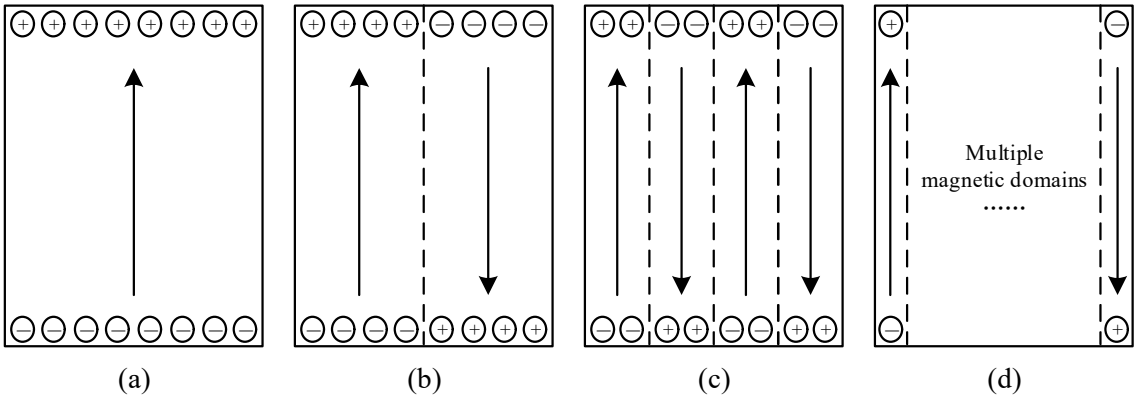

Figure 2.5 Example of magnetic domain formation in a uniaxial crystal.

In Figure 2.5(a), the entire crystal is uniformly magnetized. The magnetostatic energy or demagnetizing field has the largest intensity, the total free energy in the ferromagnetic body increases, and the above-mentioned spontaneous magnetization state is no longer stable. As a result, multiple magnetic domains with opposite magnetization directions appear in the ferromagnetic body, as shown in Figures 2.5(b), 2.5(c), and 2.5(d), and the magnetostatic energy or demagnetizing field is reduced. The greater the number of magnetic domains with opposite magnetization directions appearing, the lower the magnetostatic energy or the strength of the demagnetizing field. If there are n magnetic domains with opposite magnetization directions, then the magnetostatic energy or demagnetizing field strength at this time will reduced to 1/n of the magnetostatic energy or demagnetizing field strength during a uniform magnetization.

In the process of forming multiple magnetic domains with opposite magnetization directions, the adjacent magnetic moments change from a parallel arrangement to an antiparallel arrangement, thereby increasing the exchange interaction energy. To reduce the increase in the exchange interaction energy, the atomic magnetic moments between adjacent magnetic domains do not suddenly turn, but instead pass through a transition

region where the direction of the magnetic moment gradually changes. This transition region is called a magnetic domain wall, as illustrated in Figure 2.6.

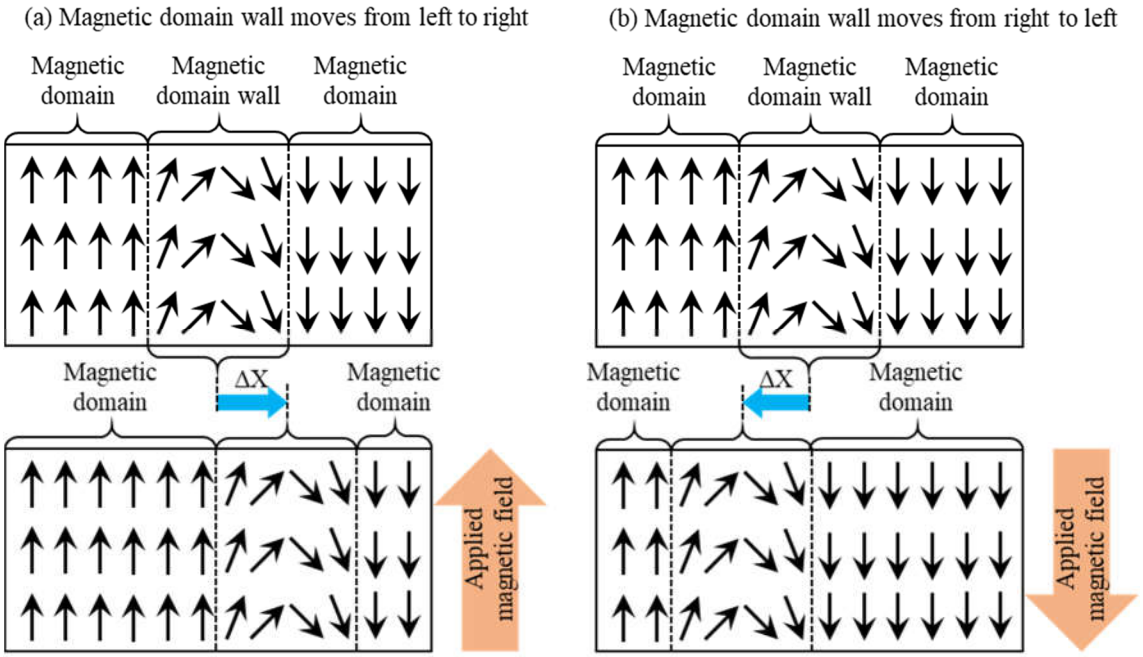

Figure 2.6 Illustration of magnetic domain wall and its movement.

As shown in the Figure 2.6, when the external magnetic field is applied, the magnetic domains whose magnetic moment directions are consistent with the direction of the external applied magnetic field become larger, and those magnetic domains whose magnetic moment directions are opposite to the direction of the external applied magnetic field become smaller. The position of the magnetic domain wall will also change accordingly. This phenomenon is considered as the movement or propagation of the magnetic domain wall. [24] The ΔX in Figure 2.6 is the distance traveled or propagated by the magnetic domain wall. In this study, pickup coils can be installed at different positions of the Wiegand wire, and the propagation or moving speed of the magnetic domain wall can be obtained by measuring the time differences in the pulse signals received by the pickup coils at different positions. The detailed information will be described in Section 2.3.3.

As the intensity of the external applied magnetic field continues to increase, the magnetic domains whose magnetic moment directions are consistent with the direction of the external applied magnetic field will continue to increase. When the intensity of the external applied magnetic field reaches a certain value, the direction of the magnetic moment of the entire magnetic domain turns to the direction of the external applied

magnetic field. The result is that the magnetization direction of the magnetic domain is parallel to the direction of the external applied magnetic field, and the magnetic material has the maximum magnetism at this time. Even when the intensity of the external applied magnetic field increases again, the magnetization of the material will not increase, and the material will reach a state of saturation magnetization.

2.2 Wiegand Wire

2.2.1 Magnetic Structure of Wiegand Wire

A Wiegand wire is a bistable magnetic material with a rapid magnetization reversal. This rapid magnetization reversal is essentially a large Barkhausen jump. The Wiegand wire was invented by Wiegand in 1974 [25]; correspondingly, the rapid magnetization reversal in the Wiegand wire is called the Wiegand effect. The Barkhausen jump and Wiegand effect are described in detail in Section 2.2.2. Initially, wires of NiFe alloys and magnetically bistable amorphous FeSiB were tested as the magnetic wires, because they showed a large Barkhausen jump. However, a vicalloy with a typical composition of $Fe_{0.4}Co_{0.5}V_{0.1}$ has been known as the optimum material for yielding this jump [26-29]. The diameter of a Wiegand wire is typically 0.25 mm. Wiegand wires of different lengths were used in this research, and were supplied from Sichuan Wisdom and Firefighting Equipment (SWFE) Co. Ltd., Meishan, China.

A torsion stress, annealing, and a cold treatment were applied to the wire during fabrication. The torsion stress was first applied to the wire and then released [30]. When a torsional stress is applied along the radial direction of a Wiegand wire, a strong uniaxial anisotropy is imparted along the length of the wire, and after the torsion stress is eliminated, a residual stress occurs in the wire. This causes different magnetic properties near the surface regions of the wire and around the center. In particular, the coercive force on the outer layers of such wires is reduced under the large stress occurring during the twisting process [31, 32], whereas that of the core remains unchanged. The surface region is a soft magnetic material with a low coercivity of approximately $\mu_0 H = 2$ mT. The volume ratio of this "soft layer" is calculated as 23% at a maximum and the thickness of the soft layer is approximately 0.03 mm, as previously reported in detail [18, 33]. The center is known as the "hard core," with a larger coercive force of approximately $\mu_0 H = 8$ mT.

Finally, the cold-treatment process improves the strength, twisting, and anti-twisting abilities of the Wiegand wire. The magnetic properties of twisted FeCoV wires depend on the conditions of the torsion stressing and annealing, as previously reported [34]. For convenience, Wiegand wires exhibit magnetic structures that can be described as comprising two layers: a magnetically soft outer layer and a hard core, with lower and higher coercive forces, respectively. However, in fact, the coercivity of the two layers does not change drastically; rather, it changes gradually along the radial direction. Moreover, there is no evident boundary between the two layers, as verified in this study. The two-layer magnetic structure of the Wiegand wire is shown in Figure 2.7.

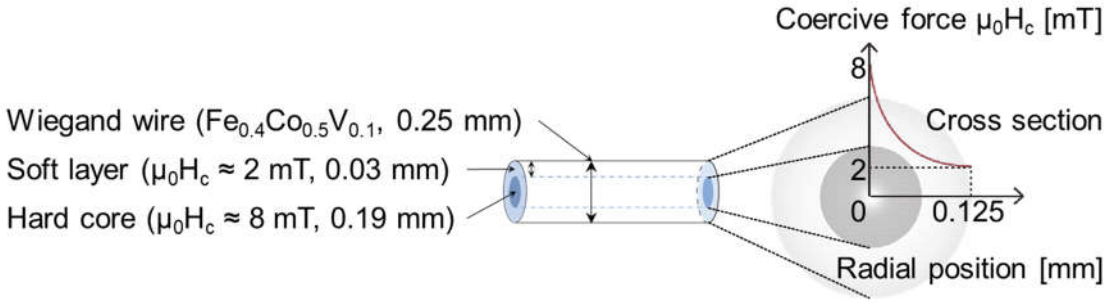

Figure 2.7 Two-layer magnetic structure of the Wiegand wire.

The Wiegand wire is the sensitive element of the Wiegand sensor. The Wiegand sensor is based on the Barkhausen effect [18] and consists of two parts: one is the Wiegand wire, and the other is the pickup coil wound around the Wiegand wire. Because the Wiegand sensor does not require an external power supply, it can output sharp and perfect voltage pulses by changing only the polarity of the applied external magnetic field. Moreover, the width of the pulse does not depend on the ratio of the change of the applied external magnetic field [25, 35-36]. This unique and remarkable feature makes Wiegand sensors widely popular in applications than other magnetic sensors, such as in electromagnetic sensors that use the electromagnetic effect, Hall sensors that use the Hall effect, and magnetic resistance sensors that use the magnetoresistance effect. A typical configuration of the Wiegand sensor is illustrated in Figure 2.8.

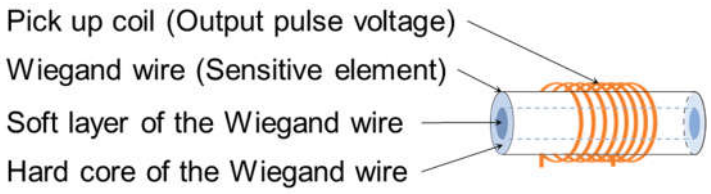

Figure 2.8 Typical configuration of the Wiegand sensor.

2.2.2 Barkhausen Jump and Wiegand Effect

A ferromagnetic material is composed of a series of independent magnetic domains. Within the magnetic domains, all of the atomic magnetic moments are arranged in the same direction, so each magnetic domain is a magnet with a high-intensity magnetic field. The spontaneous magnetization directions of the magnetic domains are different and their magnetisms cancel each other out, so the entire ferromagnetic material does not show magnetism to the outside. Nevertheless, when the ferromagnetic material is subjected to an external magnetic field with high intensity, the magnetic domain walls propagate, causing all of the independent magnetic domains to align in the same direction. Accordingly, the ferromagnetic material has magnetism. This is also the magnetization process of the ferromagnetic material from the demagnetization state to the saturation state.

However, in the magnetization processes of ferromagnetic materials, the magnetization degree does not increase smoothly, but increases with small jumps, an indicated in Figure 2.9. When a jump occurs, noise accompanies it. This jump is called a Barkhausen jump, and the noise generated during the jump is called Barkhausen noise. [37-39] If the noise is amplified by a loudspeaker, a series of "clicks" will be heard. This phenomenon is the "Barkhausen effect." In particular, in the process of arranging independent magnetic domains in the same direction, the movements of the magnetic domain walls are not stable and two adjacent magnetic domains can rub against each other and vibrate, thereby generating noise.

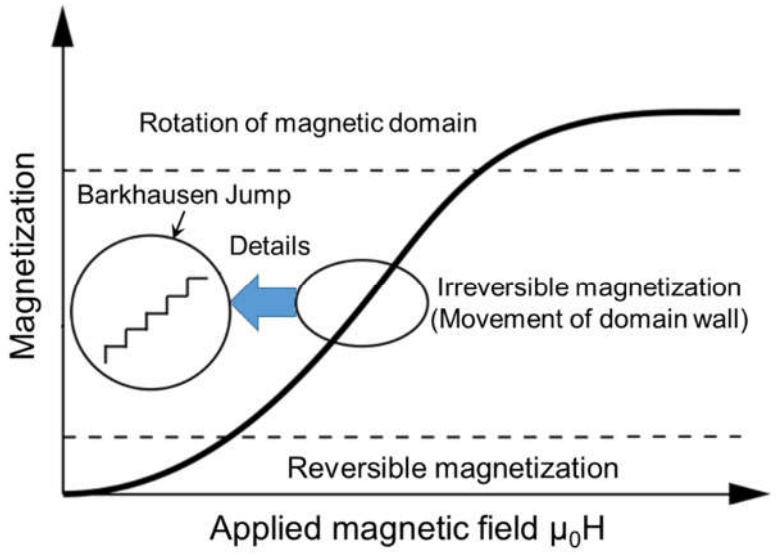

Figure 2.9 Magnetization process and Barkhausen jump.

For the Wiegand wire used in this research, Barkhausen jumps are also generated in the process of its magnetization. This rapid and steep magnetization reversal can be observed in its magnetization curve, as shown in Figure 3.3. Interestingly, this rapid magnetization reversal is not observed under an external magnetic field greater than the coercive field of the hard core, or less than the coercive field of the soft layer. That is to say, the magnetic field reversal only occurs in the external magnetic field between the coercive field of the soft layer and the coercive field of the hard core. Therefore, this magnetization reversal is considered to be the magnetization reversal of the soft layer of the Wiegand wire. An illustration of the magnetization reversal of the soft layer in the Wiegand wire is shown in Figure. 2.10.

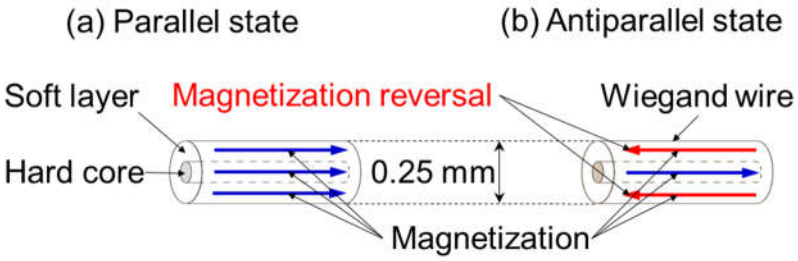

Figure 2.10 Explanation of the magnetization reversal of the soft layer in the Wiegand wire: (a) parallel state; (b) antiparallel state.

When no external magnetic field is applied, the hard and soft layers are parallel [40], as shown in Figure 2.10(a). When opposite magnetic fields with appropriate strengths are applied to the wire, the soft layer with the low coercivity will flip first [41–43], as demonstrated in Figure 2.10(b). As the magnetization reversal of the soft layer in the Wiegand wire is rapid and steep, the magnetization jump in the Wiegand wire is usually called the large Barkhausen jump, and is also known as the Wiegand effect [20, 44–45]. The process of the magnetization reversal for the entire Wiegand wire will be described in further detail in Section 3.2.3.

2.2.3 Electromagnetic Induction and Wiegand Pulse

Electromagnetic induction is one of the most important discoveries in electromagnetics. It shows the interconnections and transformations between electricity and magnetism. [23] The in-depth study of the essence of electromagnetic induction was of great significance to the establishment of Maxwell's electromagnetic field theory. Electromagnetic induction has a wide range of applications in electrical engineering, electronic technologies, and electromagnetic measurement.

Electromagnetic induction refers to a coil placed in a changing magnetic flux, which generates electromotive forces at both ends of the coil. There are two approaches to making the magnetic flux change. In one, the coil does not move and the magnetic field changes with time; in the other, the magnetic field does not change and the coil moves within the magnetic field, so that the magnetic flux passing through the coil changes. If the coil is closed, there will be a current flowing through the coil. If the coil is not closed, there will be a voltage at both ends of the coil, but no current will flow through the coil. The voltage and current generated according to this phenomenon are called the induced electromotive force and induced current, respectively. For the generation of the induced electromotive force, it is only necessary to satisfy the condition that the magnetic flux passing through the coil changes. For the generation of the induced current, not only the magnetic flux passing through the coil changes, but also, the coil (placed in the magnetic field) is closed. When a current passes through the conducting wire, a magnetic field is generated around it.

Assuming that the number of turns of the closed coil is N, the induced electromotive force can be expressed as follows:

$$\varepsilon = -N\frac{d\phi}{dt} = -\frac{d\Phi}{dt} \tag{2.3}$$

$$\Phi = N\phi \tag{2.4}$$

In the equations, ε, N, ϕ, and Φ are the induced electromotive force (V), number of coil turns, magnetic flux (Wb), and interlinkage magnetic flux (Wb), respectively.

The magnetic flux is calculated as follows:

$$\phi = B \cdot S \cdot cos\theta \tag{2.5}$$

In the above, B, S, and θ are the magnetic induction intensity of the magnetic field (T), area enclosed by the coil in the magnetic field (m^2), and angle between the direction of the magnetic field and area enclosed by the coil (°), respectively.

As noted in the description in Section 2.2.2, a large Barkhausen jump can be observed during the magnetization process of the Wiegand wire, and this is considered to be the

magnetization reversal of the soft layer of the Wiegand wire. This also means that the magnetic flux inside the Wiegand wire has changed at this time. In this way, the pickup coil around the Wigand wire can induce a voltage pulse, which is called the Wiegand pulse. The pickup coil is 5-mm long and has 3,000 turns. The amplitude of the voltage pulse can exceed several volts and the pulse width is approximately 10 μs, as shown in Figure 2.11.

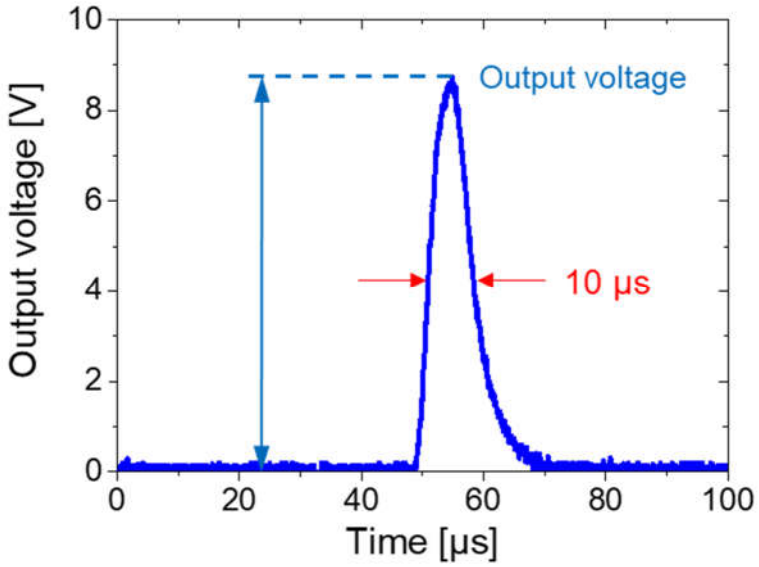

Figure 2.11 Waveform of the Wiegand pulse.

Therefore, in this research, the law of electromagnetic induction is also used to convert the magnetization reversal of the Wiegand wire into electrical energy. The detection method for the electromagnetic induction in the magnetization reversal process of the soft layer in the Wiegand Wire is shown in Figure 2.12.

During the magnetization reversal of the soft layer in the Wiegand wire, the magnetic flux will leak to the outside of the Wiegand wire, as shown in Figure 2.12(b). At this time, if a pickup coil is set at the position where the magnetization of the soft layer in the Wiegand wire is reversed (as shown in Figure 2.12(a)), according to the electromagnetic induction theory, the pickup coil will output an induced pulse voltage. The amplitude and area of the pulse detected by the pickup coil are proportional to the volume of the reversed soft layer in the magnetic wire, which in turn depends on the intensity of the external magnetic field used for excitation [41, 46]. In addition, the width of the pulse does not depend on the ratio of the change of the applied external magnetic field [26, 35].

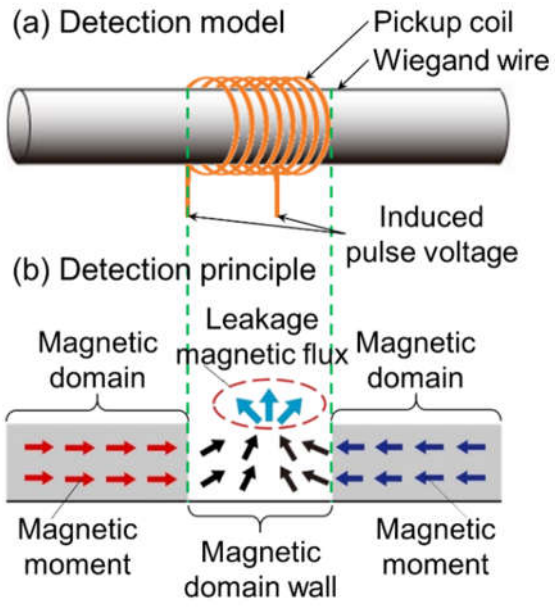

Figure 2.12 Detection method of electromagnetic induction in the Wiegand wire: (a) detection model; (b) detection principle.

Moreover, according to the phenomenon of magnetic flux leakage caused by the magnetization reversal of the soft layer in the Wiegand wire, by setting the pickup coils at different positions of the Wiegand wire, the propagation of the magnetic domain wall can be observed. The specific content will be introduced in Section 2.3.3.

2.3 Elucidation Methods of Magnetic Characteristics

2.3.1 Magnetic Hysteresis Loops

A magnetic hysteresis loop shows the relationship between a magnetization M and magnetic field H in the process of the repeated magnetization of a magnetic material [47-48]. This loop can be measured experimentally. However, it is only an important feature for ferromagnetic and ferromagnetic materials; paramagnetic and diamagnetic materials do not have this phenomenon.

The magnetization of ferromagnetic materials (including ferromagnetic and ferrimagnetic materials) starts from the residual magnetization M = 0, and gradually increases the intensity of the applied external magnetic field H. The magnetization will increase until it reaches magnetic saturation state. If magnetization field H increases again, the magnetization state of the sample will remain basically unchanged. The curve drawn according to the relationship between magnetization and H in this process is called the initial magnetization curve.

If the intensity of the applied external magnetic field is reduced at this time, the magnetization curve does not return along the original initial magnetization curve; this indicates that the change in magnetization lags behind the change in the applied external magnetic field. This phenomenon is called the magnetism stagnant. When the intensity of the applied external magnetic field is reduced to zero, the magnetization is not zero, but rather, is equal to the residual magnetization M_r. To reduce the magnetization to zero, a reverse external magnetic field must be applied, and when the intensity of the reverse external magnetic field is $-H_c$, the magnetization is zero, and H_c is called the coercive force of the magnetic material. If the intensity of the reverse magnetic field continues to increase until the sample is magnetized in the opposite direction to the saturation state, the corresponding magnetization saturation value is $-M_s$.

After that, if the reverse magnetization field is reduced to zero, then it will increase in the positive direction. The magnetization state of the sample will return to the positive saturation magnetization state along another curve, as shown in Figure 2.13. The curve from forward saturation to reverse saturation and that from reverse saturation to forward saturation are symmetrical with respect to the origin. It can be seen from this that when the magnetization field of a magnetic material changes periodically, the relationship between the degree of magnetization of the magnetic material and intensity of the applied magnetic field is a closed curve. This closed curve is called the magnetic hysteresis loop.

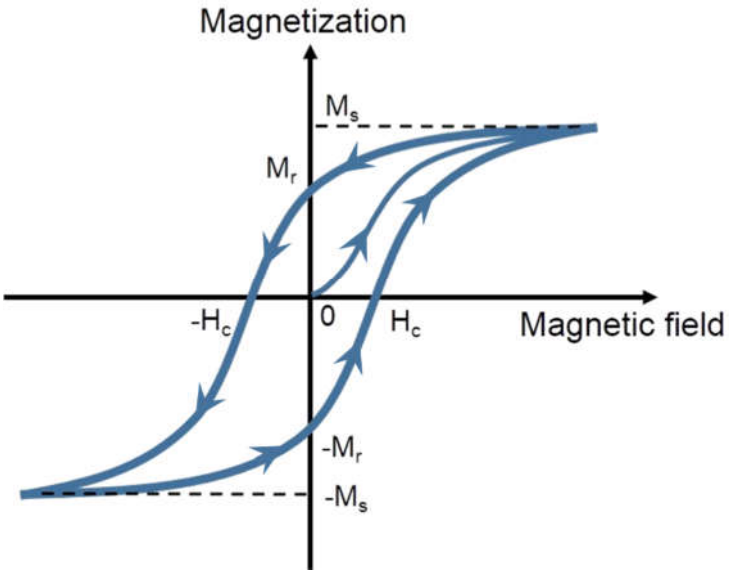

Figure 2.13 Example of the major loop of the magnetic material.

If the sample is repeatedly magnetized and the maximum value of the applied magnetization field intensity is less than the corresponding magnetic field intensity when the sample is in the saturation magnetization state, some small magnetic hysteresis loops will be obtained. These small magnetic hysteresis loops are called minor loops, as shown in Figure 2.14. The largest one of all magnetic hysteresis loops, that is, the above-mentioned curve from the forward saturation state to the reverse saturation state and then back to the forward saturation state, is often called the major loop, as shown in Figure 2.13.

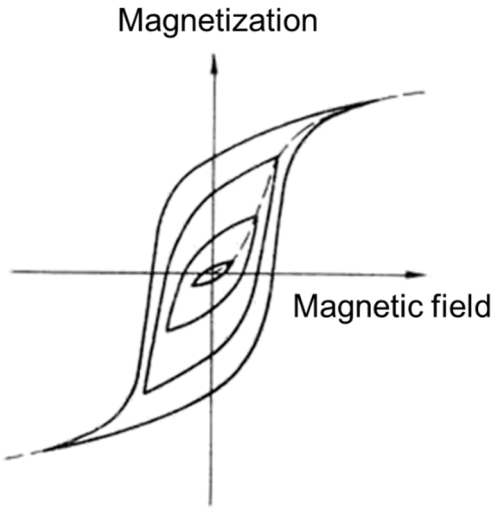

Figure 2.14 Example of the minor loops of the magnetic material.

The line connecting the vertices at both ends of each hysteresis loop is called the normal magnetization curve, as shown by the dashed line in Figure 2.14. It basically coincides with the initial magnetization curve. Owing to the hysteresis phenomenon of the magnetic material, the magnetic material will generate heat when it is repeatedly magnetized in the forward and reverse directions in the applied external magnetic field, that is, the energy of the applied magnetic field will become heat, and then be lost in the magnetic material. The size of the energy loss of the magnetic material from the repeated magnetization process is proportional to the size of the area enclosed by the magnetic hysteresis loop.

The magnetic hysteresis loop reflects the magnetization characteristics of the magnetic material. There are several very effective magnetic static parameters of the magnetic material on the magnetic hysteresis loop, such as the residual magnetization M_r, coercive force H_c and the saturation magnetization M_s. These parameters reflect the magnetic characteristics of the magnetic material, and also determine the shape of the magnetic hysteresis loop for the magnetic material. Different magnetic materials have different shapes of magnetic hysteresis loops. For example, the hysteresis loop of a soft magnetic material is long and thin, making it easy to magnetize and demagnetize, whereas the hysteresis loop width of a hard-magnetic material is short, making it difficult to magnetize and demagnetize. In addition, different shapes of magnetic hysteresis loops have different applications. As such, the magnetic hysteresis loop provides a basis for the selection of materials for practical applications.

2.3.2 First-Order Reversal Curves (FORCs)

The magnetization data and applied magnetic field form a class of partial hysteresis curves known as FORCs [49, 50]. A FORC analysis is an advanced hysteresis measurement method, and is increasingly being used in research on magnetic materials. This is because it can provide additional information for characterizing magnetic properties, i.e., information which cannot be obtained using normal hysteresis curves [51-54]. The FORC information includes the distribution of the coercivity and interaction fields and the identification of multiple phases in composite or hybrid materials containing more than one phase [51, 52]. Moreover, the FORCs also provide insight into the relative proportions of the reversible and irreversible components of the magnetization of a magnetic material.

The FORCs are measured by first saturating the magnetic material in a large positive field ($\mu_0 H_{sat}$). Then, the field is decreased to a reversal magnetic field ($\mu_0 H_a$). The FORC is defined as the magnetization curve measured by increasing the reversal magnetic field ($\mu_0 H_a$) back to $\mu_0 H_{sat}$, as illustrated in Figure 2.15(a). Finally, the process is repeated for several values of $\mu_0 H_a$ to yield a series of FORCs [55, 56], as shown in Figure 2.15(b). The magnetization corresponding to any applied magnetic field ($\mu_0 H_b$) of a FORC can be expressed as M ($\mu_0 H_a$, $\mu_0 H_b$), where $\mu_0 H_b \geq \mu_0 H_a$. The parameters $\mu_0 H_a$, $\mu_0 H_b$, and M ($\mu_0 H_a$, $\mu_0 H_b$) of the FORCs are described in Figure 2.15(a).

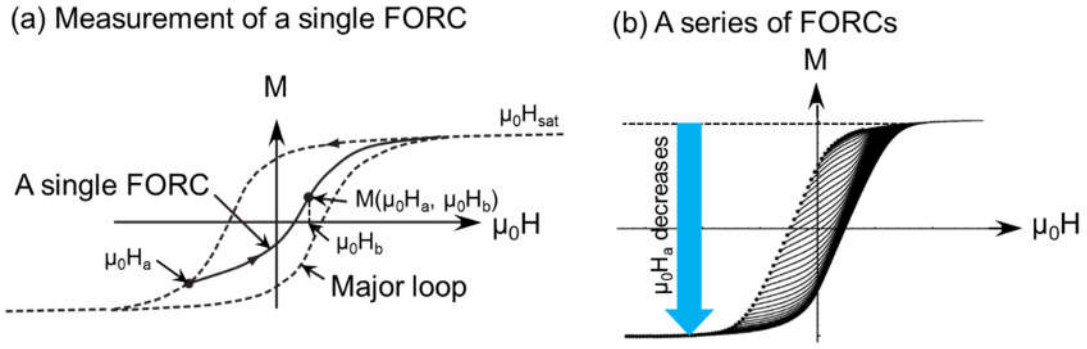

Figure 2.15 Illustration of the first-order reversal curve (FORC) measurements: (a) measurement of a single FORC; (b) a series of FORCs.

The FORC distribution is defined as a mixed second derivative, as follows:

$$\rho(\mu_0 H_a, \mu_0 H_b) = -\frac{\partial^2 M(\mu_0 H_a, \mu_0 H_b)}{\partial \mu_0 H_a \, \partial \mu_0 H_b} \tag{2.6}$$

The calculated FORC distributions are contour plots. To analyze the distribution of the switching and interactions of the magnetic material, it is common to change the

coordinates from $\{\mu_0 H_a, \mu_0 H_b\}$ to $\{\mu_0 H_c, \mu_0 H_u\}$ ($\mu_0 H_c = (\mu_0 H_b - \mu_0 H_a) / 2$, $\mu_0 H_u = (\mu_0 H_b + \mu_0 H_a) / 2$). [57, 58] In that context, $\mu_0 H_c$ corresponds to the distribution of the switching field or coercive field, and $\mu_0 H_u$ corresponds to the distribution of the interaction field or reversal field. [59-61]

As a FORC distribution is defined as the mixed second derivative shown in Equation (2.6), taking the second derivative magnifies the noise inevitably present in the magnetization data [57, 58]. As with the standard method of fitting a function to experimental data, a segmented method is used to reduce the influence of noise on the FORC distribution. In other words, instead of fitting a function to the entire $M(\mu_0 H_a, \mu_0 H_b)$ surface and then directly differentiating the surface to determine $\rho(\mu_0 H_a, \mu_0 H_b)$, the FORC distribution at each point is determined by fitting a mixed second-order polynomial to a local, moving grid. The expression of the second-order polynomial is as follows:

$$a_1 + a_2 H_a + a_3 H_a^2 + a_4 H_b + a_5 H_b^2 + a_6 H_a H_b \quad (2.7)$$

In this case, the fitting parameter $-a_6$ provides the mixed second derivative of the fit surface, and can be assigned to the center of the grid as a representation of the FORC distribution density at that point [57]. As the polynomial is only second-order, it cannot accurately accommodate complex surfaces. However, for the Wiegand wire used in this research, this usually does not become a problem, because it usually has a relatively smooth FORC distribution. The size of the local grid is determined based on a user-defined smoothing factor (SF), where the size of the grid is only $(2SF+1)^2$. Therefore, it is necessary to introduce a SF into the calculation of the FORC distribution. If the SF is too small, the FORC diagram will contain a large amount of noise, and increasing the SF can effectively reduce this noise. However, when the SF is excessively large, it not only reduces the contribution of noise, but also removes the measured data [57]. Furthermore, a suitable SF is very important in the FORC diagram, and usually, simple tests can be conducted to determine the suitable SFs for each sample. These tests determine when all of the noise is removed by smoothing, and if SF is greater than this value, only the measured data is removed [55, 57]. The SF usually takes a value between 2 and 5, but ideally, it should be 2. A local grid is used to calculate the FORC distribution of the point at the center of the local grid, as shown in Figure 2.16.

Owing to the non-regular FORC diagram in this work, a simple SF is no longer applicable; as such, a series of SFs are used. They are SFs in a horizontal direction to be used along the vertical ridge (Sc0), in a horizontal direction to be used just outside the vertical ridge region (Sc1), in the vertical direction to be used along the central ridge (Sb0), and in the vertical direction to be used just outside the central ridge (Sb1). These parameters are usually used for identifying the presence of ridges in a non-regular FORC

diagram. For a full explanation of these parameters, see Reference 63. In this study, according to the above guidelines for obtaining the optimal SF, tests were performed, and then the values of the SFs were determined. In particular, Sc0, Sc1, Sb0, and Sb1 were set to 6, 8, 6, and 8, respectively, and the rate of increase in the SF was set to a typical value of 0.1.

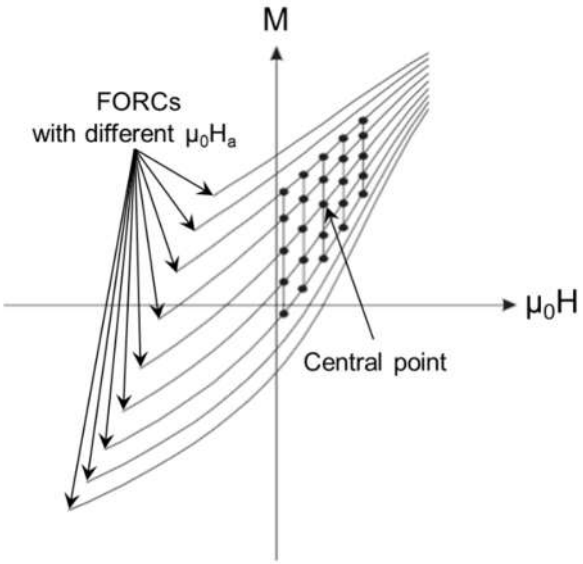

Figure 2.16 Local grid used to calculate the FORC distribution of the point at the center of the local grid (SF = 2).

There are several open-source software programs available for calculating FORC distributions and plotting FORC diagrams, such as FORCinel [62] and VARIFORC [63]. The advanced functions of VARIFORC can be selected from the FORCinel menu. Therefore, FORCinel and its auxiliary software (Igor Pro®, WaveMetrics Inc., Portland, OR, USA) were used in this research.

2.3.3 Induced Pulse from Wiegand Wire

The fast magnetization reversal in Wiegand wires induces a pulse voltage in the pick-up coil wound around the wire [64, 65]. This is because when the magnetization of the soft layer in the Wiegand wire is reversed, the magnetic flux leaks from the position where the magnetization is reversed to the outside of the Wiegand wire; thus, the pickup coil wound around the Wiegand wire generates a pulse voltage.

According to Equation (2.3), the obtained induced electromotive force voltage is proportional to the rate of change of the magnetic field. However, for the Wiegand wire, even if the rate of change of the applied magnetic field is as low as almost zero, the Wiegand sensor will generate a pulse voltage with a constant intensity. This shows that the amplitude of the pulse voltage induced from the Wiegand wire has nothing to do with the rate of change of the applied magnetic field. That is, the change of the magnetic flux density in the Wiegand wire has nothing to do with the rate of change of the applied magnetic field. The change of the magnetic flux density in the Wiegand wire is related to the degree of magnetization of the soft layer of the Wiegand wire. The greater the degree of magnetization of the soft layer of the Wiegand wire, the greater the change of the magnetic flux density in the Wiegand wire, and the greater the amplitude of the induced pulse voltage. The degree of magnetization of the soft layer in the Wiegand wire depends on the intensity of the applied external magnetic field. The greater the intensity of the applied external magnetic field, the greater the degree of magnetization of the soft layer of the Wiegand wire. Thus, the amplitude of the induced pulse voltage generated by the Wiegand wire is proportional to the intensity of the applied external magnetic field. Therefore, by analyzing the amplitude and area of the induced pulse voltage generated by the Wiegand wire, the magnetic characteristics concerning the degree of magnetization reversal of the soft layer in the Wiegand wire under different intensities of applied external magnetic fields can be obtained.

In addition, a Wiegand wire shows domain wall propagation when the intensity of the applied external magnetic field reaches a certain threshold, regardless of the time rate of change of the applied external magnetic field. By setting up pick-up coils at different positions of the Wiegand wire, the propagation of the magnetic domain wall can be observed. The experimental principle of the propagation of the magnetic domain wall is shown in Figure 2.17. When an exciting coil or magnet is used to apply a reverse magnetic field to the entire Wiegand wire, a reverse magnetic domain (as the core of the domain wall propagation) is formed at a certain position of the Wiegand wire, and the magnetic domain wall begins to propagate from this position. When the magnetic domain wall

propagates to different positions, the coils at different positions will induce pulse voltages, respectively, and there is a certain time difference between the induced pulse voltages. In this way, the propagation velocity of the magnetic domain wall can be calculated based on the time difference between the pulse voltages and distance between the coils. By selecting pickup coils at different positions, the propagation velocity of the domain wall at different positions of the entire Wiegand wire can be respectively measured.

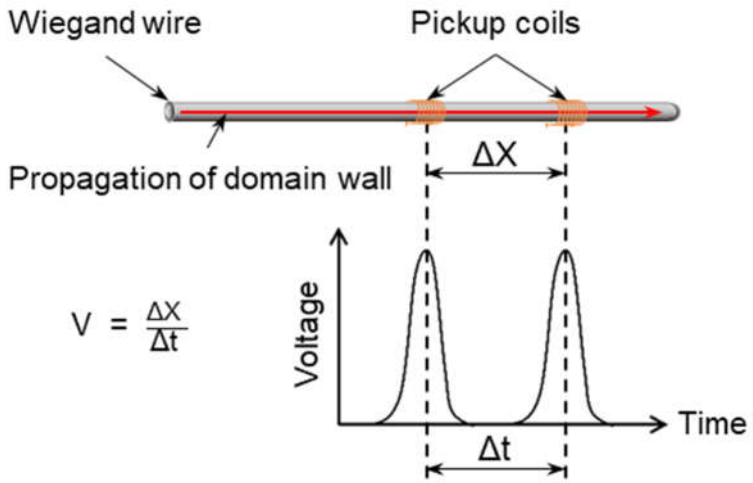

Figure 2.17 Method of measuring propagation velocity of magnetic domain wall.

At the same time, the position of the first coil that induces the pulse voltage is the initial position of the reverse magnetic domain formation, i.e., the initial position of the magnetization reversal of the soft layer in the Wiegand wire. Usually, the initial position of the reverse magnetic domain formation is the position where the intensity of the opposite magnetic field is strongest on the Wiegand wire; thus, the magnetization reversal of the soft layer in the Wiegand wire occurs at the position where the intensity of the opposite magnetic field is the strongest on the Wiegand line. Moreover, according to the sequence of the pulse voltage as induced by the different coils, the propagation direction of the magnetic domain can be obtained, that is, the direction of magnetization reversal of the soft layer in the Wiegand wire can be obtained. In this way, the magnetic characteristics of the initial position of the magnetization reversal of the soft layer in the Wiegand wire are obtained, along with its direction and the velocity of its propagation.

Chapter 3: Magnetization Analysis of Wiegand Wire

This chapter is one of the three chapters describing the research results acting as the main contributions of this dissertation. It presents the research results regarding the magnetization process, magnetization reversal, and magnetic structure of the Wiegand wire. The magnetization process for the whole Wiegand wire was identified using traditional magnetic hysteresis curves. In particular, by using the FORC method, the magnetization reversals of the soft and hard regions in the wire were identified, the magnetization reversals of the dominantly irreversible process of the soft layer and magnetic intermediate region between the soft and hard regions were clarified, and a two-layer magnetic structure of the Wiegand wire without marked boundaries was verified. These research results cannot be elucidated using conventional magnetization hysteresis curves.

3.1 Magnetization States of Wiegand Wire

A Wiegand wire of with a length of 5 mm was used in this work. Generally, owing to the magnetic structure of the Weigand wire, the two layers usually exhibit different magnetization states (parallel or antiparallel to each other), as depicted in Figure 3.1. Initially, the hard core and soft layer are in parallel in Figure 3.1(a) [42]. When a magnetic field with the appropriate strength and opposite polarity from the wire's initial magnetization is applied, the soft layer with low coercivity will first flip, as shown in in Figure 3.1(b) [21, 40]. When the reverse magnetic field continues to increase, the hard core (with higher coercivity) will also reverse its magnetization so that the two layers are parallel with each other again, as shown in Figure 3.1(c). When the polarity of the external magnetic field changes, the soft layer becomes reversed first as shown in Figure 3.1(d), before the hard core flips to be parallel to the soft layer once more, and the wire returns to the initial magnetization state in a cyclic process [43].

The Wiegand wire is in the parallel state in Figure 3.1(a) and Figure 3.1(b), and in the antiparallel state in Figure 3.1(c) and Figure 3.1(d). The difference between the two parallel states lies in the direction of magnetization. Normally, these states occur when the wire is completely magnetized, when the applied external magnetic field $\mu_0 H_{ext}$ is greater than 15 mT, and when the Wiegand wire almost simultaneously reaches the saturation state. To reach either antiparallel state, a magnetization reversal occurs in the

soft layer, inducing a pulse of several volts and with a duration of 10 μs in the pickup coil placed around the Wiegand wire.

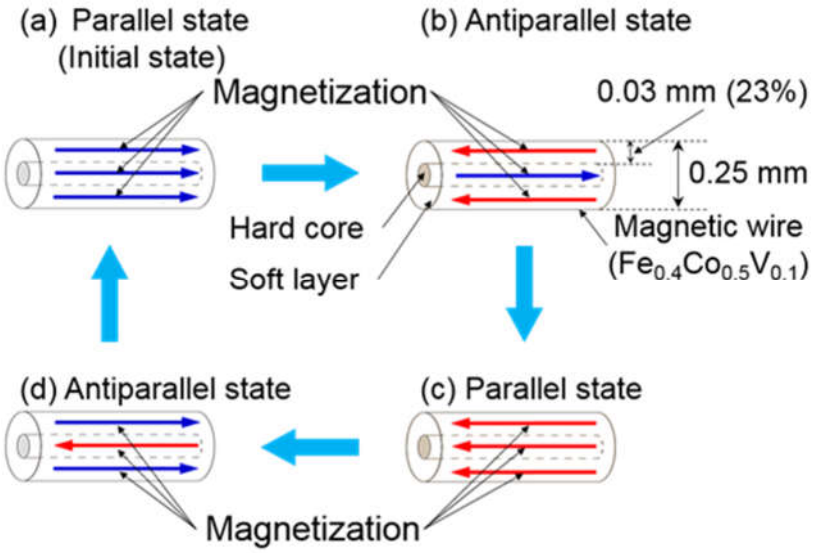

Figure 3.1 Magnetization states of the Wiegand wire in the (a, c) parallel state and (b, d) antiparallel state.

The magnetization reversal of the soft layer in Wiegand wire can be observed from the magnetization curves. In this research, the magnetization curves of normal major and minor hysteresis loops and FORCs were measured using a vibrating sample magnetometer (model 8600 series, Lake Shore Cryotronics, Westerville, OH, USA) at room temperature.

3.2 Magnetization Hysteresis Loop of Wiegand Wire and Its Analysis

3.2.1 Major Loop of Wiegand Wire

The measurement most commonly performed to characterize a material's magnetic properties is that of a major hysteresis loop. In this study, to extract comprehensive information on magnetic properties from the magnetic hysteresis curves, the major loop was measured with the Wiegand wire parallel and perpendicular to the applied magnetic field, as shown in Figure 3.2.

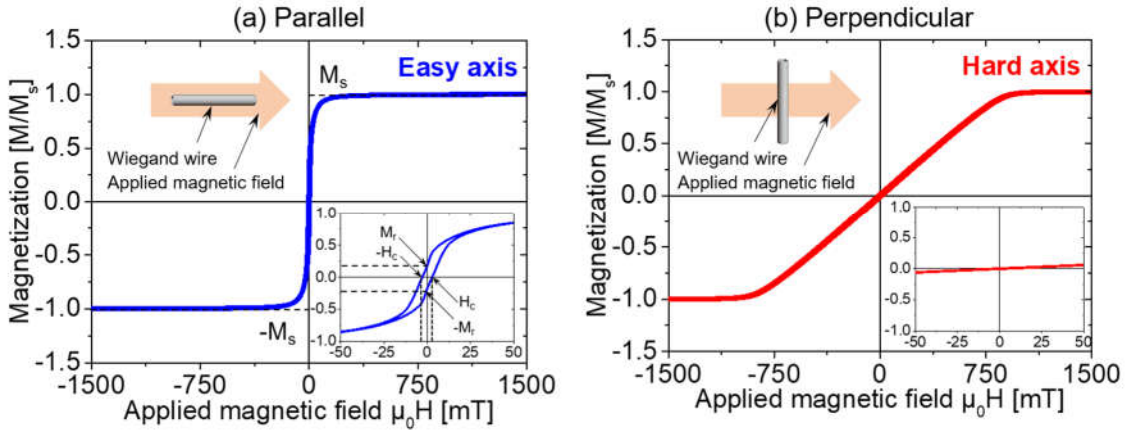

Figure 3.2 Major hysteresis loops of the Wiegand wire. The applied magnetic field is (a) parallel to the wire (easy axis), and (b) perpendicular to the wire (hard axis).

The normal and magnified views of the major loop in Figure 3.2(a) indicate that the sample exhibits remanent magnetization, and a coercive field of H_c = 3 mT/μ_0H. These results are in agreement with our previously reported results [18]. When the applied magnetic field is perpendicular to the Wiegand wire, the major loop is significantly narrower with negligible remanence or coercivity, as shown in Figure 3.2(b). This indicates that the Wiegand wire is anisotropic; the axis along the length is the easy axis of magnetization, and the axis along the diameter is the hard axis of magnetization. Therefore, it is difficult to achieve fast magnetization reversal when the Wiegand wire is perpendicular to the applied magnetic field, and hence, the Wiegand effect is not observed in this case. Consequently, the Wiegand pulse is not induced from the pick-up coil. This observation is consistent with previously reported results [33].

3.2.2 Minor Loops of Wiegand Wire

Because the Wiegand wire cannot effectively output energy on the hard axis, we studied only the magnetic properties of the Wiegand wire along the easy axis. The minor loops of the Wiegand wire, as traced with various maximum amplitudes of the applied magnetic field, are shown in Figure 3.3.

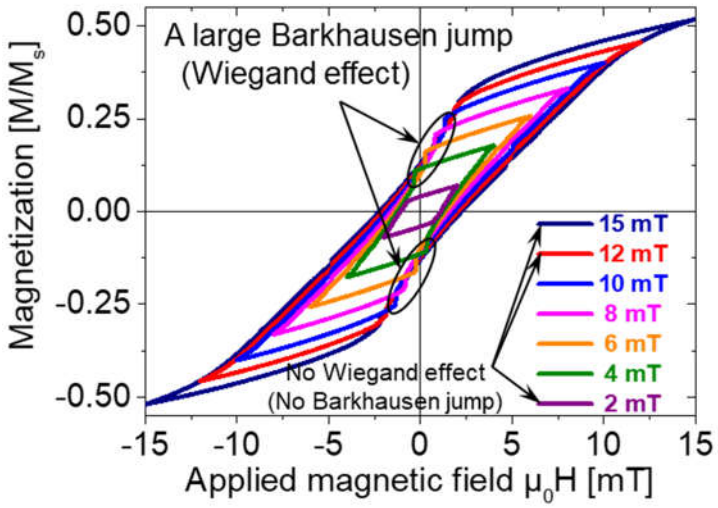

Figure 3.3 Minor hysteresis loops of the Wiegand wire (easy axis).

As shown in Figure 3.3, a fast magnetization reversal is observed in some limited minor loops. When the amplitude of the applied magnetic field is $\mu_0 H$ = 2, 12, or 15 mT, no Wiegand effect is observed. The coercive field of the soft layer is approximately $\mu_0 H$ = 2 mT [18-20]. Therefore, an applied magnetic field equivalent to or less than this value cannot reverse the magnetization of the soft layer, and the Wiegand effect is not observed. The coercive field of the hard core is approximately $\mu_0 H$ = 8 mT [18-20]. It has been reported that a fast magnetization reversal is not observed under an applied magnetic field larger than the coercive field of the hard core, although the reason for this is not clear. With an increase in the amplitude of the applied field the magnetic field that initiates the fast magnetization reversal of the soft layer is reduced, and becomes negative. This is caused by the demagnetizing field in the wire and the magnetostatic coupling between the soft layer and hard core, as described in Section 3.4.2.

3.2.3 Magnetization Process of Wiegand Wire

Figure 3.4 illustrates the relationship between the magnetization curve (minor loop) of the whole wire and the magnetization process of the Wiegand wire (FeCoV wire) used in this research. It can be seen from Figure 3.4 that the magnetization reversal is gradual in the hysteresis loop (magnetization curve) when measured with an applied static magnetic field of up to $\mu_0 H = 4$ mT. The hard core is magnetized completely until the wire reaches the saturation state, which occurs when the applied alternating magnetic field $\mu_0 H$ is greater than 15 mT.

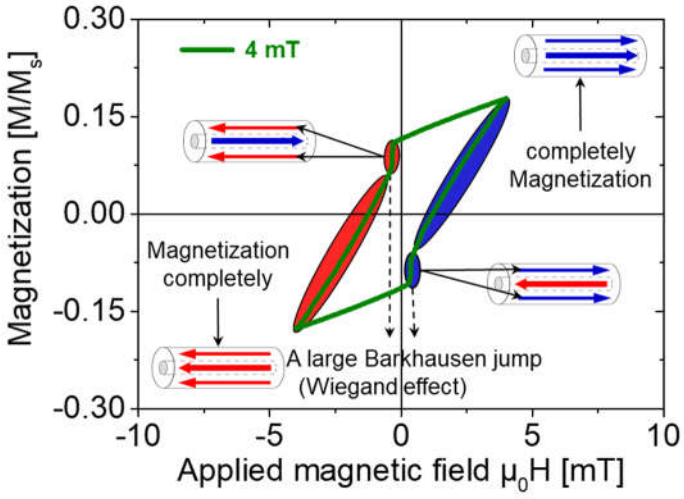

Figure 3.4 Relationship between the magnetization curve (minor loop) of the whole wire and the magnetization process of the Wiegand wire.

The steep change cannot be observed in the major loop. Therefore, for the Wiegand wire, it can be concluded that the minor loops can provide certain additional information relative to the major loop. The minor loops are located inside the major loop, so more complex magnetization curves covering states with applied magnetic fields and magnetization values located inside the major loop need to be used to characterize the magnetic properties of the Wiegand wire.

3.3 FORCs Measurement

3.3.1 FORCs of Wiegand Wire

As the Wiegand wire comprises components with different distributions of coercivity, an FORC analysis is an effective method to further investigate and clarify its magnetic properties. The FORC measurement method for magnetic materials is described in detail in Section 2.3.2. Figure 3.5 is an example of a FORC of the Wiegand wire at different applied reverse magnetic fields $\mu_0 H_a$.

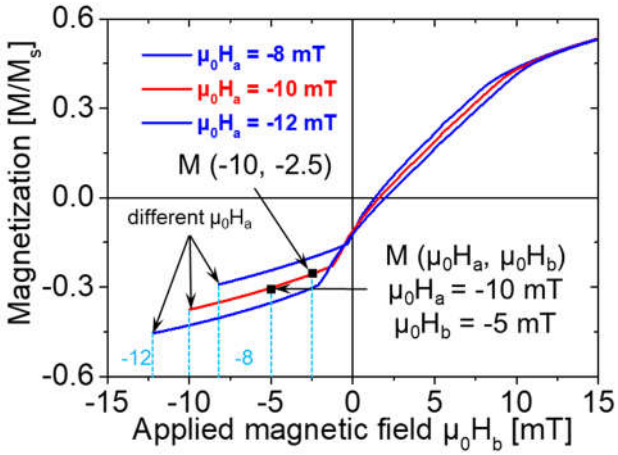

Figure 3.5 Example of an FORC of a Wiegand wire at different $\mu_0 H_a$. Two points of magnetization on the FORC, at two applied fields ($\mu_0 H_b$) with a reversal field ($\mu_0 H_a$), are represented by M ($\mu_0 H_a = -10$ mT, $\mu_0 H_b = -5$ mT) and M ($\mu_0 H_a = -10$ mT, $\mu_0 H_b = -2.5$ mT), respectively.

Normally, the FORCs are measured by first saturating the magnetic material in a large positive field ($\mu_0 H_{sat}$). The saturation field ($\mu_0 H_{sat}$) of the Wiegand wire used in this research is 1.8 T (provided by the supplier). Thus, a typical FORC of the Wiegand wire requires a large amount of magnetization data to be measured, and takes a large amount of time. However, the range of the applied magnetic field can be reduced to reduce the measurement time in the experiments, and the efficiency of the experiments can be improved. This is because, according to the previous conclusion in Section 3.2.3, the curves covering states with applied magnetic field and magnetization values that characterize the magnetic properties of the Wiegand wire are located inside the major loop. In addition, in the area near the saturation magnetic field, the outgoing path and

back path of the magnetization curve almost overlap. Therefore, this area contains very little effective information regarding the magnetic properties, and can be ignored. Furthermore, in the 8600 Series vibrating sample magnetometer, the FORC curves are measured after the magnetization of the sample is saturated to reset its history. Thus, the range of the applied magnetic field intensity can be reduced accordingly to increase the efficiency of the experiments.

In this research, to confirm the effectiveness of this experimental method and obtain a suitable range of the applied magnetic field intensity for the repeated experiments, FORC measurements of the Wiegand wire with applied magnetic field intensities $\mu_0 H$ ranging from -500 to 500 mT, -100 to 100 mT, -85 to 85 mT, -60 to 60 mT, -50 to 50 mT, and -10 to 10 mT were performed, separately. In all of the measurements, the step of the applied magnetic field was 0.5 mT, and the saturation field was set to 2 T.

The reasons for choosing so many ranges are that first, they can be used to compare the differences in experimental results under different ranges; moreover, if the method is effective, a suitable range can be obtained for subsequent repeated experiments. In particular, the reason for choosing the range from -500 to 500 mT is that according to the measurement results of the major loop in Section 3.2.1, the magnetization susceptibilities (M/M_s) of the Wiegand wire can reach 99.3% at the two measurement points of 500 mT and -500 mT. The Wiegand wire is basically completely magnetized; in this way, the experiment results from other different ranges have a comparison reference. Moreover, the time spent in this experiment is also acceptable at approximately 3 days, and when the range increases, the time required for the measurement becomes unacceptable. For example, when the intensity of the applied magnetic field $\mu_0 H$ is in the range of -1 to 1 T, the time is approximately 10 days at the same size of the field step.

3.3.2 FORC Diagram of Wiegand Wire

To intuitively compare the differences between the experimental results from different ranges of the applied magnetic field, the FORC diagrams are displayed in Figure 3.6.

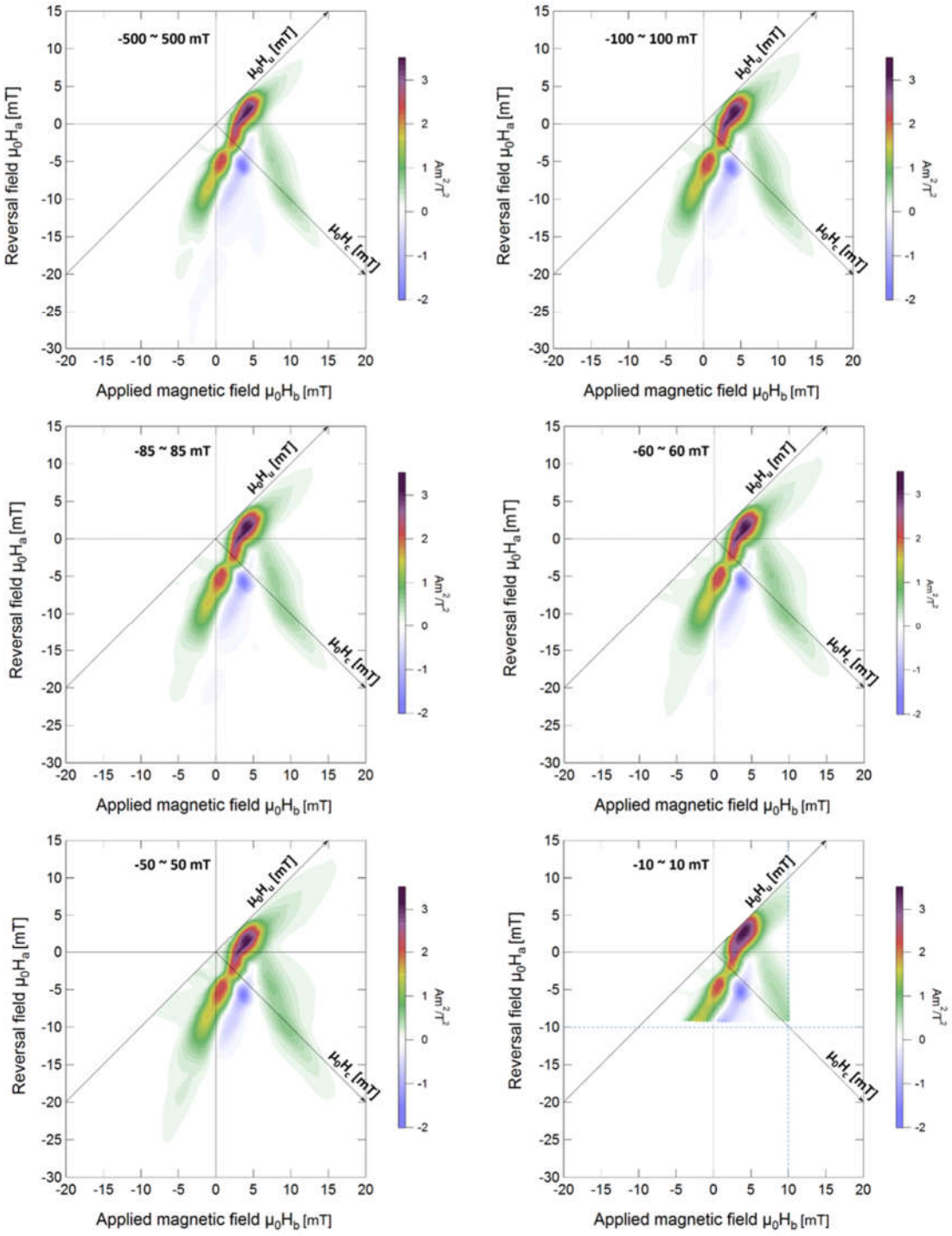

Figure 3.6 FORC diagrams under various applied magnetic fields.

As demonstrated in Figure 3.6, when the ranges of the applied magnetic field intensity $\mu_0 H$ are -500 to 500 mT, -100 to 100 mT, -85 to 85 mT, -60 to 60 mT, and -50 to 50 mT, the FORC distributions and resultant diagrams have no evident changes in their shape and key points, illustrating that the intensity of the applied magnetic field can be reduced accordingly in the experiment. Thus, it is not necessary to collect data on each individual ascending FORC branch all the way to saturation to obtain the FORCs and resultant diagram. However, when the intensity of the applied magnetic field is -10 to 10 mT, the information of the FORC distribution is missing, illustrating that the intensity of the applied magnetic field cannot be reduced indefinitely; when the FORCs generated by the applied magnetic field cannot cover the area surrounded by the major loop, the key information regarding the magnetic properties of the Wiegand wire will be lost. This also further proves the previous conclusion, i.e., that the magnetization curves covering states with applied magnetic field and magnetization values characterizing the magnetic properties of the Wiegand wire are located inside the major loop.

Overall, the effectiveness of this experimental method is verified, and a suitable range of the applied magnetic field intensity for the repeated experiments is obtained. In the experiments, it is necessary to obtain as much information as possible regarding the magnetic properties of the Wiegand wire; in addition, the time required for each experiment must be acceptable. Therefore, the experimental method in this work is determined as follows: the range of the applied magnetic field intensity is -50 to 50 mT, the corresponding step is 0.5 mT, and the saturation field is set to 2 T. The time required for the FORCs measurements is approximately 51 minutes. Figure 3.7 shows the measured FORC curves of the Wiegand wire from $\mu_0 H = -50$ to 50 mT.

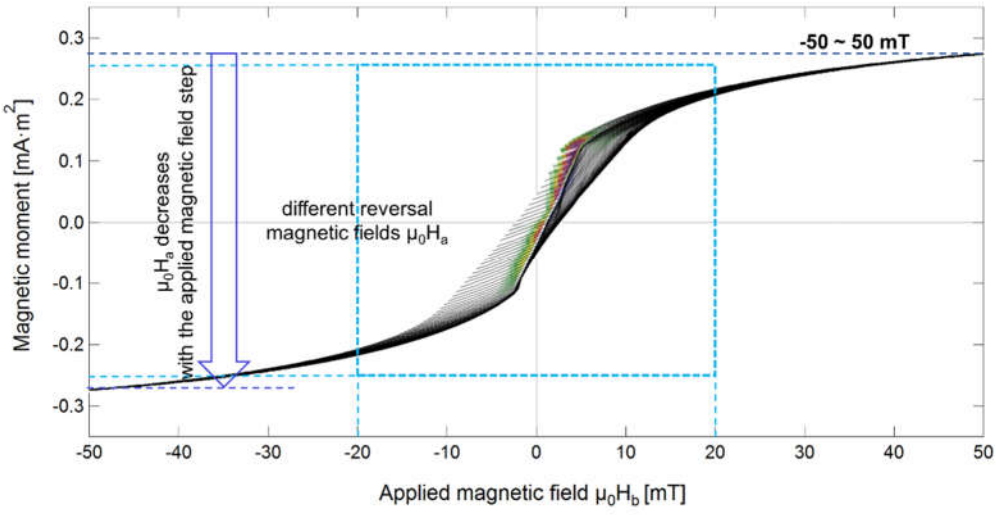

Figure 3.7 Measured FORC curves of the Wiegand wire from $\mu_0 H = -50$ to 50 mT.

To facilitate the analysis of the experimental results and obtain the magnetic properties of the Wiegand wire, a magnified snippet of the measured FORC curves from $\mu_0 H = -50$ to 50 mT and the FORC diagram as calculated from the measured FORC curves are shown in Figure 3.8.

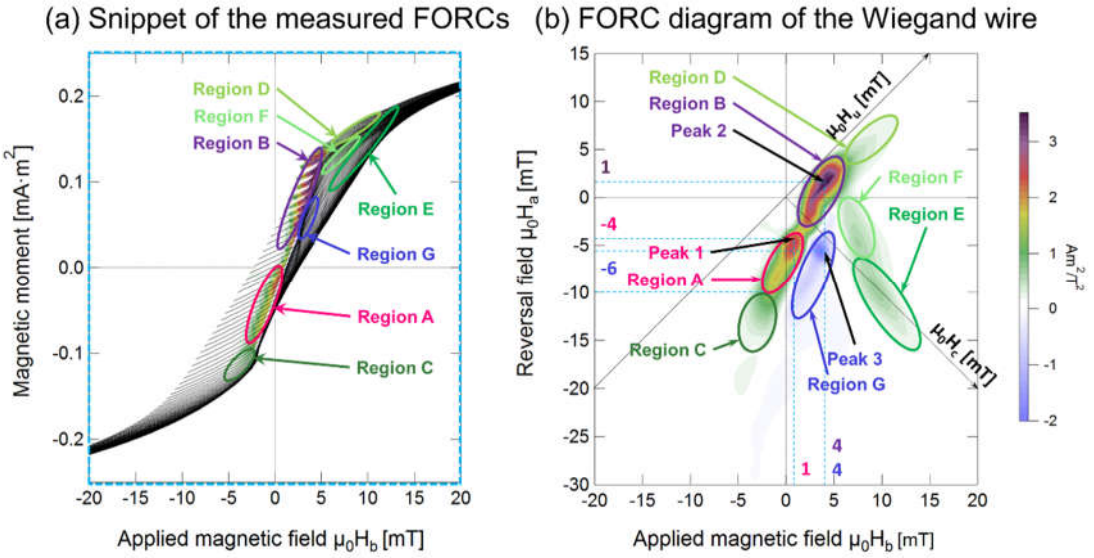

Figure 3.8 (a) Magnified snippet of the FORCs and (b) FORC diagram of the Wiegand wire measured under the applied magnetic field intensity range of −50 to 50 mT. The colors in (a) correspond to the intensity of the FORC distribution in (b).

3.4 FORC Analysis of Wiegand Wire

3.4.1 Two-Layer Magnetic Structure and Its Magnetization Reversal

The FORC diagram provides information on the magnetization process and magnetic interaction inside the sample [66-71]. As shown in Figure 3.8(b), two spot-like peaks are clearly observed. Peak 1, indicated in the figure, is located at $\mu_0 H_b = 1$ mT and $\mu_0 H_a = -4$ mT. Because the FORC distribution is calculated using the differential component of the gradient of the magnetization curve using Equation (2.6), it principally emphasizes an irreversible magnetization of the sample. Peak 1 can be broadened to reveal the area indicated as Region A in Figure 3.8(b). This region is also marked in the corresponding FORCs in Figure 3.8(a). Interestingly, it is evident from Figure 3.8 that the reversal fields of the magnetization in Region A are close to the applied alternating magnetic field at which a large Barkhausen jump occurs in the minor loops, as shown in Figure 3.3. The reversal field corresponding to Region A lies between $\mu_0 H_a = -4$ and -10 mT. This field range is consistent with the applied alternating magnetic field of ± 4 to 10 mT in which the Wiegand effect is observed, as shown in Figure 3.3. Peak 1 and Region A are attributed to the irreversible magnetization process of the soft axis, as accompanied by a large Barkhausen jump. Region C shows a continuously broadened distribution related to Region A. The magnetization reversal of the soft layer after the magnetization of the Wiegand wire is saturated in the negative direction by H_b. As the intensity of the FORC distribution is low, the magnetization process of the soft layer in Region C is almost reversible, and is not related to the Wiegand effect.

Peak 2 is located at $\mu_0 H_b = 4$ mT and $\mu_0 H_a = 1$ mT. Considering that this value of H_b lies between those of the coercive fields of the soft layer and hard core, Peak 2 and Region B correspond to the magnetization reversal of the intermediate layer between them, or to the interaction of the soft layer with the hard core. This magnetization process is irreversible because the intensity of the FORC distribution is high. Region D, with a low intensity FORC distribution and continuously adjacent to Region B, is attributed to the magnetization reversal of the soft layer, with an approximately reversible process.

Region E, observed in the range of $\mu_0 H_b > 5$ mT and $\mu_0 H_a < -8$ mT, is a long and narrow ellipse. It has a wide dispersion along the $\mu_0 H_c$ axis. This region is attributed to the magnetization reversal of the hard core, as H_b and H_a are sufficiently larger than the coercive field of the soft layer. The magnetization process is approximately reversible. The origin of Region F, which is centered at $\mu_0 H_b = 8$ mT and $\mu_0 H_a = -4$ mT, can be attributed to the magnetization reversal of the intermediate layer between the soft layer

and hard core, or the magnetization reversal of a partial region of the hard core. The magnetization reversal of the partial region of the hard core is automatically reversed by the corresponding demagnetizing field. Owing to the shape anisotropy, the demagnetizing field in the wire reverses both ends of the wire in the remanent state. The magnetization of the hard core at both ends of the wire is considered to be reversible and does not contribute to the FORC diagram (with a negligible intensity).

3.4.2 Interactions Between the Two Layers

Although there are different field components of the magnetization reversal in the Wiegand wire, when there are no interactions between these components, they generally form a peak or ridge along the zero-bias axis ($H_u = 0$) [61, 72]. However, it can be seen from Figure 3.8(b) that these are spread along the H_u axis of the FORC diagram of the Wiegand wire. The interactions between components can displace these components off the zero-bias axis, and/or can lead to the development of ridges [61, 73-74]. This indicates that there are interactions between these components, i.e., there are interactions between the soft layer and hard core of the Wiegand wire.

As shown in Figure 3.8(b), the interaction between the soft layer and hard core displaces the hard core from the zero-bias axis. This interaction can lead to the formation of a ridge indicating that Region F belongs to the hard core (Region E). If there is no interaction between the soft layer and hard core, then the FORC distribution that originates from the hard core would be located between Region E and F, instead of spreading out and developing into a ridge. This can also be observed in Figure 3.8(b), wherein the soft layer (Region A) and a part of the hard core (Region F) are not completely separated, and there is an intermediate layer, i.e., Region B, between them. This intermediate layer further indicates that the hard and soft layers interact with each other. Therefore, it can be concluded that the intermediate layer (Region B) develops because of the interaction between the soft layer and hard core of the Wiegand wire used in this study.

Owing to the presence of the intermediate layer (Region B), it can be determined that there is no clear boundary between the two layers in the Wiegand wire. The degree of the magnetization reversal field component spread along the H_u axis can be used to measure the strength of the interaction [70, 75-78]. It can be inferred that the interaction between the soft layer and hard core is strong, as shown in Figure 3.8(b).

3.4.3 Negative Region in the FORC Diagram

It can be seen from Figure 3.8(b) that the FORC diagram comprises two distinguishable parts: a positive FORC distribution (ρ (μ_0H_a, μ_0H_b) > 0) and negative FORC distribution (ρ (μ_0H_a, μ_0H_b) < 0). A peak is observed in the negative region (Region G, Peak 3), which is just below Peak 2, and is located at approximately μ_0H_b = 4 mT and μ_0H_a = −6 mT, as shown in Figure 3.8(b). The FORCs responsible for the negative region and its magnified view are shown in Figure 3.9.

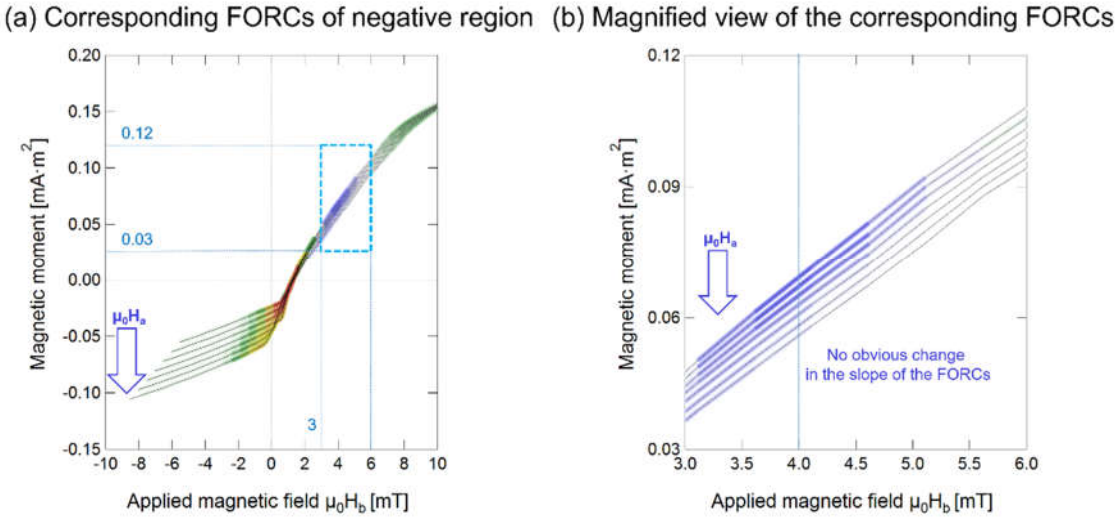

Figure 3.9 (a) FORCs responsible for the negative region (Region C) and (b) the magnified view.

The origin of the negative regions commonly seen in FORC diagrams has been previously discussed [79-81]. It is well-known that the negative region is an intrinsic feature of the FORC diagrams for noninteracting Stoner-Wohlfarth particles [79, 82-84]. The negative region of the FORC diagram of the Wiegand wire cannot be readily explained by this theory, as the position of the negative region is located far from the H_u axis [79-81] and just below the main peak, as shown in Figure 3.8(b). Carvallo et al. observed a negative region in the FORC diagram for hematite, a magnetite mixture, and a bimodal magnetite mixture sample [85-87]. However, these diagrams also could not explain the origin of the negative region in the FORC diagram of the Wiegand wire. The Wiegand wire used in this study had a typical composition of $Fe_{0.4}Co_{0.5}V_{0.1}$, i.e., not a mixture.

Muxworthy et al. explained the negative regions by the slope changes in the raw FORCs. Specifically, if the slope increases with decreasing μ_0H_a, then the distribution is greater

than zero. [87-90] When there is no change in the slope, the distribution is zero, and if the slope decreases, then the distribution is less than 0. [66, 91-93] Based on this conclusion, the original FORC data of the Wiegand wire were examined. However, the phenomenon of the slope change is not observed. At $\mu_0 H_b$ = 4 mT, each individual FORC curve branch of the Wiegand wire is approximately parallel the others, as illustrated in Figure 3.9(b). In other words, the FORCs parallel to each other indicate that the slope does not change, and the distribution ρ ($\mu_0 H_a$, $\mu_0 H_b$) is zero, not less than zero. Therefore, this observation cannot explain why the distribution of Wiegand wires in this region is less than zero.

In the FORCs shown in Figure 3.7 and 3.8(a), it can be seen that the part with a distribution less than zero appears between the soft layer and hard core and that there is a strong interaction between the soft layer and hard core, as discussed previously. Therefore, it can be inferred that the negative region in the FORC diagram of the Wiegand wire also appears owing to the interactions between the soft and hard cores. Pike et al. quantitatively showed that these interactions can produce a negative region in the FORC diagram [70, 93-95]. Therefore, it was important to elucidate if the presence of the negative region of the FORC diagram, as observed in this work, was owing to the interactions between the soft layer and hard core of the Wiegand wire, as explained before.

3.5 Summary

In this chapter, the magnetization properties of a Wiegand wire were examined using FORC diagrams and magnetic hysteresis curves. The magnetic properties of the Wiegand wire were successfully clarified through a detailed analysis of the prominent features in its FORC diagram. It was found that the magnetization process of the soft layer is an irreversible process. The switching field and intensity range of the applied magnetic field for producing the Wiegand effect with a large Barkhausen jump corresponded well with both the minor hysteresis curves and FORC diagram. An irreversible magnetization process of the soft layer, not accompanied by a large Barkhausen jump, was also observed in the FORC diagram. The magnetization of the hard core was almost reversible. The magnetization of the intermediate region between the soft layer and hard core, which was also interpreted as the soft layer interacting with the hard core, was observed in the FORC diagram. These results provide evidence for the magnetic structure of the Wiegand wire, which cannot be elucidated using conventional magnetization hysteresis curves.

Chapter 4: Pulse Voltage from Wiegand Wire with Magnetic Flux Guidance

This chapter presents the research results regarding the factors affecting the energy of the Wiegand pulse. To meet the power consumption requirements, it is necessary to maximize the energy of the pulse voltage from the Wiegand wire without changing the external field conditions. In this study, the main factors affecting the energy of a pulse voltage were determined by setting ferrite beads for both ends of the Wiegand wire, changing the position of the pickup coil around the Wiegand wire, and adjusting the direction of the Wiegand wire in the applied magnetic field. Meanwhile, an appropriate configuration for the Wiegand sensor made of the Wiegand wire was chosen so as to maximize the energy of the pulse voltage, without changing the external field conditions.

4.1 Energy of the Pulse Voltage

A Wiegand wire with a length of 11 mm was used in this work. When the Wiegand wire was placed in an alternating magnetic field, the pickup coil repeatedly output the alternating pulses. A magnetization reversal of the soft layer (from the antiparallel to the parallel state) against the hard core was observed by applying an asymmetric field [18, 96].

To reach either antiparallel state, a magnetization reversal occurs in the soft layer to induce a pulse of several volts and duration of 10 μs in the pickup coil placed around the Wiegand wire, as illustrated in Figure 4.1. However, the polarity of the voltage pulse is the opposite between these two cases: one is negative and the other is positive, depending on the initial magnetization state of the wire and the direction of the pickup coil around it. In this experiment, a pickup coil with a length of 5 mm and 2,000 turns was used. The external excitation magnetic field was applied by a magnet (NdFeB) with a diameter of 4 mm and length of 6 mm. The magnetization direction of the magnet was along the axis.

Typically, the rotation of a pair of magnets or a single magnet is used to apply an alternating magnetic field to a wire. In this research, a pair of magnets was used. All of the waveforms of the pulse voltage were measured as an open circuit voltage across the pickup coil of the Wiegand wire.

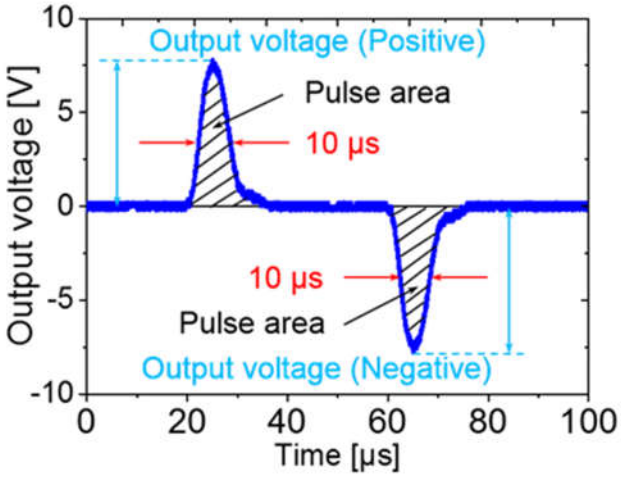

Figure 4.1 Pulse voltage induced by magnetization reversal of the soft layer in the Wiegand wire.

The energy of the signal can be expressed as follows:

$$E = \int_{-\infty}^{+\infty} |V(t)|^2 d_t \tag{4.1}$$

In this study, the energy of the pulse voltage (Wiegand pulse) was calculated based on the discrete data points determined by the oscilloscope. It can be seen from Equation (4.1) that the energy of the Wiegand pulse is equal to the sum of the product of the squares of the magnitudes for all discrete points and the time axis. In other words, the energy of the Wiegand pulse is proportional to the area of the shaded part in Figure 4.1. Because the width of the Wiegand pulse does not depend on the intensity of the applied magnetic field or frequency of the magnetic-field change, the larger the voltage, the larger the pulse area and the corresponding energy of the Wiegand pulse.

4.2 Enhance the Magnetic Flux

4.2.1 Install the Ferrite Beads

Air's ability to collect magnetic flux is weak, as the magnetic path diverges in air. In contrast, a ferrite material is more capable of collecting magnetic flux. Therefore, in the experiments aiming to enhance the magnetic flux at the center of the Wiegand wire, a ferrite bead was set at both ends of the Wiegand wire, as presented in Figure 4.2. Figure 4.2(a) shows a model without ferrite beads, referred to as the "Without beads" model. Figure 4.2(b) shows the model with ferrite beads, referred to as the "With beads" model. The inner and outer diameters of the ferrite beads (TDK, Co. Ltd., Japan, HF57BB3.5X3X1.3) used in the study were 1.3 and 3.5 mm, respectively, the length was 3 mm, and their main metallic elements were Ni, Zn, and Fe.

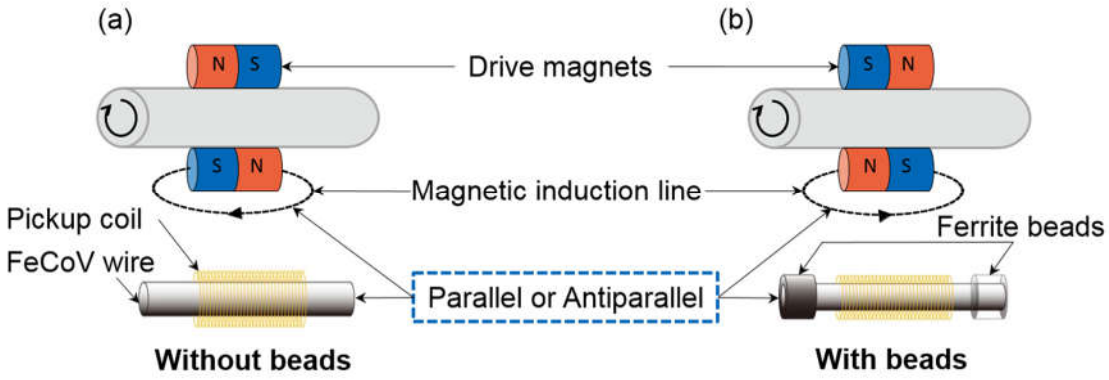

Figure 4.2 Experimental models: (a) "Without beads" model and (b) "With beads" model.

To study the effects of the magnetic flux density through the center of the Wiegand wire with respect to the energy of the Wiegand pulse, the applied external magnetic-field intensity $\mu_0 H$ was set to between 4 and 8 mT for both models. Meanwhile, to prove that the ferrite material was more capable than air for collecting the magnetic flux density, the two models used the same pickup coil and the same external magnetic field. The experimental results from the two models were compared for each additional 1 mT. The pickup coil was wound 200 turns around the Wiegand wire, and its length was 5 mm.

4.2.2 Simulate the Distribution of the Magnetic Flux

Before the experiments, the magnetic flux density through the center of the Wiegand wire was simulated by a finite element analysis using ANSYS Maxwell®(ANSYS, Inc., USA). In the simulation, the 3D models of the magnet, Wiegand wire, ferrite beads, and air field were defined.

The distance from the surface of the magnet to the center of the Wiegand wire was 5 mm. The dimensions of the magnet, Wiegand wire, and ferrite beads were designed according to the samples used in the experiments, and the air field was designed as a cylinder with a radius of 40 mm and height of 80 mm. The maximum length of the elements of the Wiegand wire, ferrite beads, magnet, and air field were set to 0.3, 0.3, 0.5, and 0.5 mm in the mesh operations, respectively.

The corresponding materials were determined according to the samples, as follows.

"NdFe35" was chosen for the magnet from the material database of the software, and the default parameters were used.

A material named FeCoV was defined for the Wiegand wire. Its relative permeability and saturation magnetic flux density were 20 and 1.8 T, respectively, as provided by the supplier (SWFE, Co. Ltd., Meishan, China).

The "ferrite" material in the material database was selected for the ferrite beads, and the parameters were modified according to the sample datasheet of the supplier (TDK, Co. Ltd., Japan).

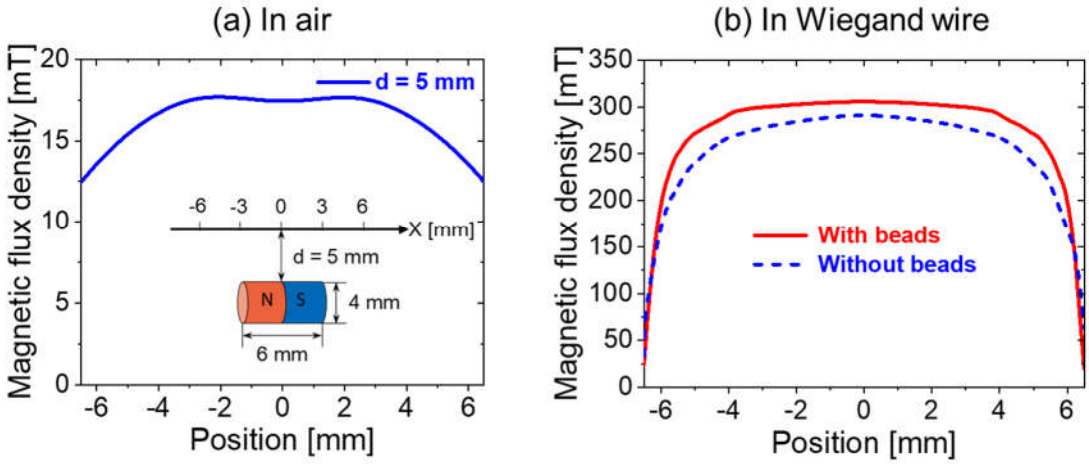

Figure 4.3. Simulation results of the magnetic flux density in the air and the Wiegand wire: (a) in the air and (b) in the Wiegand wire.

The simulation results in Figure 4.3(a) show the magnetic field distribution at a distance of 5 mm from the surface of the magnet used in this study. The simulation results in Figure 4.3(b) show the magnetic flux density through the center of the Wiegand wire in the “With beads” model and “Without beads” model. The results of Figure 4.3(b) verify that the magnetic flux density through the center of the Wiegand wire is increased by setting ferrite beads at both ends of the Wiegand wire. This is achieved without changing the intensity of the external magnetic field. This demonstrates the feasibility and effectiveness of the experimental method used herein.

4.2.3 Pulse Voltage Induced by Different Magnetic Flux Densities

It can be observed from Figure 4.4 that the amplitude and area of the pulse voltage from the Wiegand wire increases with an increase in the applied magnetic field. This is irrespective of whether or not the ferrite beads are installed at both ends of the Wiegand wire. The reason for this result is that the volume of the reversed soft layer increases against the hard core based on the increase in the external excitation magnetic field. When all of the soft layer and hard core are antiparallel, the amplitude and area of the pulse will reach a maximum. They will also not increase with a further increase in the external magnetic field. In summary, the increases in the amplitude and area of the pulse are attributed to the increase in the volume of the reversed soft layer against the hard core.

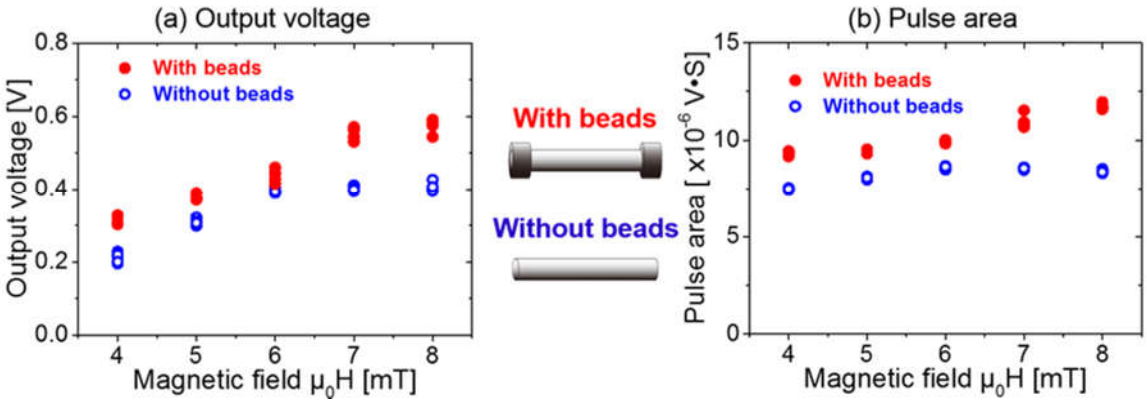

Figure 4.4 Comparison of the experimental results of the amplitude and the area of the pulse voltage with or without ferrite beads, displaying: (a) output voltage and (b) pulse area. (The meanings of amplitude and area of the pulse are described in Figure 4.1).

However, the amplitude and area of the pulse voltage are larger when using ferrite beads than those without ferrite beads. This suggests that the ferrite beads at both ends of the wire are capable of increasing the magnetic flux density through the center of the Wiegand wire. Therefore, the volume of the magnetically reversed soft layer is increased, and the amplitude and area of the pulse increase.

Thus, the experimental results show that the addition of ferrite beads at both ends of the Wiegand wire, without changing the external magnetic field, increases the volume of the reversed soft layer against that of the hard core. The amplitude and area of the Wiegand pulse increase, thereby improving the energy of the pulse voltage.

4.3 Magnetic Flux Guidance at Different Positions of the Wiegand Wire

4.3.1 Change the Position of the Pickup Coil

To analyze the relationship between the position of the pickup coil and the energy of the pulse voltage, a 1-mm-long pickup coil was wound 50 times around the Wiegand wire, and an external magnetic field with an intensity of 4 mT was applied. In the initial state, the pickup coil was located at the center of the Wiegand wire, and was moved by a 1-mm step to the right for both models. The pulse waveforms induced by the pickup coil at different positions were measured for the different models. The schematic for the position measurement is shown in Figure 4.5.

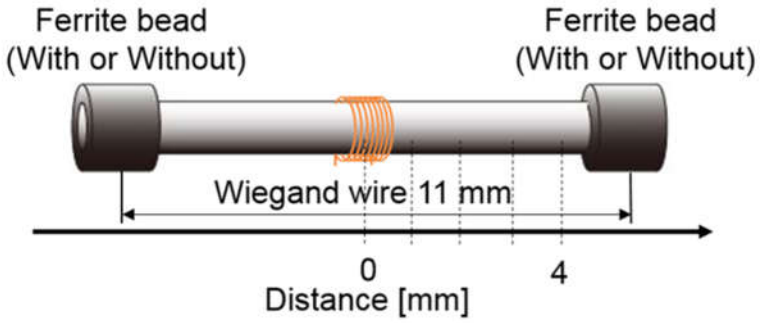

Figure 4.5 Schematic for position measurement.

4.3.2 Pulse Voltage at Different Positions of Wiegand Wire

As shown in Figure 4.6, as the distance between the pickup coil and Wiegand wire center increases, the amplitude and area of the Wiegand pulse decrease. In other words, the energy of the pulse voltage decreases. To analyze the causes of this phenomenon, the magnetic field distributions were simulated at a distance of 5 mm from the surface of the magnet applied in the study, as demonstrated in Figure 4.3(a).

It can be seen from Figure 4.3(a) that the magnetic field is strong in the middle and weak at both ends. This makes the volume of the reversed soft layer against the hard core larger at the center of the Wiegand wire and smaller at both ends. Therefore, the amplitude and area of the pulse as detected by the pickup coil are the largest at the center of the Wiegand wire, and show a decreasing trend towards both ends. When the pickup coil is at the center of the Wiegand wire, the detected energy of the Wiegand pulse is at its maximum.

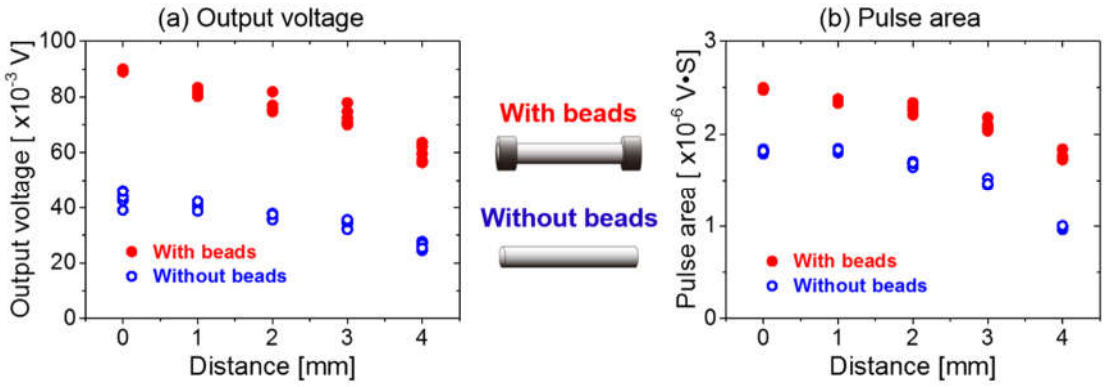

Figure 4.6 Experimental results of the relationship between the amplitude and area of the Wiegand pulse and the position of the pickup coil, displaying: (a) output voltage and (b) pulse area.

It can also be demonstrated from Figure 4.6 that, irrespective of where the pickup coil is placed around the Wiegand wire, the amplitude and area of the pulse output are larger when using the ferrite beads. This further verifies that the setting of the ferrite beads at both ends of the Wiegand wire can improve the volume of the reversed soft layer against the hard core, thereby improving the energy of the pulse.

4.4 Magnetic Flux Guidance of the Wiegand Wire at Different Angles

4.4.1 Adjust the Angle of the Wiegand Wire in the Magnetic Field

To obtain the relationship between the angle of the Wiegand wire and the magnetic induction line, as well as the energy of the pulse voltage, the waveforms of the pulse voltage were detected by the pickup coil. These were measured under the rising and falling triggering modes of the oscilloscope. The angles (between the Wiegand sensor and the magnetic induction line) were 0°(360°), 30°(330°), 45°(315°), 60°(300°), 90°(270°), 120°(240°), 135°(225°), 150°(210°), and 180°, for both models ("With beads" and "Without beads"). The angle (theta) diagram of the Wiegand wire in the magnetic field is illustrated in Figure 4.7. The waveforms were then analyzed and compared. The pickup coil was wound 500 times around the Wiegand wire, and its length was 5 mm. The distance between the magnet surface and the center of the pickup coil was 5 mm.

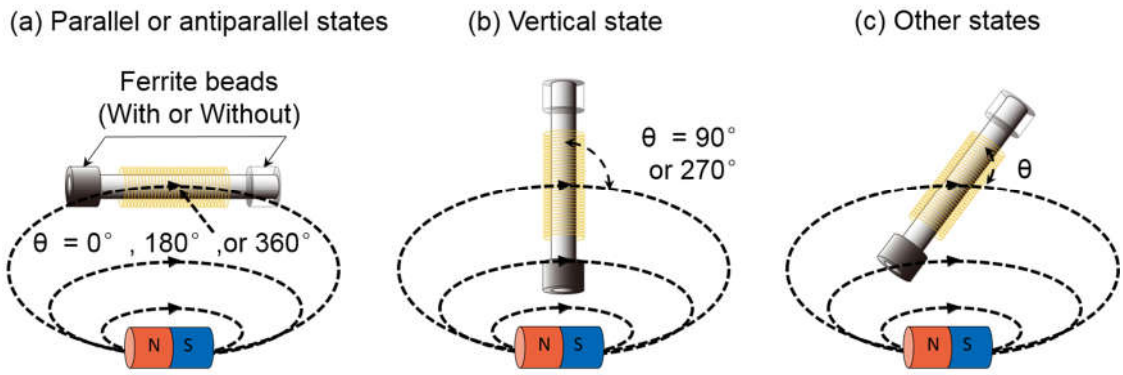

Figure 4.7 Angle (theta) diagram of the Wiegand sensor in the magnetic field: (a) parallel or antiparallel states, (b) vertical state, and (c) other states.

4.4.2 Pulse Voltage of Wiegand Wire at Different Angles

Figure 4.8 displays the positive and negative peak-to-peak voltages of the Wiegand wire, from 0° to 360° for both the "With beads" and "Without beads" models. The abscissa in Figure 4.8 represents the angle between the Wiegand wire and the magnetic induction line. The ordinate represents the peak-to-peak voltages of the Wiegand pulse for the corresponding angle.

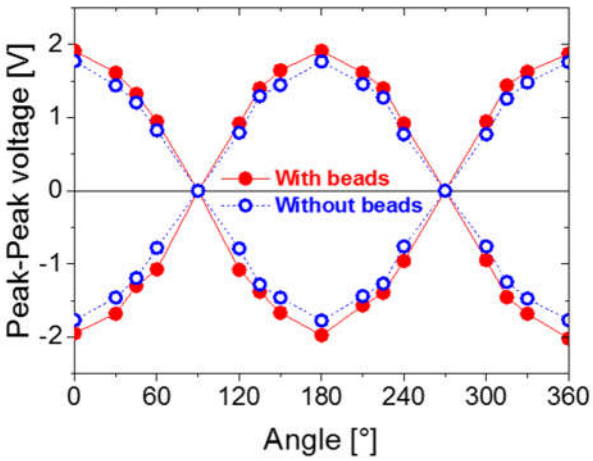

Figure 4.8 Experimental results of the relationship between the angle of the Wiegand wire in the applied magnetic field and peak-to-peak voltage of the voltage pulse from the Wiegand wire.

As demonstrated from Figure 4.8, at the angles of 0°, 180°, and 360° between the Wiegand wire and magnetic induction line (in the parallel or antiparallel states), the peak-to-peak value of the Wiegand pulse is at its maximum. In other words, the output energy is at its maximum. In contrast, when the angle becomes 90° or 270° (in a vertical state), the peak-to-peak value of the Wiegand pulse is at a minimum; thus, the energy output is at its minimum.

In other words, the magnetic induction lines that are parallel or antiparallel can excite the Wiegand wire successfully, whereas those in the vertical state cannot. The Wiegand wire and magnetic induction line are not in a parallel or antiparallel state, and they are inclined at a certain angle. As a result, the magnetic induction lines that excite the Wiegand wire to output the Wiegand pulses are the parallel or antiparallel components of the magnetic induction lines with a particular angle to the Wiegand wire.

Furthermore, the intensity of the effective magnetic field applied to the Wiegand wire is reduced. That is, the magnetic field, which reverses the soft layer, is reduced, and the volume of the reversed soft layer becomes reduced. As a result, the peak-to-peak voltage of the Wiegand pulse decreases. However, when the direction of the applied magnetic field is parallel or antiparallel to the Wiegand wire, the peak-to-peak voltage of the Wiegand pulse reaches its maximum. The experimental results shown in Figure 4.6 support this analysis. Both the positive and negative peak-to-peak voltages of the Wiegand wire in the “With beads” model are larger than those in the “Without beads” model. Therefore, setting the ferrite beads is advantageous for the practical applications of the Wiegand wire concerning power supply.

4.5 Summary

In this chapter, the energy of the Wiegand pulse was described. Through a large number of experiments, the factors affecting the energy of the Wiegand pulse were determined, and their relationships with the energy of the Wiegand pulse were successfully stated. The magnetic flux through the center of the Wiegand wire increased after ferrite beads were set at both ends of the Wiegand wire. The simulation results predicted an increase in the magnetic flux density, and it could be estimated that the energy of the Wiegand pulse increased in a corresponding manner. When the pickup coil was closer to the center of the Wiegand wire, the angle between the Wiegand sensor and magnetic induction line was smaller, and the energy of the Wiegand pulse was larger.

The essential relationship between these factors and the energy of the Wiegand pulse was determined to have an effect on the volume of the reversed soft layer against the hard core. For the same Wiegand wire, same pickup coil, and same external excitation conditions, a larger volume of the reversed soft layer against the hard core could produce a Wiegand pulse with greater energy.

When using the Wiegand sensor in practical applications, ferrite beads should be set at both ends of the Wiegand wire to increase the magnetic flux density. The pickup coil on the Wiegand wire should be distributed evenly on both sides, with the center as the origin. In addition, when the Wiegand sensor is used as a power supply, it should be ensured that the magnetic induction line and Wiegand sensor are parallel or antiparallel, so as to obtain the maximum energy.

Chapter 5: Pulse Generation in Wiegand Wire Excited by Various Magnetic Fields

This chapter presents the research results regarding the magnetization characteristics of the magnetic wire as excited by various typical magnetic fields. These typical magnetic fields are produced by a rotating magnet with radial magnetization, a pair of rotating bar magnets with axial magnetization, and a solenoid coil with AC current. The initial position, propagation direction and velocity, and degree of magnetization reversal of the soft layer in the Wiegand wire are successfully described. Meanwhile, placing ferrite beads at both ends of the wire is found to increase not only the degree but also the propagation velocity of the magnetization reversal in the soft layer of the Wiegand wire.

In this work, the magnetization characteristics refer to the position of the initial magnetization reversal, direction and velocity of its propagation, and degree of magnetization reversal (volume of the soft layer exhibiting this reversal) in the soft layer of the magnetic wire. These characteristics can be analyzed by the amplitude, area, and timing of the pulse generated in the pickup coils under different applied magnetic fields.

5.1 Configuration of Wiegand Wire

A Wiegand wire with a length of 13 mm was used in this work. From the above description, when a Wiegand wire is placed in an external alternating magnetic field, alternating Wiegand pulses are repeatedly generated in the pickup coil placed around it, and the pulse amplitude is independent of the change rate of the external field. In this study, all of the waveforms of the pulse were measured as open circuit voltages by the pickup coils around the Wiegand wire. The experimental data in the figures are the averages over five measurements. The meanings of the output voltage and its area were described in Figure 4.1.

The voltage pulse output from the pickup coil around the Wiegand wire increases after ferrite beads are set at both ends of it, as previously reported in detail [33]. Therefore, two experimental models of the Wiegand wire (“Without beads” and “With beads," i.e., Figure 5.1(a) and Figure 5.1(b), respectively) were employed in this work to comprehensively analyze the magnetization characteristics of the Wiegand wire. The Wiegand wire models with and without beads were both subjected to the different types of external magnetic

fields. The inner and outer diameters of the ferrite beads (TDK, Co. Ltd., Japan, HF57BB3.5X3X1.3) were 1.3 and 3.5 mm, respectively; their length was 3 mm, and the main metallic elements were Ni, Zn, and Fe.

To obtain the Wiegand wire's magnetization characteristics at a resolution of 1 mm, Wiegand wire models with and without the beads were measured with the same pickup coil placed at every 1 mm. As the ferrite beads occupied 6 mm of the wire, seven identical pickup coils were distributed along the Wiegand wire. Each pickup coil was 0.9 mm long and had 200 turns, and the distance between the centers of two adjacent coils was 1 mm. Thus, the seven coil centers were located at X = -3, -2, -1, 0, 1, 2, and 3 mm along the Wiegand wire, as displayed in Figure 5.1.

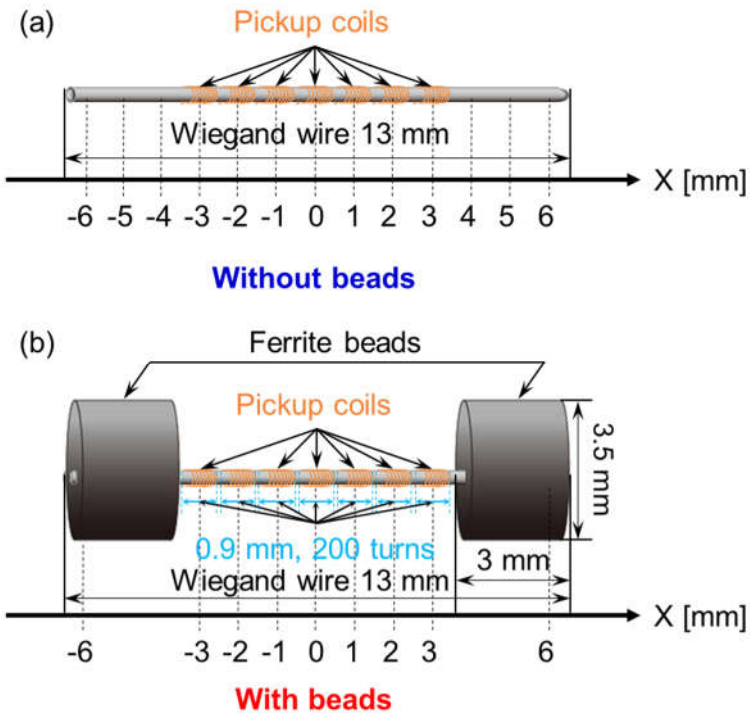

Figure 5.1 Experimental models of the Wiegand wire: (a) Without beads model and (b) With beads model.

5.2 Various Excitation Magnetic Fields

Typically, the alternating magnetic field is generated by rotating a single radial magnet or a pair of axial magnets [97, 98], or by passing an AC current through a spiral coil. Usually, a single rotating radial magnet is used for the encoder, a pair of rotating axial magnets is used for rotation sensing, and a spiral coil carrying AC current is used to create a uniform excitation magnetic field. These setups are involved in most applications for the Wiegand sensor, and therefore, they were separately applied to the Wiegand wire in this work.

To demonstrate that the Wiegand sensor could work at an extremely low frequency in the alternating magnetic field, the rotational frequency of the external magnets and frequency of the applied AC current were set to 60 rpm and 1 Hz, respectively. Meanwhile, to study the effect of the applied magnetic field intensity on the magnetization characteristics, the intensity at the center of the wire was set at $\mu_0 H$ = 6 or 10 mT by adjusting either the distance from the external magnet(s) or the AC current in the spiral coil. The specific distances (d) and currents (I) were determined by measuring the actual intensity of the applied magnetic field with a Gauss meter.

5.2.1 Single Rotating Radial Magnet

A single rotating external magnet (NdFeB) with a diameter of 8 mm and height of 1 mm was used. The magnetization direction of the magnet was along its radius. In practical applications, this setup may be used in encoders such as linear encoders, angular encoders, and position measurement systems. To completely analyze the magnetization characteristics of the magnetic wire in the Wiegand sensor as excited by this field, the external magnet was driven by a motor to rotate. In this setup, the rotation angle of $\theta = 0°$ was defined as shown in Figure 5.2.

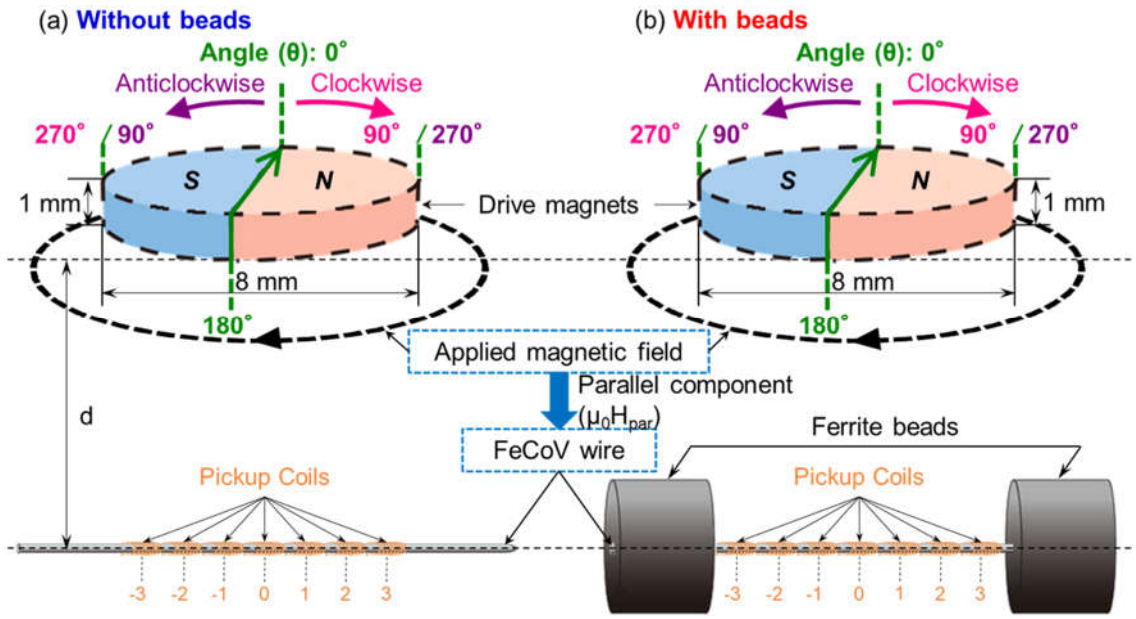

Figure 5.2 Experimental schematic for the single radial magnet applied to the models: (a) “Without beads” and (b) “With beads.”

5.2.2 Pair of Rotating Axial Magnets

In this setup, a pair of axial magnets were placed on one side of the Wiegand wire. Each of the pair of axial magnets (NdFeB) had a diameter of 4 mm and length of 6 mm, and their magnetization direction was along their axis (Figure 5.3). This method is widely used for rotation sensing, such as for robot motion (position and speed), car control, and other rotation applications.

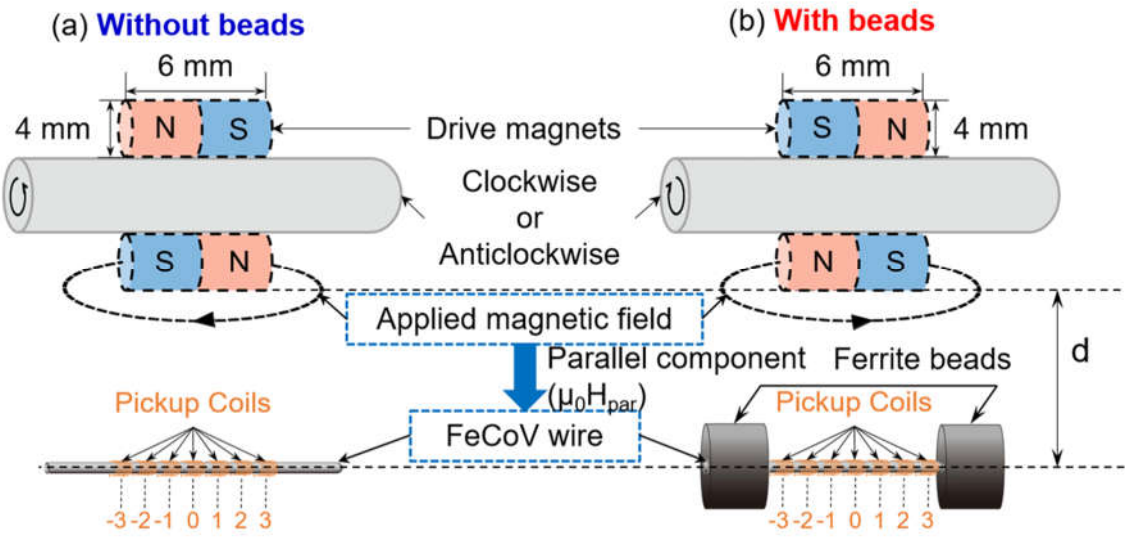

Figure 5.3 Experimental schematic for the pair of axial magnets applied to the model: (a) "Without beads" and (b) "With beads."

5.2.3 Spiral Coil Carrying AC Current

The third type of applied magnetic field was generated by a spiral coil (exciting coil) carrying an AC current. This configuration, which generates a uniform magnetic field, is important for magnetic resonance imaging units, and is most commonly seen in physics research involving charged particles. The magnetic wire (with or without the ferrite beads) was placed at the center of the spiral coil (inner diameter of 14 mm, length of 21 mm, and 750 turns), as shown in Figure 5.4.

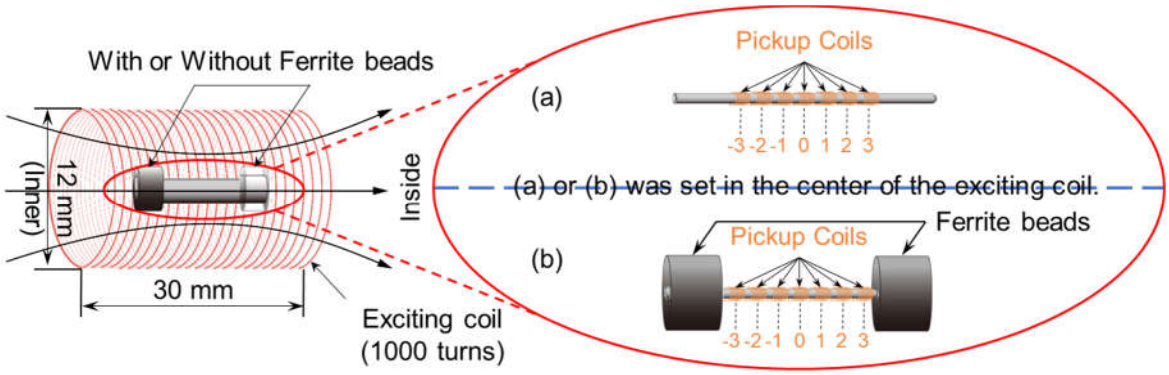

Figure 5.4 Experimental schematic for the exciting coil containing the magnetic wire model: (a) “Without beads” and (b) “With beads.”

5.2.4 Simulation of the Applied Magnetic Fields

Before the experiments, the applied magnetic field intensity and magnetic flux density through the center axis of the magnetic wire were simulated by a finite element analysis using ANSYS Maxwell® (ANSYS, Inc., USA), employing 3D models for the external magnet (single radial magnet or single axial magnet), magnetic wire, ferrite beads, exciting coil, and air field. The distance (d) between the surface of the external magnet and the axis of the magnetic wire was 6.7 mm for the radial magnet and 6 mm for the axial magnet, and the current (I) through the spiral coil was 280 mA. These settings ensured that the intensity of the applied magnetic field in the simulation equaled the experimentally measured value of $\mu_0 H = 10$ mT.

The dimensions of the magnets, magnetic wire, ferrite beads, and exciting coil were designed to match the actual objects, and the air field was assumed to be a cylinder. In the simulation of the magnets, the radius of the cylinder was 40 mm and the height was 80 mm, and in the simulation of the coil, the radius of the cylinder was 80 mm and the height was 120 mm. In the mesh operations, the maximum lengths of the elements in the magnetic wire, ferrite beads, axial magnets, radial magnet, exciting coil, air field of the magnet simulation, and air field of the coil simulation were set to 0.1, 0.2, 0.3, 0.3, 1, 0.5, and 3 mm, respectively.

The materials in the simulation were also determined according to the physical samples. A material named “NdFe35” in the material database was selected for the magnet, and default parameters were used. A material named FeCoV was defined for the magnetic wire, and the respective relative permeability and saturation magnetic flux density of the magnetic wire were defined as 20 and 1.8 T, respectively. The simulation parameters of the magnetic wire were provided by the supplier (SWFE, Co. Ltd., Meishan, China). “Ferrite” in the material database was selected for the ferrite beads, and the parameters were modified according to the sample datasheet of the supplier (TDK, Co. Ltd., Japan). “Copper” in the material database was selected for the exciting coil; the number of turns was set to 1000, and the current was set to 280 mA.

According to the conclusion of Section 4.4.2, the magnetic induction lines that excite the Wiegand wire to output the Wiegand pulses are the parallel or antiparallel components of the magnetic induction lines. Therefore, the intensities of the parallel or antiparallel components of the three applied magnetic fields in the work were simulated, as shown in Figure 5.5. Figure 5.5(a) shows the magnetic field intensity through the center axis of the magnetic wire as a function of the position along the wire when the rotation angle goes from 0° to 180° and from 180° to 360°, respectively. As can be seen from Figure 5.5(a),

when the radial magnet rotates from 90° to 120°, the polarity of the applied magnetic field changes, and the applied magnetic field intensity $\mu_0 H$ at an angle of 120° is greater than the coercivity ($\mu_0 H$ = 2 mT) of the soft layer of the Wiegand wire. This means that a pulse is generated between 90° and 120°. It can also be inferred that a pulse of the opposite polarity is generated between 270° and 300°. To obtain the angle of the generated pulse, the applied magnetic field intensities from 90° to 120° and from 270° to 300° were simulated with a resolution of 1°, respectively. From Figure 5.5(a), when the rotation angle is 100° and 280°, the reverse applied magnetic field intensity is approximately $\mu_0 H$ = 2 mT. Therefore, during the rotation of the radial magnet, two Wiegand pulses with opposite polarities occur at angles of 100° and 280°, respectively. The simulation results in Figure 5.5(b) and 5.5(c) indicate the magnetic field distribution along the magnetic wire when excited by the rotating axial magnet and exciting coil, respectively.

These simulation results can be used to predict the magnetization characteristics (initial position, propagation direction, and degree of magnetization reversal) of the Wiegand wire in the Wiegand sensor excited by these fields.

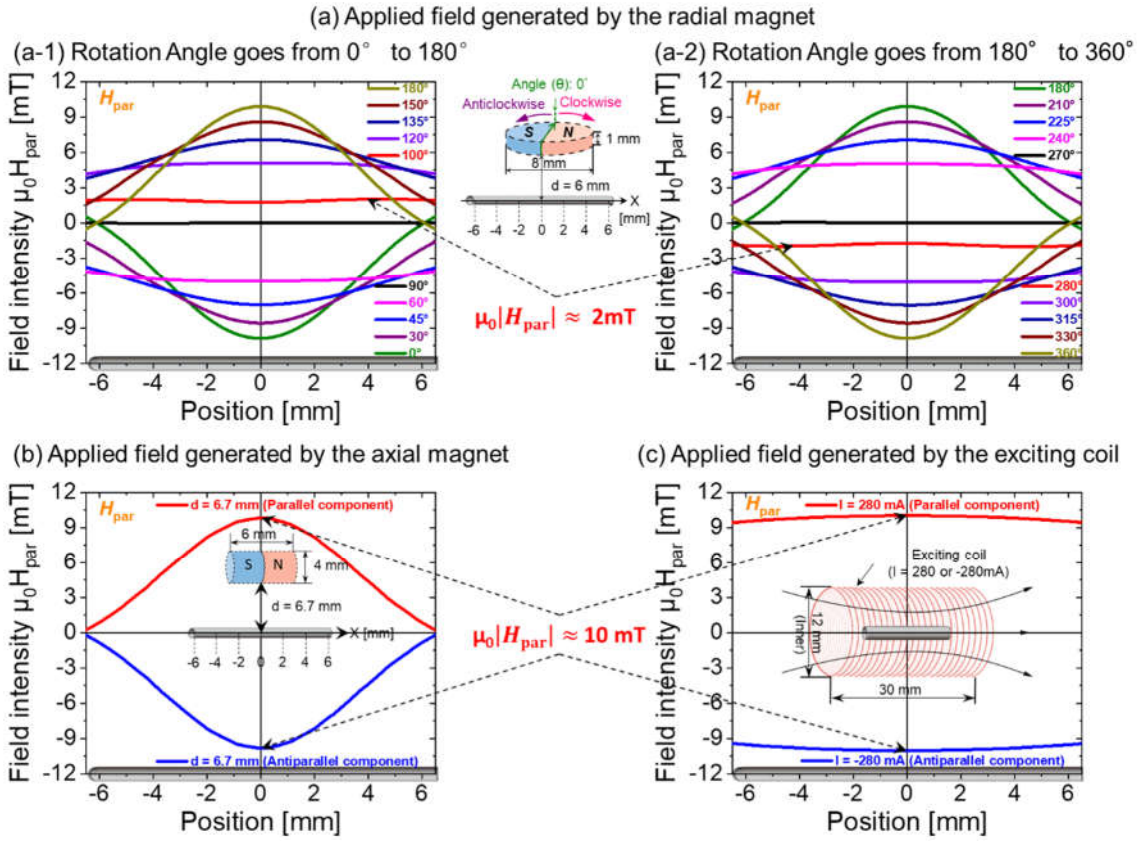

Figure 5.5 Simulated applied magnetic field distribution: (a) generated by the rotating radial magnet; (b) generated by the axial magnet; and (c) generated by an exciting coil.

5.3 Excited by the Rotating Radial Magnet

5.3.1 Amplitude and Area of the Generated Pulses

Figure 5.6(a) displays the positive and negative output voltages from the pickup coils when the Wiegand wire with or without the beads is excited by the radial magnet rotating in the two directions. The intensity of the applied magnetic field at the center of the magnetic wire is either $\mu_0 H = 6$ mT (green) or $\mu_0 H = 10$ mT (purple). Figure 5.6(b) shows the experimentally measured area of the pulse under the same conditions.

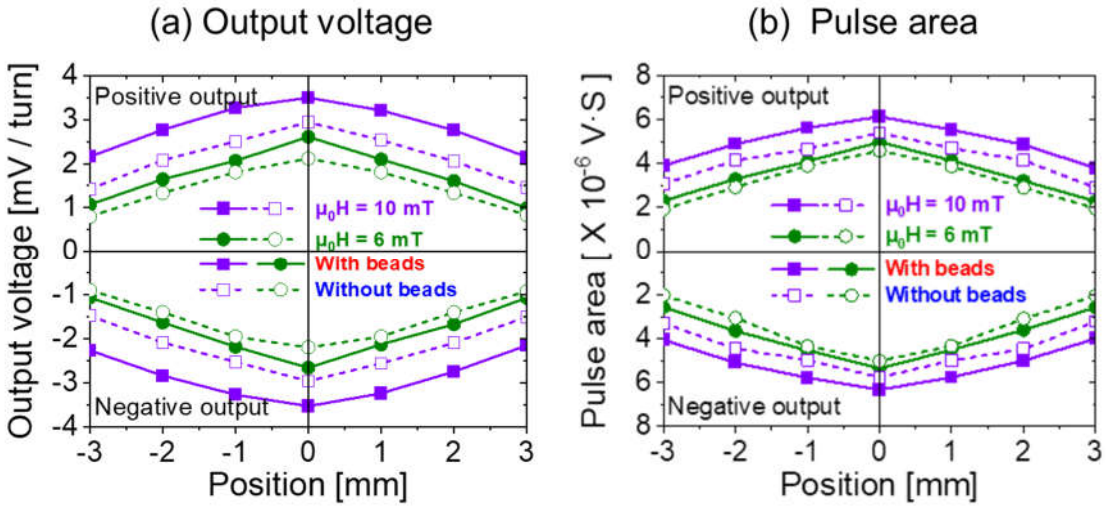

Figure 5.6 Experimental results of the pulses from the pickup coils in both Wiegand wire models, when excited by the rotating radial magnet: (a) output voltage; and (b) pulse area.

From Figure 5.6, both the amplitude and area of the voltage pulse reach a maximum when the pickup coil is located at 0 mm on the Wiegand wire, irrespective of the presence of the ferrite beads and the intensity of the applied magnetic field. As mentioned above, both the amplitude and area of the pulse are proportional to the volume of the reversed soft layer in the Wiegand wire, and this volume depends on the intensity of the applied driving field [33]. Thus, the magnetic field applied to the Wiegand wire changes according to the same trend. Also, the maximum amplitude and area of the pulse occur at the location with the highest magnetic field intensity. The degree of magnetization reversal of the soft layer in the Wiegand wire increases with the volume of the reversed soft layer, which is in turn proportional to the intensity of the applied magnetic field; this can be obtained by

analyzing the amplitude and area of the pulse.

Figure 5.6 also shows a larger amplitude and area of the pulse when ferrite beads are added to the ends of the Wiegand wire, or when the applied magnetic field is stronger. Therefore, either of these changes will enhance the degree of the magnetization reversal. It also supports the indication that the magnetic flux density through the center of the Wiegand wire is higher with the ferrite beads. These trends are consistent with the previous discussion, i.e., that the degree of magnetization reversal is proportional to the intensity of the magnetic field applied to the Wiegand wire.

5.3.2 Time Differential of the Generated Pulses

Figure 5.7 shows the appearance time of the pulse output at different positions along the Wiegand wire. When the radial magnet is rotating, the pulse is first detected at 0 mm, and then successively at locations further from there, regardless of the presence of the beads and the intensity of the applied magnetic field. This means that the magnetization reversal initially occurs at the sites with the most intense applied magnetic field. That is to say, both the initialization and maximum degree of magnetization reversal in the soft layer are detected at the position with the strongest magnetic field.

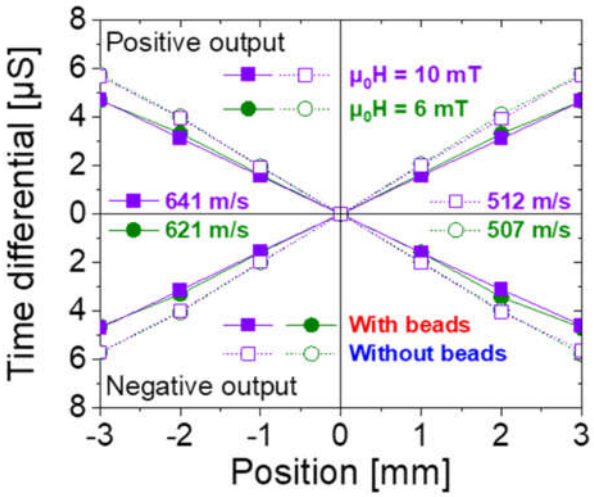

Figure 5.7 Time differential of the pulses excited by the rotating radial magnet.

The nucleation of reverse magnetic domain should occur under the highest reverse magnetic field; then, it should propagate to areas with a weaker magnetic field, and stop where the applied field intensity is lower than the coercive force of the magnetic material [41]. Therefore, the reverse magnetic domain is the origin of magnetization reversal in the soft layer of the magnetic wire, and propagates along the direction of the magnetization reversal. In other words, the reverse magnetization propagates in the direction of decreasing magnetic field intensity, and stops in the soft layer at approximately μ_0H = 2 mT.

To visually represent the initial position and propagation direction of the magnetization reversal and compare the degree of magnetization at the same position in both models of the magnetic wire, the waveforms of pulses were measured experimentally at -3, -2, -1, 0, 1, 2, and 3 mm, as displayed in Figure 5.8. All of the pulses show a symmetrical distribution between the two halves of the wire; thus, only the portion from the center to

the right is considered here.

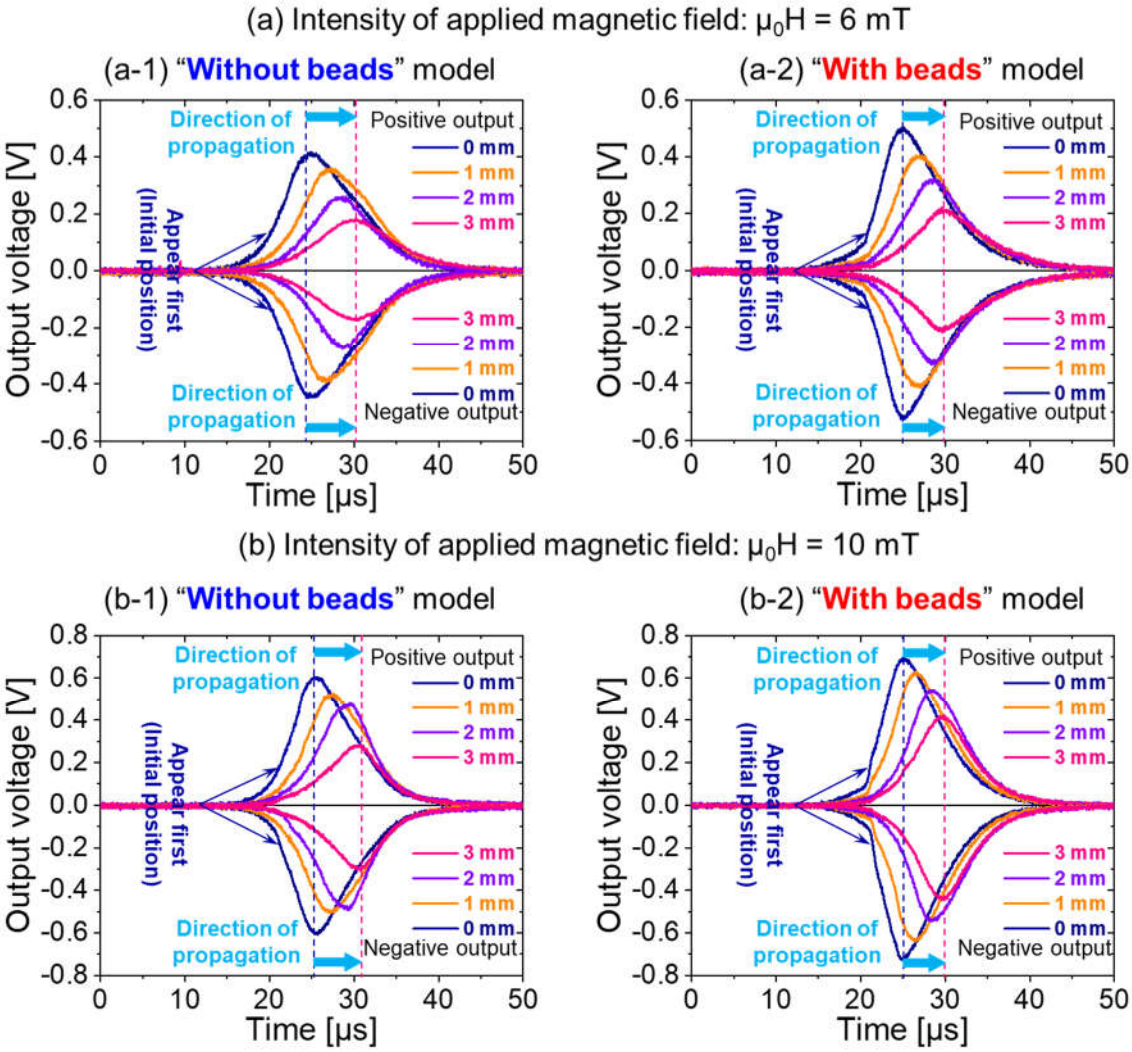

Figure 5.8 Waveforms of the pulses excited by the rotating radial magnet: (a) $\mu_0 H$ = 6 mT; and (b) $\mu_0 H$ = 10 mT.

The sequential appearance of the pulses in Figure 5.8 also demonstrates that the magnetization reversal of the soft layer is gradual and propagates from the initial position towards both ends of the magnetic wire, in accordance with the movement of the reverse magnetic domain nucleation. The propagation velocities at $\mu_0 H$ = 10 and 6 mT are calculated from the slope of the time differential in Figure 5.7 as 641 and 621 m/s for the "With beads" model, respectively. For the "Without beads" model, the corresponding values are 512 and 507 m/s, respectively.

For the "With beads" model, when multiple measurements are made at the same position,

the obtained maximum and minimum velocities differ by 56 m/s, whereas the difference for the “Without beads” model is 44 m/s. With this in mind, the propagation velocity of the magnetization reversal can be considered as independent of the applied magnetic field intensity. However, the propagation velocity is much faster when using the ferrite beads. This is attributed to the reduction of the exchange energy between the magnetic domains in the sample.

As the ferrite beads are set at both ends of the Wiegand wire, under the same external conditions (the intensity of the applied magnetic field is the same), the degree of magnetization reversal of the soft layer is significantly enhanced. This means that the magnetostatic coupling between the soft layer and hard core in the sample is significantly enhanced, i.e., the magnetostatic energy in the sample is significantly increased. In the process by which the degree of magnetization reversal of the soft layer is significantly enhanced, no evident changes are observed in the length and shape of the sample, that is, the magnetocrystalline anisotropy and magnetostriction energy in the sample do not change significantly. In this way, the exchange energy in the Wiegand wire should be significantly reduced, so as to satisfy the principle that the stable state of the magnetic domain is determined by the minimum value of the total free energy. Thus, with a smaller exchange energy between the magnetic domains in the sample, there is less resistance to the propagation of the reverse magnetic domain wall in the wire, and the propagation velocity of the domain wall increases when using the ferrite beads.

5.3.3 Magnetization Characteristics in the Applied Magnetic Field

Overall, the magnetization characteristics of the Wiegand wire under an external field generated by a single rotating radial magnet are summarized in Figure 5.9.

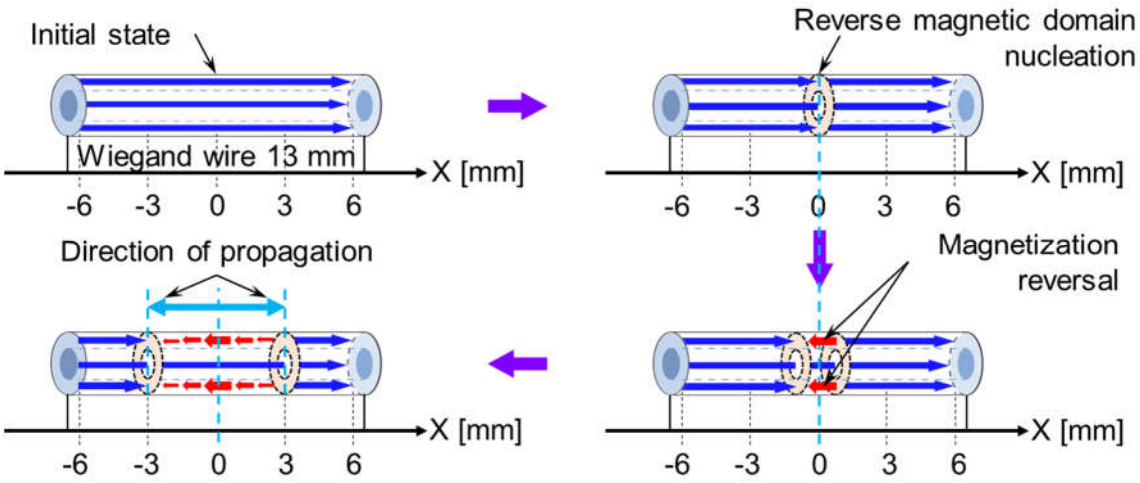

Figure 5.9 Magnetization characteristics of the magnetic wire excited by the rotating radial magnet.

5.4 Excited by the Pair of Rotating Axial Magnets

5.4.1 Amplitude and Area of the Generated Pulses

Figure 5.10 shows the experimental output voltages (both positive and negative) and pulse areas from the pickup coils when the two Wiegand wire models are excited by the pair of rotating axial magnets. The applied magnetic fields in the center of the magnetic wire were $\mu_0 H$ = 6 and 10 mT, respectively.

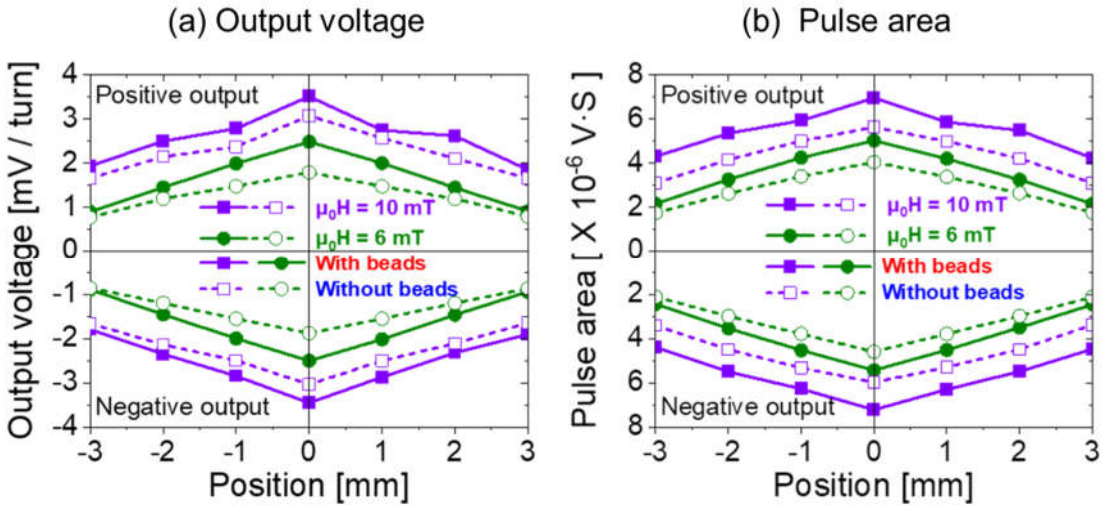

Figure 5.10 Experimental results of the pulses from the pickup coils in both Wiegand wire models, when excited by the pair of rotating axial magnets: (a) output voltage; and (b) pulse area.

From Figure 5.10, it can be seen that the amplitude and area of the pulse are almost the same between the pair of rotating axial magnets and the rotating radial magnet, meaning that there is identical effect on the degree of magnetization reversal in the soft layer of the Wiegand wire. Furthermore, the amplitude and area are larger near the center of the wire and smaller at both ends, suggesting a similar trend in the degree of magnetization reversal in the soft layer. The reason is that the degree of magnetization reversal depends on the intensity of the field applied to the wire. Under this type of applied magnetic field, the degree of magnetization reversal in the soft layer is also enhanced when the ferrite beads are set at both ends of the magnetic wire, or when the applied magnetic field intensity at the center of the magnetic wire is increased.

5.4.2 Time Differential of the Generated Pulses

Figure 5.11 displays the time differential of the pulses in both models as excited by the pair of rotating axial magnets. Regardless of the presence of the ferrite beads, a reverse magnetic domain nucleation initially occurs at the center of the Wiegand wire (0 mm) and moves towards both ends, and the time differential increases with the distance. Therefore, the initial magnetization reversal of the soft layer also occurs at 0 mm, where the magnetic field intensity is the strongest. Then, reverse magnetization propagates in the wire in the same direction as the movement of the domain wall, i.e., towards a lower applied magnetic field intensity. From the slope of the time differential in Figure 5.11, the propagation velocities in the "With beads" model are 644 and 633 m/s at $\mu_0 H$ = 10 and 6 mT, respectively. For the "Without beads" mode, the corresponding values are 496 and 500 m/s, respectively. Given the measurement errors, this velocity is also considered as independent of the applied field intensity in this setup. Similar to the rotating radial magnet, it is also much faster in the "With beads" model than in the "Without beads" model.

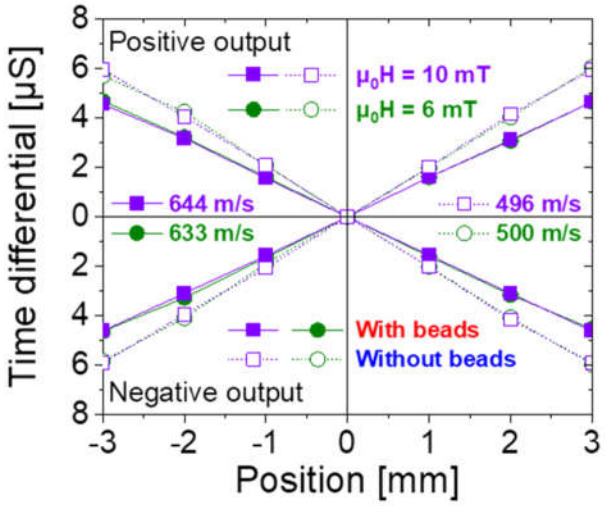

Figure 5.11 Time differential of the pulses excited by the pair of rotating axial magnets.

To clearly identify the initial position and propagation direction of the magnetization reversal, the waveforms of the pulses are shown in Figure 5.12. For the same reason as the rotating radial magnet, only the portion from the center to the right is considered here.

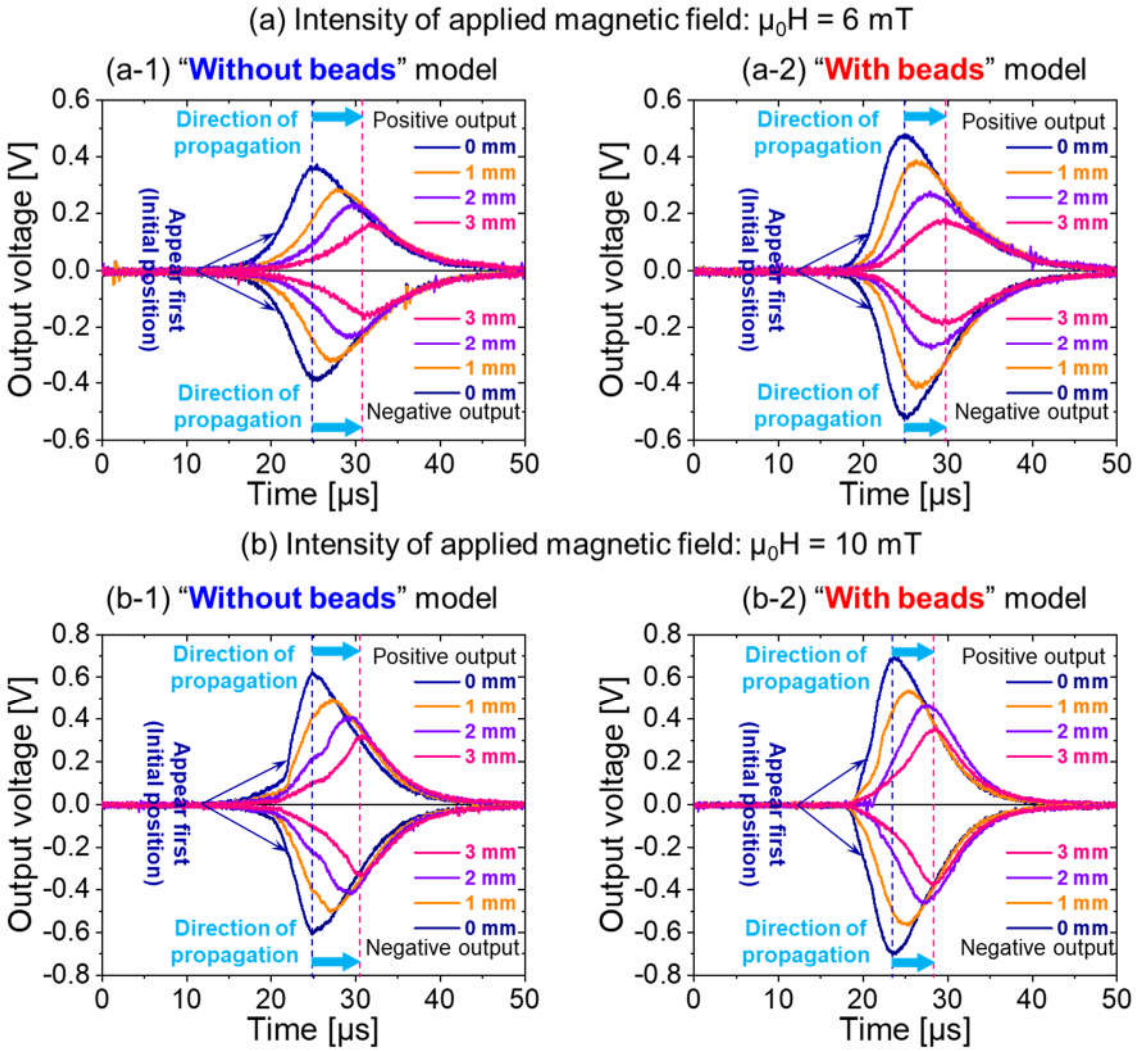

Figure 5.12 Waveforms of the pulses excited by the pair of rotating axial magnets: (a) $\mu_0 H$ = 6 mT; and (b) $\mu_0 H$ = 10 mT.

From Figure 5.12, the pulse induced at the end of the wire lagged behind that induced at the center, the time differential is position-dependent, and the time differential between adjacent positions is shorter in the "With beads" model than in the "Without beads" model. These results are consistent with previous discussion for the radial magnet.

5.4.3 Magnetization Characteristics in the Applied Magnetic Field

Overall, in the applied magnetic field generated by the pair of rotating axial magnets, nucleation is initiated at the center of the wire (the initial position of the magnetization reversal). The domain wall moves from the center to both ends (the direction of magnetization reversal propagation), and the propagation velocity is faster in the presence of ferrite beads. Figure 5.13 is a sketch of the magnetization characteristics under this applied field.

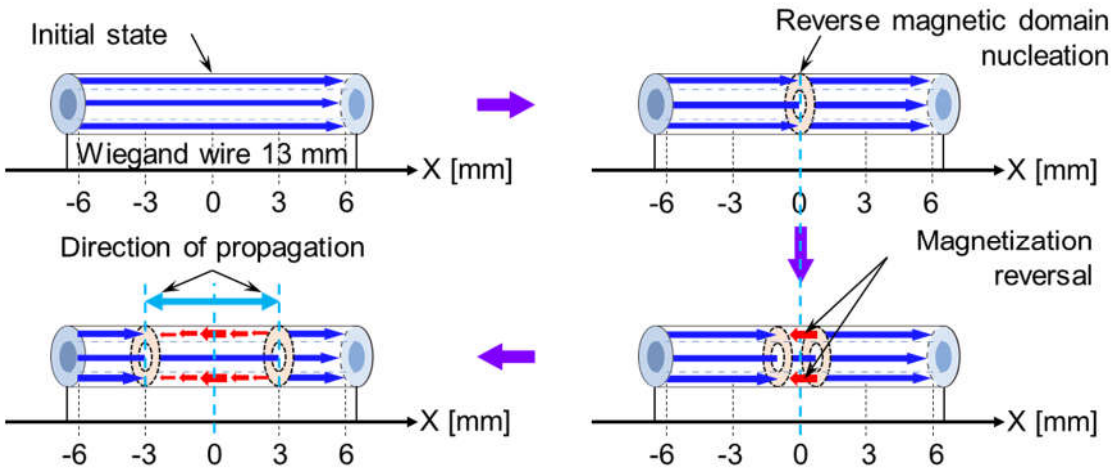

Figure 5.13 Magnetization characteristics of the magnetic wire excited by the pair of rotating axial magnets.

5.5 Excited by the Exciting Coil

5.5.1 Amplitude and Area of the Generated Pulses

When using an external coil for excitation, the amplitude of the pulse is approximately constant near the center of the wire (from -3 to 3 mm, Figure 5.14(a)), regardless of the use of ferrite beads and the applied field intensity. Figure 5.14(b) shows that the area of the pulse is also almost unchanged in this range, which is not surprising, as the exciting coil generates a mostly uniform magnetic field along its axis. In addition, the degree of magnetization reversal in the soft layer is constant across the wire.

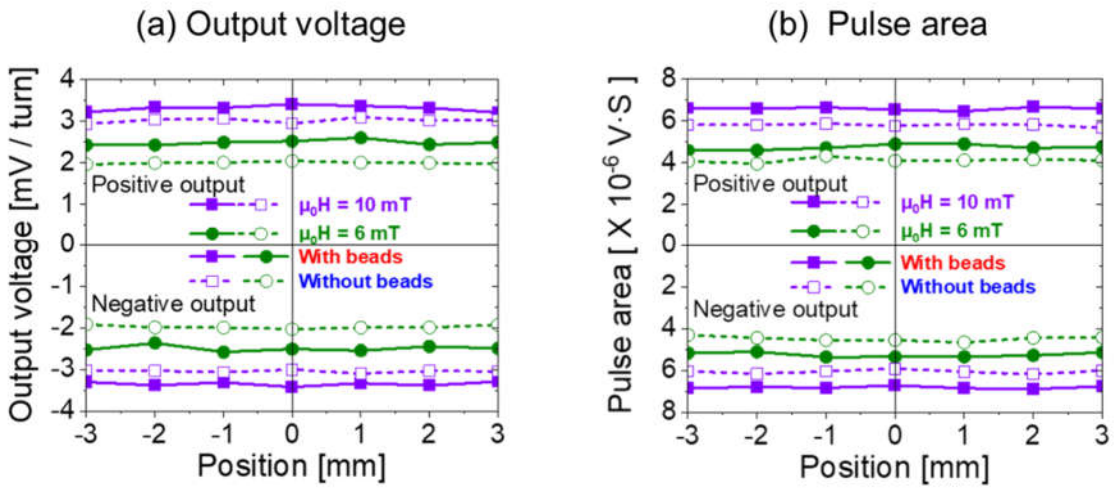

Figure 5.14 Experimental output voltage and pulse area from the pickup coils in both models under the exciting coil: (a) output voltage; and (b) pulse area.

Figure 5.14 shows that the degree of magnetization reversal is also affected by the presence of the ferrite beads at the ends of the wire and the applied magnetic field intensity. Meanwhile, under a uniform external magnetic field, the effective field intensities in the wire at certain locations are almost the same.

5.5.2 Time Differential of the Generated Pulses

The time differential and waveforms of the pulse output from the pickup coils under the exciting coil are shown in Figure 5.15 and Figure 5.16, respectively. Like the other two types of applied magnetic fields, only the waveforms from the center to the right of the wire are considered, and the experimental conditions are the same.

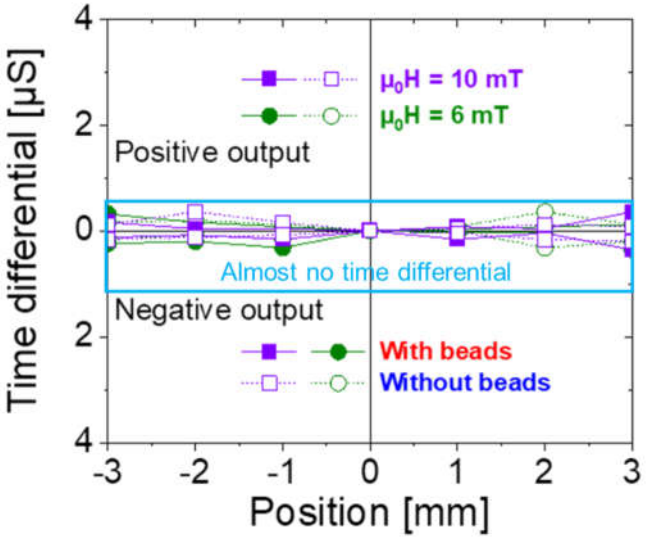

Figure 5.15 Time differential of the voltage pulses generated under the exciting coil.

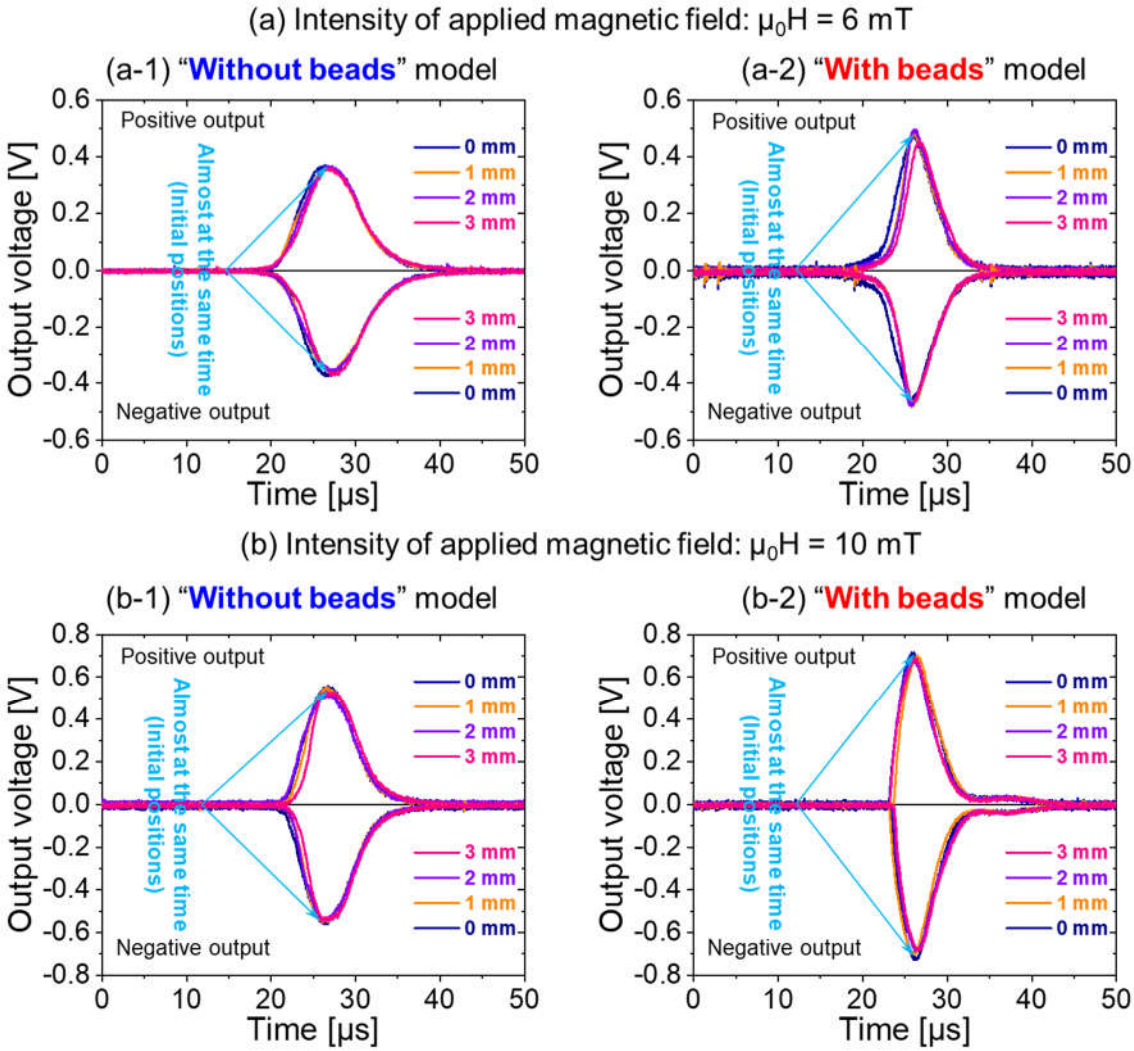

Figure 5.16 Waveforms of the pulses generated under the exciting coil: (a) $\mu_0 H$ = 6 mT; and (b) $\mu_0 H$ = 10 mT.

As demonstrated in Figure 5.15 and Figure 5.16, either with or without the ferrite beads, pulses are generated almost simultaneously in the range of -3 to 3 mm, i.e., where the reverse magnetic domain nucleation initially occurs under this setup. This is attributed to the applied magnetic field, as it is a uniform magnetic field, and the applied magnetic field intensity is almost the same in the range of -3 to 3 mm, where the magnetic field intensity is the strongest. Thus, the reverse magnetic domain occurs almost simultaneously in this range.

5.5.3 Magnetization Characteristics in the Applied Magnetic Field

Figure 5.17 summarizes the magnetization characteristics of the magnetic wire under the exciting coil.

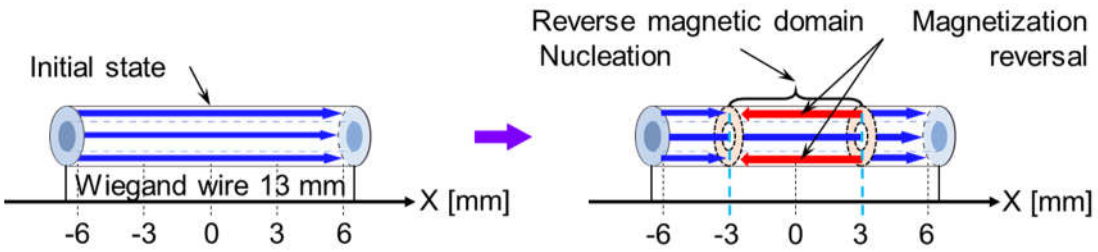

Figure 5.17 Magnetization characteristics of the magnetic wire under the exciting coil.

5.6 Summary

In this work, we examined the magnetization characteristics of a magnetic wire in a Wiegand sensor when the Wiegand wire was excited by three common types of alternating magnetic fields. Through systematic experiments, the relationship between the distribution of the applied magnetic field for excitation and resultant magnetization characteristics was clarified, as follows. (1) The initial magnetization reversal, i.e., the reverse magnetic domain nucleation, occurs at the position in the wire with the maximum applied magnetic field. (2) The intensity of the magnetic field applied to the wire determines the degree of the magnetization reversal. (3) The domain wall moves in the direction of decreasing magnetic field intensity, which is also the direction of the magnetization reversal propagation. (4) The propagation velocity of the magnetization reversal in the soft layer is independent of the applied magnetic field intensity and the rotation direction of the magnet(s).

Further research should be conducted for magnetic wires excited by other types of magnetic fields. The obtained magnetization characteristics could be used to help design a Wiegand sensor to maximize the amplitude and area of the pulse generated under these exciting magnetic fields. This will ensure that sufficient power is supplied by the Wiegand senor for battery-less electric devices and energy harvesting.

Chapter 6: Conclusion

With the rapid development of IoT technologies, certain monitoring nodes with wide ranges and irregular wiring can be replaced by wireless monitoring nodes, thereby greatly improving the depth and breadth of the application of the IoT. However, these wireless monitoring points require a large number of batteries that need to be replaced regularly, making maintenance expensive and time-consuming. Therefore, these wireless monitoring nodes need to be equipped with self-powered facilities to meet the growing demands for IoT devices.

In this research, the Wiegand sensor used for energy harvesting is proposed as a battery-less sensor or self-powered device, aiming to solve the power supply problem for monitoring, connection, and interactive devices in the IoT. The advantages of using the Wiegand sensor for energy harvesting are that the Wiegand sensor does not require an external power supply, the electrical energy is generated by the movement or vibration of the magnet at a very slow speed (almost zero, which may not be possible with other vibration-type energy harvesters), and a constant pulse voltage is induced (which does not depend on the time rate of change of the external magnetic field).

As the magnetic structure of the Wiegand wire cannot be elucidated using the traditional hysteresis curve, the FORC is used to analyze the magnetic characteristics of the Wiegand wire. The magnetic properties of the Wiegand wire are successfully clarified through a detailed analysis of the prominent features in its FORC diagram. It is found that the magnetization process of the soft layer is an irreversible process. The switching field and the intensity range of the applied magnetic field producing the Wiegand effect with a large Barkhausen jump correspond well with both the minor hysteresis curves and the FORC diagram. An irreversible magnetization process of the soft layer not accompanied by a large Barkhausen jump is also observed in the FORC diagram. The magnetization of the hard core is almost reversible. The magnetization of the intermediate region between the soft layer and hard core, which can be also interpreted as the soft layer interacting with the hard core, is observed in the FORC diagram. Therefore, a two-layer magnetic structure without marked boundaries is clarified.

In this study, the factors affecting the Wiegand pulse energy were determined by setting ferrite beads at both ends of the Wiegand wire, changing the position of the pickup coil around the Wiegand line, and adjusting the direction of the Wiegand sensor in the magnetic field. The relationships between these factors and the energy were successfully stated. When using the Wiegand sensor in practical applications, ferrite beads should be

set at both ends of the Wiegand wire to increase the magnetic flux density. The pickup coil on the Wiegand wire should be distributed evenly on both sides, with the center as the origin. In addition, when the Wiegand sensor is used as a power supply, it should be ensured that the magnetic induction line and Wiegand sensor are parallel or antiparallel, so as to obtain the maximum energy. The essential relationship between these factors and the energy of the Wiegand pulse has an effect on the volume of the reversed soft layer against the hard core.

The volume of the reversed soft layer in the Wiegand wire is proportional to the degree of magnetization of the soft layer in the Wiegand wire. The degree of magnetization of the soft layer under different excitation magnetic fields is determined by its magnetization characteristics. Therefore, the Wiegand wire models with and without the beads were both subjected to the three types of external magnetic fields to examine the magnetization characteristics. The three typical magnetic fields were produced by a rotating magnet with radial magnetization, a pair of rotating bar magnets with axial magnetization, and a solenoid coil with AC current. Through systematic experiments, the relationships between the distribution of the applied magnetic field for excitation and the resultant magnetization characteristics were clarified. It was found that the intensity of the magnetic field applied to the wire determines the degree of magnetization reversal. Both the initialization and maximum degree of magnetization reversal in the soft layer are detected at the position with the strongest magnetic field. The direction of magnetization reversal propagation is along the direction in which the intensity of the externally applied magnetic field decreases. The velocity of the domain wall movement is faster when ferrite beads are added to both ends of the Wiegand wire.

These magnetic characteristics of the Wiegand wire are expected to be applied when using the Wiegand sensors to design battery-less sensors or self-powered devices for the IoT. Meanwhile, this research provides a major development for the Wiegand sensors used as power sources for battery-less sensors or self-powered devices.

References

1. B. Jan, H. Farman, M. Khan, M. Talha, I.U. Din, “Designing a smart transportation system: An Internet of things and big data approach”, IEEE Wireless Communications, Vol. 26, pp. 73-79, 2019.

2. S. Balakrishna, M. Thirumaran, V. K. Solanki, “A framework for IoT sensor data acquisition and analysis”, EAI Endorsed Transactions on Internet of Things, Vol.4, pp. 1-13, 2018.

3. M. Bazzani, D. Conzon, A.Scalera, M. Spirito, C. Trainito, “Enabling the IoT paradigm in e-health solutions through the VIRTUS middleware”, In Proceedings of the IEEE 11th International Conference on Trust, Security and Privacy in Computing and Communications, Liverpool, UK, pp. 1954-1959, 25-27 June 2012.

4. DARPA, “Research Advances for Near-Zero-Power Sensors”, Available online: www.eetimes.com/darpa-research-advances-for-near-zero-power-sensors/#, accessed January 3, 2022.

5. S. Dhananjay, T. Gaurav, J. Antonio, “A survey of Internet-of-Things: Future vision, architecture, challenges and services”, In Proceedings of the IEEE World Forum on Internet of Things, Seoul, Korea (South), pp. 287-292, 6-8 March 2014.

6. R. J. M. Vullers, R. V. Schaijk, H. J. Visser, J. Penders, C. V. Hoof, “Energy harvesting for autonomous wireless sensor networks”, IEEE Solid-State Circuits Magazine, Vol. 2, pp. 29-38, 2010.

7. Tony Armstrong, “Green Buildings Get a Boost: Wireless sensor nodes as a key application for energy harvesting”, Analog Devices, Available online: https://www.analog.com/media/en/technical-documentation/tech-articles/green-buildings-get-a-boost.pdf, accessed March 6, 2021.

8. H. Jayakumar, A. Raha, Y. Kim, S. Sutar, W. S. Lee, V. Raghunathan, “Energy-efficient system design for IoT devices”, 21st Asia and South Pacific Design Automation Conference, Macao, China, pp. 298-301, 25-28 January 2016.

9. S. C. Lai, K. Yao, C. Y. Tan, “A Battery-Less Sensor Concept Outputting Perceivable Signal Demonstrated With an Accelerometer”, IEEE Sensors Journal, Vol. 16, pp. 7841-7842, 2016.

10. T. S. Muratkar, A. Bhurane, A. Kothari, “Battery-less Internet of Things -A Survey”, Computer Networks, Vol. 180, 107385, 2020.

11. R. J. M. Vullers, R. V. Schaijk, I. Doms, C. V. Hoof, R. Mertens, “Micropower energy harvesting”, Solid-State Electronics, Vol. 52, pp. 684-693, 2009.

12. M. Nielsen-Lönn, P. Angelov, J.J. Wikner, A. Alvandpour, “Self-powered micro-watt level piezoelectric energy harvesting system with wide input voltage range”, Analog Integrated Circuits and Signal Processing, Vol. 98, pp. 441-451, 2019.

13. S. P. Beeby, M. J. Tudor, N. M. White, “Energy harvesting vibration sources for microsystems applications”, Measurement Science and Technology, Vol. 17, pp. R175-R195, 2006.

14. J. A. Paradiso, T. Starner, “Energy scavenging for mobile and wireless electronics”, IEEE Pervasive Computing, Vol. 4, pp. 18-27, 2005.

15. N. Sharpes, D. Vuckovic, S. Priya, “Floor Tile Energy Harvester for Self-Powered Wireless Occupancy Sensing”, Energy Harvesting and Systems, Vol. 3, pp. 43-60, 2016.

16. A. A. A. Rahman, N. A. Rashid, A. S. A. Aziz, G. Witjaksono, “Design of autonomous micro-solar powered energy harvesting system for self-powered batteries-less wireless sensor mote”, 2012 Electronics Goes Green 2012+, Berlin, Germany, pp. 1-4, 9-12 September 2012.

17. G. KUERS, H.-J. GEVATTER, “Wiegand-Sensoren für Weg- und Geschwindigkeitsmessungen / Wiegand effect position and speed sensors”, Technisches Messen, Vol. 5, pp. 123-129, 1984.

18. Y. Takemura, N. Fujiyama, A. Takebuchi, T. Yamada, “Battery-less hall sensor operated by energy harvesting from a single Wiegand pulse”, IEEE Transactions on Magnetics, Vol. 53, 4002706, 2017.

19. K. Takahashi, A. Takebuchi, T. Yamada, Y. Takemura, “Power supply for medical implants by Wiegand pulse generated from a magnetic wire”, Journal of the Magnetics Society of Japan, Vol. 42, pp. 49-54, 2018.

20. R. Serizawa, T. Yamada, S. Masuda, S. Abe, S. Kohno, F. Kaneko, Y. Takemura, “Energy harvesting derived from magnetization reversal in FeCoV wire”, In Proceedings of the IEEE Sensors, Taipei, Taiwan, pp.28-31, October 2012.

21. C.-C. Chang, J.-Y Chang, “Novel Wiegand effect-based energy harvesting device for linear positioning measurement system”, In Proceedings of the Asia-Pacific Magnetic Recording Conference (APMRC), Shanghai, China, 15-17 November 2018.

22. J. M. D. Coey, “Magnetism and Magnetic Materials”, Cambridge University Press, 2010.

23. N. Spaldin, “Magnetic Materials: Fundamentals and Applications (2nd ed.)”, Cambridge University Press, 2010.

24. Kannan M. Krishnan, “Fundamentals and Applications of Magnetic Materials”, Oxford University Press, 2016.

25. J.R. Wiegand, M. Velinsky, “Bistable Magnetic Device”, U.S. Patent 3,820,090, 25 June 1974.

26. S. Abe, A. Matsushita, “Induced pulse voltage in twisted Vicalloy wire with compound magnetic effect”, IEEE Transactions on Magnetics, Vol. 31, pp. 3152-3154, 1995.

27. S. Abe, A. Matsushita, M. Naoe, “Dependence of large Barkhausen jump on length of a vicalloy fine wire with torsion stress”, IEEE Transactions on Magnetics, Vol. 34, pp. 1318-1320, 1998.

28. S. Abe, A. Matsushita, K. Negishi, Y. Baba, M. Naoe, “Generation of large Barkhausen jump in bilayered thin film”, IEEE Transactions on Magnetics, Vol. 35, pp. 3634-3636, 1999.

29. S. Abe, A. Matsushita, M. Naoe, “Annealing and torsion stress effect on magnetic anisotropy and magnetostriction of Vicalloy fine wire”, IEEE Transactions on Magnetics, Vol. 33, pp. 3916-3918, 1997.

30. Y. Takemura, T. Aoki, H. Tanaka, T. Yamada, S. Abe, S. Kohno, H. Nakamura, “Control of demagnetizing field and magneto static coupling in FeCoV wires for zero-speed sensor”, IEEE Transactions on Magnetics, Vol. 42, pp. 3300-3302, 2006.

31. C. Radeloff, G. Rauscher, “Pulse generation with short composite wires”, IEEE Transactions on Magnetics, Vol. 21, pp. 1933-1935, 1985.

32. T. Kohara, T. Yamada, S. Abe, S. Kohno, F. Kaneko, Y. Takemura, “Effective excitation by single magnet in rotation sensor and domain wall displacement of FeCoV wire”, Journal of Applied Physics, Vol. 109, 07E531, 2011.

33. C. Yang; T. Sakai, T. Yamada, Z. Song, Y. Takemura, “Improvement of pulse voltage generated by Wiegand sensor through magnetic-flux guidance”, Sensors, Vol. 20, 1408, 2020.

34. A. Matsushita, Y. Takemura, “Power generating device using compound magnetic wire”, Journal of Applied Physics, Vol. 87, pp. 6307-6309, 2000.

35. J.R. Wiegand, “Switchable Magnetic Device”, U.S. Patent 4,247,601, 27 January 1981.

36. S. Abe, A. Matsushita, M. Naoe, “Annealing and torsion stress effect on magnetic anisotropy and magnetostriction of Vicalloy fine wire”, IEEE Transactions on Magnetics, Vol. 33, pp. 3916-3918, 1997.

37. K. Mohri, F. Kinoshita, T. Yamamoto, J. Yamasaki, “Large Barkhausen Effect and Matteucci Effect of Amorphous Magnetostrictive Wires”, IEEE Translation Journal on Magnetics in Japan, Vol. 1, pp. 231-232, 1985.

38. H. Kawamura, K. Mohri, J. Yamasaki, L. Ogasawara, “Large Barkhausen Effect and Matteucci Effect in Cold-Drawn and Torsion Annealed Amorphous Magnetostrictive Wires”, IEEE Translation Journal on Magnetics in Japan, Vol. 3, pp. 609-610, 1988.

39. J. Kravcak, L. Novak, “The analysis of large Barkhausen effect in the FeSiB amorphous wire”, Czechoslovak Journal of Physics, Vol. 52, pp. 175-178, 2002.

40. Y. Takemura, T. Yamada, “Output Properties of Zero-Speed Sensors Using FeCoV Wire and NiFe/CoFe Multilayer Thin Film”, IEEE Sensors Journal, Vol. 6, pp. 1186-1190, 2006.

41. H. Tanaka, T. Yamada, Y. Takemura, S. Abe, S. Kohno, H. Nakamura, “Constant velocity of domain wall propagation independent of applied field strength in vicalloy wire”, IEEE Transactions on Magnetics, Vol. 43, pp. 2397-2399, 2007.

42. S. Saggini, F. Ongaro, L. Corradini, A. Affanni, “Low-power energy harvesting solutions for Wiegand transducers”, IEEE Journal of Emerging and Selected Topics in Power Electronics, Vol. 3, pp. 766-779, 2015.

43. A. Takebuchi, T. Yamada, Y. Takemura, “Reduction of vibration amplitude in vibration-type electricity generator using magnetic wire”, Journal of the Magnetics Society of Japan, Vol. 41, pp. 34-40, 2017.

44. Takahashi, K.; Yamada, T.; Takemura, Y. Circuit parameters of a receiver coil using a Wiegand sensor for wireless power transmission. Sensors 2019, 19, 2710.

45. X. Sun, T. Yamada, Y. Takemura, “Output characteristics and circuit modeling of Wiegand sensor”, Sensors, Vol. 19, 2991, 2019.

46. K.J. Sixtus, L. Tonks, “Propagation of large Barkhausen discontinuities. II”, Physical Review, Vol. 42, pp. 419-435, 1932.

47. C. Zou, D. Guo, F. Zhang, J. Meng, H. Miao, W. Jiang, “Magnetization, the susceptibilities and the hysteresis loops of a borophene structure”, Physica E: Low-Dimensional Systems and Nanostructures, Vol. 104, pp.138-145, 2018.

48. M. Teerawat, K. Kanokwan, Y. Rattikorn, L. Yongyut, “Modeling and characterization of hysteresis loops with Preisach hysteron weight modification”, Integrated Ferroelectrics, Vol. 175, pp.33-43, 2016.

49. A.P. Roberts, C.R. Pike, K.L Verosub, “First-Order Reversal Curve Diagrams: A New Tool for Characterizing the Magnetic Properties of Natural Samples”, Journal of Geophysical Research: Solid Earth, Vol. 105, pp. 28461-28475, 2000.

50. V. Franco1, T, Gottschall, K.P. Skokov, O. Gutfleisch, “First-Order Reversal Curve (FORC) Analysis of Magnetocaloric Heusler-Type Alloys”, IEEE Magnetics Letters, Vol. 7, 6602904, 2016.

51. B. Dodrill, J. Lindemuth, C. Radu, H. Reichard, “White Paper: High-temperature FORC study of single- and multi-phase permanent magnets”, MRS Bulletin, Vol. 40, pp. 903–905, 2015.

52. B. Dodrill, P. Ohodnicki, M. McHenry, A. Leary, “High-Temperature First-Order-Reversal-Curve (FORC) Study of Magnetic Nanoparticle Based Nanocomposite Materials”, MRS Advances, Vol. 2, pp. 2669-2674, 2017.

53. Robert G. Harrison, “Physical Theory of Ferromagnetic First-Order Return Curves”, IEEE Transactions on Magnetics, Vol. 45, pp. 1922-1939, 2009.

54. D. Cimpoesu, L. Spinu, A. Stancu, “Temperature Dependence of FORC Diagrams in Nanostructured Materials”, IEEE Transactions on Magnetics, Vol. 42, pp. 3165-3167, 2006.

55. C.R. Pike, A.P. Roberts, M.J. Dekkers, K.L. Verosub, “An investigation of multi-domain hysteresis mechanisms using FORC diagrams”, Physics of the Earth and Planetary Interiors, Vol. 126, pp. 11-25, 2001.

56. N. Gaur, S. N. Piramanayagam, S. L. Maurer, S. E. Steen, H. Yang, C. S. Bhatia, “First-Order Reversal Curve Investigations on the Effects of Ion Implantation in Magnetic Media”, IEEE Transactions on Magnetics, Vol. 48, pp. 2753-2756, 2012.

57. C.R. Pike, A.P. Roberts, K.L. Verosub, “Characterizing interactions in fine magnetic particle systems using first order reversal curves”, Journal of Applied Physics, Vol. 85, pp. 6660-6667, 1999.

58. C. R. Pike, A. P. Roberts, K. L. Verosub, “First-order reversal curve diagrams and thermal relaxation effects in magnetic particles”, Geophysical Journal International, Vol. 145, pp. 721-730, 2001.

59. Q. Wu, J.T. Li, H.L. Ge, Y.H. Tu, M.X. Pan, P.Y. Zhang, “Coercivity mechanism and FORC analysis of MnBi-Based permanent alloy”, Journal of Magnetism and Magnetic Materials, Vol. 503, 166600, 2020.

60. F. Béron, L. Clime, M. Ciureanu, D. Ménard, R. W. Cochrane, A. Yelon, “Magnetostatic interactions and coercivities of ferromagnetic soft nanowires in uniform length arrays”, Journal of Nanoscience and Nanotechnology, Vol. 8, pp. 2944-2954, 2008.

61. G. Acton; Q.-Z. Yin; K. L. Verosub, L. Jovane, A, Roth, B. Jacobsen; D. S. Ebel, “Micromagnetic coercivity distributions and interactions in condrules with implications for paleointensities of the early solar system”, Journal of Geophysical Research, Vol. 112, B03S90, 2007.

62. R.J. Harrison, J.M. Feinberg, “FORCinel: An Improved Algorithm for Calculating First-Order-Reversal Curve Distributions Using Locally Weighted Regression Smoothing”, Geochemistry Geophysics Geosystems, Vol. 9, Q05016, 2008.

63. R. Egli, “VARIFORC: An optimized protocol for calculating non-regular first-order reversal curve (FORC) diagrams”, Global and Planetary Change, Vol. 110, pp. 302-320, 2013.

64. Y. Takemura, A. Matsushita, “Frequency dependence of output voltage generated from bundled compound magnetic wires”, IEEE Transactions on Magnetics, Vol. 37, pp. 2862-2864, 2001.

65. Y. Sang, X. Huang, H. Liu, P. Jin, “A Vibration-Based Hybrid Energy Harvester for Wireless Sensor Systems”, IEEE Transactions on Magnetics, Vol. 48, pp. 4495-4498, 2012.

66. A.R. Muxworthy, A.P. Roberts, “First-Order Reversal Curve (FORC) Diagrams”, Encyclopedia of Geomagnetism and Paleomagnetism, pp. 266-272, 2007.

67. A. Mesbahinia, M. Almasi-Kashi, A. Ghasemi, A. Ramazani, “FORC investigation of Co-Ni bulk ferrite consolidated by spark plasma sintering technique”, Journal of Magnetism and Magnetic Materials, Vol. 497, 165976, 2020.

68. D. Heslop, A.R. Muxworthy, “Aspects of calculating first-order-reversal-curve distributions”, Journal of Magnetism and Magnetic Materials, Vol. 288, pp. 155-167, 2005.

69. A.B. Dobroserdova, P.A. Sánchez, V.E. Shapochkin, D.A. Smagin, V.S. Zverev, S. Odenbach, S.S. Kantorovich, “Measuring FORCs diagrams in computer simulations as a mean to gain microscopic insight”, Journal of Magnetism and Magnetic Materials, Vol. 501, 166393, 2020.

70. C.R. Pike, C.A. Ross, R.T. Scalettar, G. Zimanyi, “First-order reversal curve diagram analysis of a perpendicular nickel nanopillar array”, Physical Review B, Vol. 71, 134407, 2005.

71. C. Carvallo, P. R. Andrew, L. Roman, L. Carlo, K. Catherine, P. Mireille, C. Pierre, “Increasing the efficiency of paleointensity analyses by selection of samples using first-order reversal curve diagrams”, Journal of Geophysical Research: Solid Earth, Vol. 111, B12103, 2006.

72. R. Lavín, J. C. Denardin, J. Escrig, D. Altbir, A. Cortés, H. Gómez, “Magnetic Characterization of Nanowire Arrays Using First Order Reversal Curves”, IEEE Transactions on Magnetics, Vol. 44, pp. 2808-2811, 2008.

73. A.-A. Sima, A.-K. Mohammad, A. Ramazani, “Magnetic characterization of FeCo nanowire arrays by first-order reversal curves”, Current Applied Physics, Vol. 13, pp. 664-669, 2013.

74. F. Béron, L.-P. Carignan, D. Ménard, A. Yelon, “Magnetic Behavior of Ni-Cu Multilayer Nanowire Arrays Studied by First-Order Reversal Curve Diagrams”, IEEE Transactions on Magnetics, Vol. 44, pp. 2745-2748, 2008.

75. C. Rong, Y. Zhang, M.J. Kramer, L.J. Ping, “Correlation between microstructure and first-order magnetization reversal in the SmCo5/α-Fe nanocomposite magnets”, Physics Letters A, Vol. 375, pp. 1329-1332, 2011.

76. O. Sahar, A.-K. Mohammad, A.-A. Sima, “Sn addition effect on magnetic reversibility of Co–Ni alloy nanoparticles based on the FORC results”, Materials Chemistry and Physics, Vol. 243, 122575, 2020.

77. S. Laurentiu, S. Alexandru, “Using Experimental FORC Distribution as Input for a Preisach-Type Model”, IEEE Transactions on Magnetics, Vol. 42, pp. 3159-3161, 2006.

78. R. Montserrat, G. Pedro, M.-G. Cristina, C. M.-G. José, “Quasi-Static AC FORC Measurements for Soft Magnetic Materials and Their Differential Interpretation”, IEEE Transactions on Magnetics, Vol. 53, 2003606, 2017.

79. A.R. Muxworthy, J.G. King, D. Heslop, “Assessing the ability of first-order reversal curve (FORC) diagrams to unravel complex magnetic signals”, Journal of Geophysical Research, Vol. 110, B01105, 2005.

80. B. Ilie, S. Alexandru “Reversible Magnetization Processes Evaluation Using High-Order Magnetization Curves”, IEEE Transactions on Magnetics, Vol. 49, 4960-4964, 2013.

81. C. R. Pike, “First-order reversal-curve diagrams and reversible magnetization”, Physical Review B, Vol. 68, 104424, 2003.

82. A.J. Newell, “FORCs, SORCs and Stoner-Wohlfarth Theory”, In Proceedings of the AGU Fall Meeting Abstracts, San Francisco, USA, GP31B-0748, 8-12 December 2003.

83. G. Muscas, M. Menniti, R. Brucas, P.E. Jönsson, “Mesoscale magnetic rings: complex magnetization reversal uncovered by FORC”, Journal of Magnetism and Magnetic Materials, Vol. 502, 166559, 2020.

84. S. N. Piramanayagam, M, Ranjbar, R, Sbiaa, C. T. Chong, “Magnetic and First-Order Reversal Curve Investigations of Antiferromagnetically Coupled Nanostructures of Co-Pd Multilayers”, IEEE Transactions on Magnetics, Vol. 48, pp. 3410-3413, 2012.

85. C. Carvallo, A.R. Muxworthy, D.J. Dunlop, “First-order reversal curve (FORC) diagrams of magnetic mixtures: Micromagnetic models and measurements”, Physics of the Earth and Planetary Interiors, Vol. 154, pp. 308-322, 2006.

86. C. Carvallo, A. R. Muxworthy, D, J. Dunlop, W. Williams, “Micromagnetic modeling of first-order reversal curve (FORC) diagrams for single-domain and pseudo-single-domain magnetite”, Earth and Planetary Science Letters, Vol. 213, pp. 375-390, 2003.

87. A. R. Muxworthy, D. J. Dunlop, “First-order reversal curve (FORC) diagrams for pseudo-single-domain magnetites at high temperature”, Earth and Planetary Science Letters, Vol. 203, pp. 369-382, 2002.

88. A.R. Muxworthy, D. Heslop, W. Williams, “Influence of magnetostatic interactions on first-order-reversal-curve (FORC) diagrams: A micromagnetic approach”, Geophysical Journal International, Vol. 158, pp. 888-897, 2004.

89. A. Muxworthy, W. Williams, D. Virdee, “Effect of magnetostatic interactions on the hysteresis parameters of single-domain and pseudo-single-domain grains”, Journal of Geophysical Research, Vol. 108, 2517, 2003.

90. A. Muxworthy, W. Williams, “Magnetostatic interaction fields in first-order-reversal-curve diagrams”, Journal of Applied Physics, Vol. 97, 063905, 2005.

91. Y. Fang, C. L. Zha, S. bonetti, J. Åkerman, “FORC studies of exchange biased NiFe in $L1_0$(111) FePt-based spin valve”, Journal of Physics: Conference Series, Vol. 200, 072002, 2000.

92. M. A. Kashi, A. Ramazani, A. S. Esmaeily, “Magnetostatic Interaction Investigation of CoFe Alloy Nanowires by First-Order Reversal-Curve Diagrams”, IEEE Transactions on Magnetics, Vol. 49, pp. 1167-1171, 2017.

93. S. Okamoto, T. Yomogita, K. Miyazawa, N. Kikuchi, O. Kitakami, N. Watanabe, N. Suita, “First-order Reversal Curve (FORC) Analysis and Its Application for Permanent Magnet Materials”, Materia Japan, Vol. 56, pp. 533-540, 2017.

94. E. Cristian, S. Alexandru, “FORC Analysis of Size Effects in Ising-Type Models of Disordered Magnets”, IEEE Transactions on Magnetics, Vol. 42, pp. 3156-3158, 2006.

95. T. Radu, S. Alexandru, “Statistical Characterization of the FORC Diagram”, IEEE Transactions on Magnetics, Vol. 42, pp. 3246-3248, 2006.

96. R. Malmhall, K. Mohri, F.B. Humphrey, T. Manabe, H. Kawamura, J. Yamasaki, I. Ogasawara, “Bistable magnetization reversal in 50 μm diameter annealed cold drawn amorphous wires”, IEEE Transactions on Magnetics, Vol. 23, pp. 3242-3244, 1987.

97. K. Sitapati, R. Krishnan, “Performance Comparisons of Radial and Axial Field, Permanent-Magnet, Brushless Machines”, IEEE Transactions on Industry Applications, Vol. 37, pp. 1219-1226, 2001.

98. M. Vázquez, C. Gómez-Polo, D.-X. Chen, A. Hernando, “Magnetic bistability of amorphous wires and sensor applications”, IEEE Transactions on Magnetics, Vol. 30, pp. 907-912, 1994.

Publications

[Papers]

[1] Chao Yang, Yuya Kita, Zenglu Song, and Yasushi Takemura
"Magnetic Reversal in Wiegand Wires Evaluated by First-Order Reversal Curves"
Materials (Q1, IF=3.623), Vol.14, No.14, 3868, pp. 1-9, 2021.
DOl: 10.3390/ma14143868 (**"Editor's Choice"**)

[2] Chao Yang, Takafumi Sakai, Tsutomu Yamada, Zenglu Song, and Yasushi Takemura
"Improvement of Pulse Voltage Generated by Wiegand Sensor through Magnetic-Flux Guidance"
Sensors (Q1, IF=3.275), Vol.20, No.5, 1408, pp. 1-10, 2020.
DOl: 10.3390/s20051408

[3] Chao Yang, Zenglu Song, and Yasushi Takemura
"Magnetization Characteristics of Magnetic Wire in Wiegand Sensor Excited by Various Magnetic Fields"
Preparing for submission